SINGLE QUANTUM DOT TRACKING FOR QUANTITATIVE MOLECULAR IMAGING

BY

MOHAMMAD USAMA ZAHID

DISSERTATION

Submitted in partial fulfillment of the requirements
for the degree of Doctor of Philosophy in Bioengineering
in the Graduate College of the
University of Illinois at Urbana-Champaign, 2018

Urbana, Illinois

Doctoral Committee:

Professor Andrew M. Smith, Chair
Professor Stephen A. Boppart
Professor Cecilia Leal
Professor Paul R. Selvin

ABSTRACT

The application of semiconductor nanocrystals known as quantum dots (QDs) to biology in the past few decades has advanced the field of single-molecule biology by allowing for long time-scale tracking of individual biomolecules. However, QD single-molecule imaging studies have almost been exclusively limited to the extracellular space, due to limitations in intracellular delivery techniques and a limited understanding of how nanoparticles behave in the intracellular space.

In the first half of this thesis, a new analysis methodology is developed to quantitatively assess the intracellular delivery of QDs. We present a method for using single-molecule imaging and subsequent single-particle tracking (SPT) of QDs delivered to the cytosol of living cells to assess delivery efficiency and uptake mechanisms. In this method, single quantum dot mobility information is used in conjunction with single-molecule brightness measurements to develop novel single-cell metrics of delivery efficiency. These metrics are used to investigate the impact of different nanoparticle surface properties on intracellular delivery and fate. We investigate the delivery of a series of QDs designed with diverse surface properties. This comparison revealed new insights into particle uptake and endosomal escape, as well as the discovery that zwitterionic surfaces are uniquely suited for intracellular mobility. Additionally, this new analysis methodology was validated by established experimental approaches and analysis of simulated single-particle trajectories.

The second half of this thesis applies the aforementioned tools towards two applications. The first application is to quantitatively evaluate QD labeling of intracellular proteins in live cells. This was achieved by delivering QDs conjugated to biorthogonal functional groups to label a target protein and developing a new colocalization-based metric to quantify the degree of protein target labeling. We present evidence of protein target labeling by using this single-trajectory level colocalization metric in combination with nanoparticle mobility measurements. The second application is toward accurate measurement of hydrodynamic size of colloids with dimensions smaller than 100 nanometers (nm). We develop a new method using widefield fluorescence microscopy and SPT to measure nanoparticle size and demonstrate accurate single-molecule size measurements of a homogeneous nanoparticle population with hydrodynamic diameter of approximately 20 nm.

ACKNOWLEDGEMENTS

First and foremost, I thank God Almighty for giving me the strength and ability to come to this point in my education and career, but as it is said “You are not thankful to God if you are not thankful to the people.” So, I’d like to take this brief space to offer a few words of gratitude to those without whom all of this could not have been possible.

First, my deepest gratitude goes to my advisor Dr. Andrew M. Smith. I am deeply indebted to him for all his help, patience, and guidance along my scientific path. Not only did he push me to excel in ways that I could not have imagined when starting at Illinois, but he also was immensely supportive in my professional development by constantly finding unique opportunities for me to develop as a researcher and as an aspiring educator.

Second, I’d like to thank my thesis committee members Dr. Stephen Boppart, Dr. Cecilia Leal, and Dr. Paul Selvin for serving on the committee and for your support and advice. I’d also like to thank Dr. Kris Kilian, who served on my prelim exam committee.

Next, I want to extend my thanks to all my collaborators at the University of Illinois, who contributed in key ways to the work presented in this dissertation. This includes all the past and present members of the Smith Lab (since I’ve been with the lab from the beginning). I’d mention each individual member of the lab by name, but there is not enough space here. However, I’d like to note that in addition to all their scientific contributions, every single lab member, past and present, has enriched my life in some way or another, and there is not a single member of this lab with whom I have not had supportive and fruitful conversations. I’ve been honored and blessed to work with this talented group of individuals. I’d specifically like to mention and thank Dr. Sung Jun Lim and Dr. Liang Ma, both of whom were with the Smith Lab from nearly the beginning. I learned how to dedicate myself to my work and how to be a researcher from Sung Jun’s work ethic and dedication. Liang trained me in various techniques in the lab, pushed me to work hard, and he is one of my closest friends from the lab.

I would be remiss if I did not mention all my collaborators from all across the University of Illinois campus. This list includes but is not limited to Dr. Daniel McDougle, Dr. Kai Wen Teng, Dr. Minjee Kang, Yeoan Youn, Dr. Doug Zhang, and Dr. Junmin Lee.

Finally, I need to thank my pillars of support: my family members. Ammee: my mom has been my greatest supporter, counselor, advisor, patient listener throughout the entire Ph.D. process. Ammee-jee, my favorite line of support from you in these last few months has been: “Haathi nikal gaya, dum reh gayi. (The elephant has left, just the tail is left).” I couldn’t have done this without you. Abbu: my dad has been a stalwart supporter and down to earth motivator. He always reminds me to focus on the task at hand, and to put forth my best effort. Abbu-jee, I still remember the poem you told me: “Girte hain shahsawar hi maidan-e-jung mein / Woh tifl kya gire jo ghutno ke bal chale. (Royal riders fall in the plain of battle / How would that child, crawling on its knees, ever fall?). My brothers, Ammar and Sharjeel: I love seeing you guys when I come to St. Louis. Thanks for always taking such a keen interest in whatever I tell you about my research and for just being a joy to be around.

Last but not least, I need to thank my wife, the incomparable Mrs. Meena Malik. It’s impossible to quantify your support and patience for the last three and a half years in this Ph.D. process. Throughout all the ups and downs, you’ve been there. You’ve believed in me when I doubted myself. I couldn’t have done this without you.

TABLE OF CONTENTS

PREFACE

Chapters from this dissertation were reproduced in part from the following published works:

1. Zahid MU & Smith AM Single-molecule imaging with quantum dots. in *Optical Nanoscopy and Novel Microscopy Techniques* (ed. Xi, P.) pp. 135–160 (CRC Press, 2014).
2. Lim SJ, Zahid MU, Le P, Ma L, Entenberg D, Harney AS, Condeelis J, Smith AM. Brightness-equalized quantum dots. *Nat. Commun.* **6,** 8210 (2015).
3. Ma L, Tu C, Le P, Chitoor S, Lim SJ, Zahid MU, Teng KW, Ge P, Selvin PR, Smith AM. Multidentate Polymer Coatings for Compact and Homogeneous Quantum Dots with Efficient Bioconjugation. *J. Am. Chem. Soc.* **138,** 3382–3394 (2016).
4. Zahid MU, Ma L, Lim SJ, Smith AM.. Single quantum dot tracking reveals the impact of nanoparticle surface on intracellular state. *Nat. Commun.* **9,** 1830 (2018).

CHAPTER 1: INTRODUCTION

1.1 Introduction

Quantum dots (QDs) are semiconductor nanocrystals with unique optical and electronic properties.[1,2] Originally investigated as components for light-emitting devices, solar cells, and catalysts in the early 1980's, these particles were introduced in 1998 as optical tags for bioimaging and biological detection.[3,4] The most significant contribution of QDs to biomedicine has been in the field of single-molecule fluorescence microscopy, for which they have filled a major need for bright fluorescent probes with long-term photostability. These particles are now widely used for imaging the dynamics of individual molecules and the interactions between molecules in complex biological environments.

In this chapter, we first describe the structure and optical properties of QDs. We then explore recent biological questions that have been answered through the implementation of QDs as single-molecule emitters, and finally we explore the challenges in delivering QDs into the intracellular space for single-molecule studies of live cells.

1.2 Quantum Dot Structure and Optical Properties

1.2.1 Quantum Dot Structure

Figure 1.1 depicts a prototypical QD used in single molecule imaging. The core is a nanocrystal composed of a semiconductor material such as cadmium selenide (CdSe) with a diameter of 2-6 nm, surrounded by an insulating crystalline shell of cadmium sulfide (CdS) and/or zinc sulfide (ZnS). Fluorescence and light absorption primarily take place in the core; the shell serves to enhance and protect the optical and electronic properties of the QD.[5,6] The crystalline surface facets are coated with organic ligands and/or polymers that stabilize the nanocrystal as a colloidal suspension in biological media and prevent nonspecific adhesion to proteins and cellular structures. These outer layers can be specifically tagged with biomolecules such as peptides, nucleic acids, and small molecule ligands. The most commonly used tagging strategy is based on QDs covalently conjugated to streptavidin, a modular protein adaptor that binds with high affinity to the small molecule biotin, which is readily linked to various biomolecules such as antibodies (see Figure 1.1).[7,8]

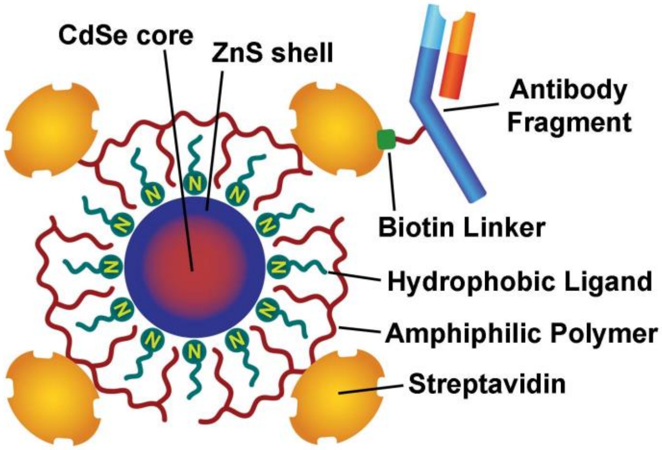

Figure 1.1 Structure of a prototypical streptavidin-coated QD. See text for details.[9]

1.2.2 Photophysical Properties

The most distinctive feature of a QD is its size-tunable fluorescence color (see Figure 1.2a-b). If the QD length dimensions are near to or smaller than a critical threshold (the Bohr exciton diameter), then the QD is within the “quantum confinement regime”.[2] In this size range, the wavelength of fluorescence emission is determined by the nanocrystal size. In the process of fluorescence, a ground state QD first absorbs an incident photon which excites an electron to a higher energy electronic state. This leaves behind an empty electronic orbital that behaves like a positively charged particle analogous to the negatively charged electron. When the electron and hole recombine, their energy is converted into a fluorescent photon. The conversion efficiency, or quantum yield (QY), is the number of photons emitted divided by the number of photons absorbed, and this value is largely a factor of the quality and thickness of the inorganic shell.

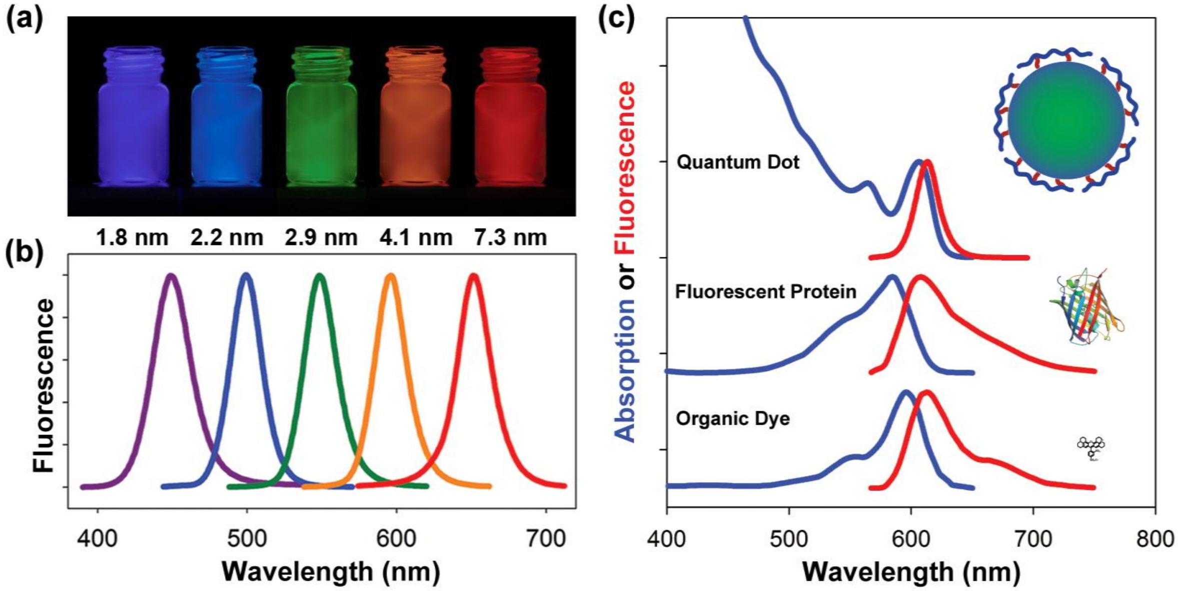

Figure 1.2. Optical properties of QDs. (a) Vials containing 5 sizes of QDs composed of CdSe dissolved in solution are illuminated with an ultraviolet lamp. (b) Fluorescence spectra of QDs depicted in (a). (c) Absorption spectra (blue) and fluorescence spectra (red) of QDs are compared with those of a fluorescent protein (mCherry) and an organic dye (Texas Red), showing the broad absorption spectra of QDs and narrow and symmetric fluorescence spectra of QDs. The relative sizes of these fluorescent labels are depicted next to their optical spectra.[10]

1.2.3 Comparison with other Fluorophores

Four key attributes of QDs are particularly advantageous for single-molecule imaging applications relative to other fluorescent reporters such as organic dyes, fluorescent proteins, and fluorescent beads. First, their fluorescence brightness is 10-100x greater than that of organic dyes and proteins, which results in a higher signal-to-noise ratio with decreased excitation power requirements.[3] This effect arises from the crystalline nature of these materials, in which hundreds to thousands of bonding electrons collectively oscillate to generate massive extinction coefficients, compared with just tens of electrons in organic dyes and proteins. Second, their emission stability is 100-1000x greater than that of other fluorophores, which enables long-term tracking of single molecules without signal decay.[3,4,7] This attribute derives from the insulating shell, as the QD can withstand oxidation or decomposition of many bonds without detriment to the sensitive core bonds in which absorption and emission take place. This is in contrast to organic dyes and proteins, for which breaking a single bond will lead to often irreversible fluorescence quenching. These first two attributes are also characteristic of some fluorescent beads, however QDs provide this in a much more compact form (beads are generally an order of magnitude larger; see section 1.3).

Third, QD fluorescence emission bands are narrow and symmetric and their excitation bands are broad (see Figure 2c), which allows for the simultaneous excitation of many fluorescence colors with little color crosstalk compared to conventional fluorophores. Fourth, their color is readily tuned over a broad spectrum by adjusting either the particle size or composition, spanning wavelengths of 300-5000 nm, far beyond what is possible with conventional fluorophores. Collectively these attributes are responsible for the capacity to image and track multiple distinct colors of individual particles for long durations in complex oxidizing environments. QDs can also be synthesized with a wide range of sizes, shapes, compositions, and composite structures, which allows for precise tuning of certain optical parameters (e.g. fluorescence lifetime and polarization) that cannot be predictably altered in conventional fluorophores. This tunability is possible due to the well-understood physical laws governing QDs derived from decades of study of semiconductor physics, and this tunability has been an enabling feature in for their implementation in advanced microscopy techniques.[2]

1.3 Novel Biological Phenomena

In 2003 and 2004, two seminal reports described the first use of QDs as probes for single molecules in living cells and demonstrated the major advantages of QDs over other available fluorophores.[11,12] In this section, we describe how QDs have become critical tools in the past decade for evaluating the dynamics and behavior of biological molecules and for revealing the organization and molecular heterogeneity of living cells and tissues.

1.3.1 Single-Molecule Dynamics

When QDs are bound to membrane proteins, motor proteins, or other biological molecules, patterns emerge from their spatial trajectories that can be used to deduce biomolecular behavior. In single-molecule trajectory analysis, the position of a single emitter in an image is first pinpointed in 2 dimensions (x, y) by calculating the centroid of the point spread function (PSF), and its displacement is calculated between sequential image frames. Trends in molecular behavior can be found from the mean of the squared displacement (*MSD*) for a time lag τ:

$$MSD(\tau) = \langle [x(\tau + t_0) - x(t_0)]^2 + [y(\tau + t_0) - y(t_0)]^2 \rangle \qquad (1.1)$$

where x and y denote the position of the particle of interest at a given time, and the angled brackets denote a combined average over all increments of time τ. When MSD values are plotted as a function of τ, a linear plot indicates random Brownian motion, while a plot with a decreasing slope indicates confined motion and a plot with an increasing slope indicates motion with a preferred directional orientation (see Figure 1.3).

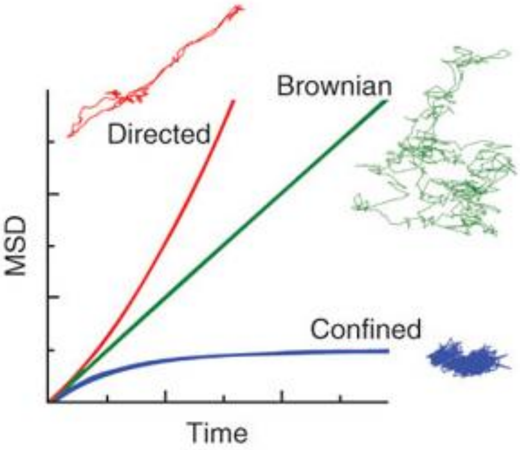

Figure 1.3. A plot of MSD values as a function of time increment that shows the differences between Brownian motion, directed motion, and confined motion.[13]

For Brownian motion in 2 dimensions, the MSD plot yields the *diffusion coefficient* (*D*) by the following equation:

$$\lim_{\tau \to 0} MSD(\tau) = 4D\tau \qquad (1.2)$$

The trajectory data can also be used to calculate an *instantaneous diffusion coefficient* (D_{inst}), by averaging only over a few time points to determine if the molecule diffuses into regions with different local environments with characteristic viscosities. Alternatively, *MSD* curves can be fit to different diffusion models, with model selection being dependent on *a priori* knowledge about the system or statistical comparisons to see which model is best suited for the system.[14] QDs are particularly effective for D_{inst} calculations because their brightness offers a greater signal-to-noise ratio, which allows for more accurate reconstruction of the PSF, low localization error, and long duration tracking. In contrast, organic dyes can only be tracked for a few seconds before irreversible photobleaching eliminates the fluorescent signal, and they require much higher excitation intensity for detection, which can be detrimental to cellular health.

1.3.2 Imaging and Tracking of Membrane Proteins

The plasma membrane is a heterogeneous, dynamically changing structure that regulates the exchange of energy and matter between the cell and the surrounding medium, integrates the cell's mechanical components with the extracellular matrix, and senses environmental change. Membrane proteins that mediate these effects exhibit complex behaviors that remain poorly understood. Membrane protein-bound QDs have recently played a key role in elucidating membrane protein function, especially for detecting molecular confinement in membrane subdomains, and the field of neuronal biology has been one of the greatest beneficiaries of this work.[15–17] Using QD-tagged receptors for neurotransmitters, receptor behaviors have been shown to differ when they are within the neuronal synapse compared to when they diffuse out of the synapse, and long-term imaging has allowed observation of the entire endocytosis/exocytosis receptor recycling process.[12,18] These observations have revealed distinct receptor behaviors in the presence of neuromodulatory drugs.[19,20] QD studies of plasma membrane proteins have connected short-term single-molecule dynamics with long-term molecular behavior that previously had not been possible. For example, QD-tagged receptors for the neurotransmitter gamma-aminobutyric acid (GABA) were shown to redistribute in the presence of an extracellular gradient of GABA to amplify gradient sensing for nerve growth cone signaling.[21] The retrograde transport of vesicles containing individual dimers of nerve growth factor (NGF) has been observed across the entire length of axons to the soma.[22] Growth factor receptor dynamics have also been explored in a variety of other cellular systems, and the multicolor imaging capability of QDs has played a key role in understanding the dimerization of the epidermal growth factor receptor and its transport in the cell after binding to its cognate receptor EGF. [23,24]

1.3.3 Motor Protein Imaging

Motor proteins are enzymes that convert chemical energy from ATP into mechanical motion to power directional translocation along a substrate. The cytoskeletal motor proteins myosin, dynein, and kinesin traverse cytoskeletal tracks to perform a variety of cellular functions such as intracellular cargo delivery and cellular division. Specific modes of motion of these proteins have been established *in vitro* using purified proteins tagged with QDs, but it is a major challenge to deliver QDs into live cells for *in vivo* verification. Intracellular delivery mechanisms include microinjection, electroporation, osmotic rupture of endosomes, or cationic lipid transfection, each of which has certain limitations.[10] However studies have confirmed that QD-motor protein conjugates exhibit similar behaviors for both kinesin and myosin Va inside and outside of cells.[25–27] Nucleic acid motors are a second class of enzymes that include polymerases, helicases, topoisomerases, and other enzymes involved in the maintenance, repair, and replication of genetic material. The multicolor imaging capacity of QD probes has been used to image and map the binding of these proteins to DNA with nanometer-scale resolution, which allows precise mapping of enzyme binding locations, such as promoters, across entire genomes.[28]

QDs have also been instrumental in determining how enzymes that are not powered by ATP efficiently scan through entire genomes to find their target sequence. Simple calculations show that 3D diffusion of enzymes and random attachment to DNA alone would not provide the efficiency necessary for genomic maintenance and repair. Single-QD imaging has revealed that enzymes such as EcoRV, UvrA, UvrB, and N-glycosylases randomly attach to DNA but then slide along the DNA while rotating with the helix to scan for their targets.[29–31] This 1D search process powered by thermal fluctuations is much more efficient than a random-attachment search.

1.4 Challenge of Intracellular Delivery

It has been a major challenge to adopt QD-based single-molecule live-cell imaging to intracellular targets due to the difficulty in homogeneously transporting these nanoparticles to the cytoplasm. This mirrors ongoing challenges in the field of gene and antibody therapeutics, for which inefficient macromolecular transport continues to be a critical barrier to effective use.[32,33] A multitude of techniques have been developed using chemical carriers such as peptides,[34,35] proteins,[11,36] polymers,[37,38] and lipids, but the vast majority of payload remains trapped in endocytotic vesicles and aggregated.[39] Single-cell microinjection[39,40] can be effective but its exceptionally low throughput is problematic,[41] and membrane pore-inducing methods using electroporation[42,43] and streptolysin toxins[44–46] can substantially alter cell physiology. Importantly, even when cytosolic delivery is observed using these methods, it is exceptionally challenging to definitively and quantitatively establish whether intracellular cargo is free or bound, and independent or aggregated. There have been recent developments of even gentler techniques such as cell squeezing[47], and photoporation[48,49], and it will be imperative to evaluate if these techniques can be used to effectively deliver single QDs to the intracellular space.

1.5 Conclusions

QDs have made an important impact in the past decade in understanding complex processes intrinsic to biology with one of the primary areas of impact being measurements of single-molecule dynamics, which have been made possible by the unique optical properties of QDs. However, the use of QDs in applications for single-molecule biology applications has largely been limited to the study of either fixed cells or the extracellular space of living cells. This has primarily been limited by the challenges in delivering nanoparticles to the cytosol of live cells, but with advancement of intracellular delivery techniques, QDs are poised to reveal intracellular single-molecule dynamics underlying various subcellular signaling and trafficking processes.

1.6 References

1. Smith, A. M., Duan, H., Mohs, A. M. & Nie, S. Bioconjugated quantum dots for in vivo molecular and cellular imaging. *Adv. Drug Deliv. Rev.* **60,** 1226–1240 (2008).
2. Smith, A. M. & Nie, S. Semiconductor nanocrystals: structure, properties, and band gap engineering. *Acc. Chem. Res.* **43,** 190–200 (2009).
3. Chan, W. C. W. & Nie, S. Quantum dot bioconjugates for ultrasensitive nonisotopic detection. *Science* **281,** 2016–2018 (1998).
4. Bruchez, M., Moronne, M., Gin, P., Weiss, S. & Alivisatos, A. P. Semiconductor nanocrystals as fluorescent biological labels. *Science* **281,** 2013–2016 (1998).
5. Dabbousi, B. O. *et al.* (CdSe) ZnS core-shell quantum dots: synthesis and characterization of a size series of highly luminescent nanocrystallites. *J. Phys. Chem. B* **101,** 9463–9475 (1997).
6. Lim, S. J. *et al.* Brightness-equalized quantum dots. *Nat. Commun.* **6,** 8210 (2015).
7. Wu, X. *et al.* Immunofluorescent labeling of cancer marker Her2 and other cellular targets with semiconductor quantum dots. *Nat. Biotechnol.* **21,** 41–46 (2002).
8. Goldman, E. R. *et al.* Avidin: a natural bridge for quantum dot-antibody conjugates. *J. Am. Chem. Soc.* **124,** 6378–6382 (2002).
9. Zahid, M. & Smith, A. Single-molecule imaging with quantum dots. in *Optical Nanoscopy and Novel Microscopy Techniques* (ed. Xi, P.) 135–160 (CRC Press, 2014).
10. Smith, A. M., Wen, M. M. & Nie, S. Imaging dynamic cellular events with quantum dots The bright future. *Biochem. (Lond).* **32,** 12 (2010).
11. Lidke, D. S. *et al.* Quantum dot ligands provide new insights into erbB/HER receptor--mediated signal transduction. *Nat. Biotechnol.* **22,** 198–203 (2004).
12. Dahan, M. *et al.* Diffusion dynamics of glycine receptors revealed by single-quantum dot tracking. *Sci. Signal.* **302,** 442 (2003).
13. Pinaud, F., Clarke, S., Sittner, A. & Dahan, M. Probing cellular events, one quantum dot at a time. *Nat. Methods* **7,** 275–285 (2010).
14. Monnier, N. *et al.* Bayesian approach to MSD-based analysis of particle motion in live cells. *Biophys. J.* **103,** 616–626 (2012).
15. Pinaud, F. & Dahan, M. Targeting and imaging single biomolecules in living cells by complementation-activated light microscopy with split-fluorescent proteins. *Proc. Natl. Acad. Sci.* **108,** E201–E210 (2011).
16. Crane, J. M., Van Hoek, A. N., Skach, W. R. & Verkman, A. S. Aquaporin-4 dynamics in

orthogonal arrays in live cells visualized by quantum dot single particle tracking. *Mol. Biol. Cell* **19,** 3369–3378 (2008).

17. Crane, J. M. & Verkman, A. S. Long-range nonanomalous diffusion of quantum dot-labeled aquaporin-1 water channels in the cell plasma membrane. *Biophys. J.* **94,** 702–713 (2008).
18. Groc, L. *et al.* Surface trafficking of neurotransmitter receptor: comparison between single-molecule/quantum dot strategies. *J. Neurosci.* **27,** 12433–12437 (2007).
19. Mikasova, L., Groc, L., Choquet, D. & Manzoni, O. J. Altered surface trafficking of presynaptic cannabinoid type 1 receptor in and out synaptic terminals parallels receptor desensitization. *Proc. Natl. Acad. Sci.* **105,** 18596–18601 (2008).
20. Porras, G. *et al.* PSD-95 expression controls l-DOPA dyskinesia through dopamine D1 receptor trafficking. *J. Clin. Invest.* **122,** 3977 (2012).
21. Bouzigues, C., Morel, M., Triller, A. & Dahan, M. Asymmetric redistribution of GABA receptors during GABA gradient sensing by nerve growth cones analyzed by single quantum dot imaging. *Proc. Natl. Acad. Sci.* **104,** 11251–11256 (2007).
22. Cui, B. *et al.* One at a time, live tracking of NGF axonal transport using quantum dots. *Proc. Natl. Acad. Sci.* **104,** 13666–13671 (2007).
23. Kawashima, N. *et al.* Reversible Dimerization of EGFR Revealed by Single-Molecule Fluorescence Imaging Using Quantum Dots. *Chem. – A Eur. J.* **16,** 1186–1192 (2010).
24. Lidke, D. S., Lidke, K. A., Rieger, B., Jovin, T. M. & Arndt-Jovin, D. J. Reaching out for signals: filopodia sense EGF and respond by directed retrograde transport of activated receptors. *Sci. Signal.* **170,** 619 (2005).
25. Courty, S., Luccardini, C., Bellaiche, Y., Cappello, G. & Dahan, M. Tracking individual kinesin motors in living cells using single quantum-dot imaging. *Nano Lett.* **6,** 1491–1495 (2006).
26. Nelson, S. R., Ali, M. Y., Trybus, K. M. & Warshaw, D. M. Random walk of processive, quantum dot-labeled myosin Va molecules within the actin cortex of COS-7 cells. *Biophys. J.* **97,** 509 (2009).
27. Katrukha, E. A. *et al.* Probing cytoskeletal modulation of passive and active intracellular dynamics using nanobody-functionalized quantum dots. *Nat. Commun.* **8,** 14772 (2017).
28. Ebenstein, Y. *et al.* Lighting up individual DNA binding proteins with quantum dots. *Nano Lett.* **9,** 1598–1603 (2009).
29. Dikić, J. *et al.* The rotation-coupled sliding of EcoRV. *Nucleic Acids Res.* **40,** 4064–4070 (2012).
30. Dunn, A. R., Kad, N. M., Nelson, S. R., Warshaw, D. M. & Wallace, S. S. Single Qdot-labeled glycosylase molecules use a wedge amino acid to probe for lesions while scanning along DNA. *Nucleic Acids Res.* **39,** 7487–7498 (2011).
31. Kad, N. M., Wang, H., Kennedy, G. G., Warshaw, D. M. & Van Houten, B. Collaborative dynamic DNA scanning by nucleotide excision repair proteins investigated by single-molecule imaging of quantum-dot-labeled proteins. *Mol. Cell* **37,** 702–713 (2010).
32. Miyata, K., Nishiyama, N. & Kataoka, K. Rational design of smart supramolecular assemblies for gene delivery: chemical challenges in the creation of artificial viruses. *Chem. Soc. Rev.* **41,** 2562–2574 (2012).
33. Zhang, Y., Satterlee, A. & Huang, L. In Vivo Gene Delivery by Nonviral Vectors: Overcoming Hurdles? *Mol. Ther.* **20,** 1298–1304 (2012).
34. Ruan, G., Agrawal, A., Marcus, A. I. & Nie, S. Imaging and tracking of tat peptide-

conjugated quantum dots in living cells: new insights into nanoparticle uptake, intracellular transport, and vesicle shedding. *J. Am. Chem. Soc.* **129,** 14759–14766 (2007).

35. Silver, J. & Ou, W. Photoactivation of quantum dot fluorescence following endocytosis. *Nano Lett.* **5,** 1445–1449 (2005).
36. Qian, J. *et al.* Imaging pancreatic cancer using surface-functionalized quantum dots. *J. Phys. Chem. B* **111,** 6969–6972 (2007).
37. Dudu, V., Ramcharan, M., Gilchrist, M. L., Holland, E. C. & Vazquez, M. Liposome delivery of quantum dots to the cytosol of live cells. *J. Nanosci. Nanotechnol.* **8,** 2293–2300 (2008).
38. Voura, E. B., Jaiswal, J. K., Mattoussi, H. & Simon, S. M. Tracking metastatic tumor cell extravasation with quantum dot nanocrystals and fluorescence emission-scanning microscopy. *Nat. Med.* **10,** 993–998 (2004).
39. Medintz, I. L. *et al.* Intracellular delivery of quantum dot− protein cargos mediated by cell penetrating peptides. *Bioconjug. Chem.* **19,** 1785–1795 (2008).
40. Dubertret, B. *et al.* In vivo imaging of quantum dots encapsulated in phospholipid micelles. *Science* **298,** 1759–1762 (2002).
41. Okada, C. Y. & Rechsteiner, M. Introduction of macromolecules into cultured mammalian cells by osmotic lysis of pinocytic vesicles. *Cell* **29,** 33–41 (1982).
42. Chen, F. & Gerion, D. Fluorescent CdSe/ZnS nanocrystal-peptide conjugates for long-term, nontoxic imaging and nuclear targeting in living cells. *Nano Lett.* **4,** 1827–1832 (2004).
43. Sun, C., Cao, Z., Wu, M. & Lu, C. Intracellular tracking of single native molecules with electroporation-delivered quantum dots. *Anal. Chem.* **86,** 11403–11409 (2014).
44. Fu, A. *et al.* Semiconductor quantum rods as single molecule fluorescent biological labels. *Nano Lett.* **7,** 179–182 (2007).
45. Agrawal, A. & Nie, S. Real-time detection of single quantum dots inside living cells. *Proc. SPIE* **5705,** 152–158 (2005).
46. Teng, K. W. *et al.* Labeling proteins inside living cells using external fluorophores for microscopy. *eLife* **5,** e20378 (2016).
47. Kollmannsperger, A. *et al.* Live-cell protein labelling with nanometre precision by cell squeezing. *Nat. Commun.* **7,** 10372 (2016).
48. Liu, J. *et al.* Repeated photoporation with graphene quantum dots enables homogeneous labeling of live cells with extrinsic markers for fluorescence microscopy. *Light Sci. Appl.* **7,** 47 (2018).
49. Xiong, R. *et al.* Comparison of gold nanoparticle mediated photoporation: vapor nanobubbles outperform direct heating for delivering macromolecules in live cells. *ACS Nano* **8,** 6288–6296 (2014).

CHAPTER 2: SINGLE QUANTUM DOT TRACKING TO ASSESS CYTOPLASMIC DELIVERY

2.1 Background

2.1.1 Motivation

With the development of new pharmaceutical agents there is a need to deliver macromolecules, biologics, and nanoparticles to intracellular targets. However, processes for delivery to the cytoplasm are both inefficient and poorly understood.[1–5] Furthermore, current approaches to asses these delivery methods rely either on indirect end-point measurements that don't allow for the direct interrogation of mechanisms or on ensemble-level measurements that mask single-molecule heterogeneity.[6–9] Traditional methods to explore mechanisms include fractionation of cell populations to isolate intracellular components, and fixation of cells followed by optical or electron microscopy.[6] However, the harshness of these treatments has been widely observed to introduce artifacts, including fixation-induced translocation of exogenous nanoparticles that misled the nanomedicine community for years.[10,11] These limitations make it impossible to understand intracellular delivery mechanisms and to subsequently improve these delivery techniques.

Live-cell fluorescence imaging has generated some of the most crucial insights in cell biology due to the ability to localize specific molecules with high resolution during physiological processes.[12–15] A major current goal is to analyze the dynamics of individual molecules to discern the heterogeneity and mechanisms of molecular processes underlying emergent behaviors at the finest level of detail.[16–18] However traditional fluorescence probes based on organic molecules (fluorescent dyes and fluorescent proteins) are limited in both their duration and intensity of light emission. Semiconductor quantum dots (QDs) have been pinpointed as a next-generation emitter for these applications due to their extraordinary stability and bright emission at the single-molecule level.[19–22] Previous limitations of large size and molecular specificity have recently been addressed and QDs are now a key tool for analyzing membrane proteins and dynamic processes in cell environments.[23–25]

In this chapter we present a method for using single-molecule imaging and subsequent single-particle tracking (SPT) of quantum dots (QDs) delivered to the cytosol of living cells to assess delivery efficacy and mechanisms. In this method, single quantum dot track information was used in conjunction with single-molecule brightness measurements in order to develop novel single-cell metrics of delivery efficiency.

2.1.2 Delivery Approach

To develop our analysis technique, we focused on one method of delivering QDs to the cell cytosol: osmotic pinosome lysis (OPL), a two-step delivery process that manipulates extracellular tonicity and natural mechanisms of fluid-phase pinocytosis.[26] The first step of OPL is to expose cultured cells to the macromolecules or nanoparticles to be delivered mixed with a hypertonic delivery media composed of PEG and sucrose. Exposure to this delivery media triggers fluid-phase pinocytosis by which the cells internalize the nanoparticle payload. The second step of OPL is a brief exposure of the cells to a hypotonic media, compose of incomplete cell culture media diluted with deionized water. This triggers the rupture of pinosomes and subsequent release of the payload into the cytoplasm (Figure 2.1a). Cell volume changes and membrane “ruffling” indicating pinocytosis were verified by brightfield microscopy (Fig. 2.1b).

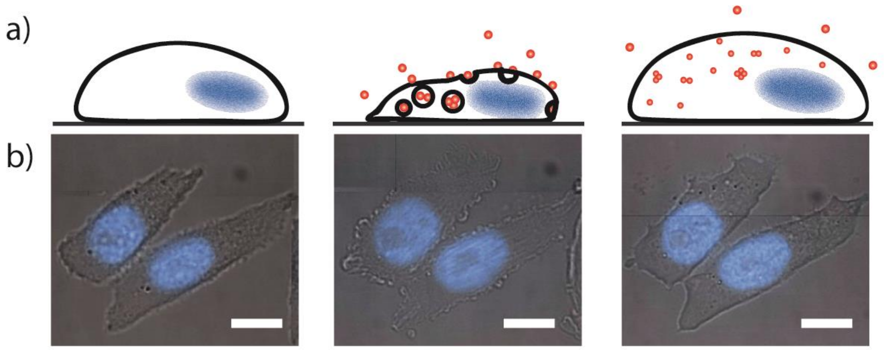

Figure 2.1. Characterization of QD delivery by OPL in CHO cells. (a) Schematic of OPL depicting changes in cell morphology and location of QDs for cells prior to treatment (left), during hypertonic loading of QDs (middle), and after hypotonic treatment to rupture pinosomes (right). (b) Brightfield images with nuclear stain (blue) demonstrating morphological changes of cells undergoing OPL, at stages corresponding to schematics in (a). Scale bars are 10 μm.

The proposed mechanism of OPL was further verified at the different steps by examining subcellular QD location an internalization by transmission electron microscopy (TEM) of silver developed QDs (Fig. 2.2).).

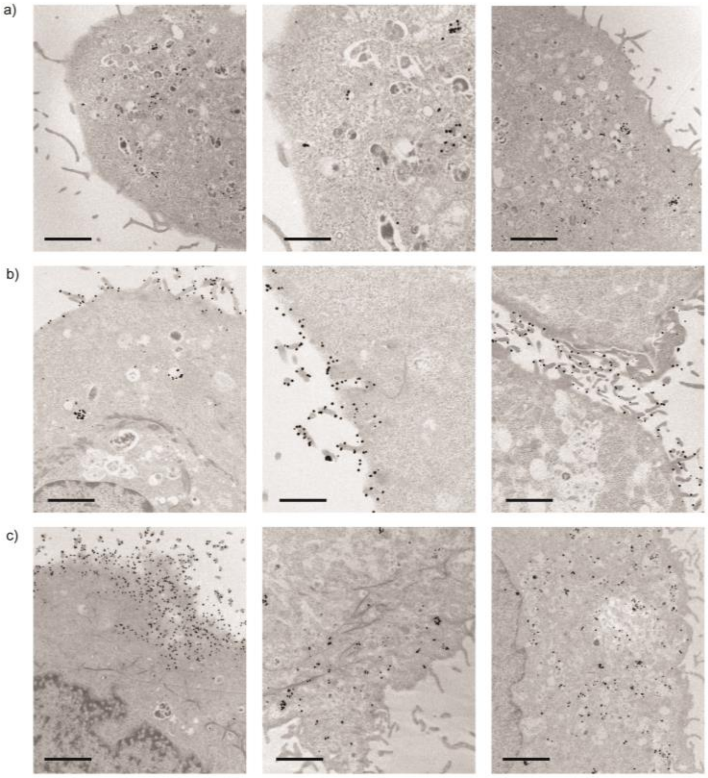

Figure 2.2. TEM images of mPEG-QD delivery to A431 cells. QDs were developed with silver to increase nanoparticle contrast.[27] (a) Cells exposed to QDs in complete medium show QDs primarily trapped in endosomes. (b) Cells exposed to QDs in hypertonic loading buffer, showing QDs trapped in pinosomes, adhering to the cell membrane, and localized in gaps between cells. (c) Cells exposed to QDs in hypertonic loading buffer, followed by addition of hypotonic lysis buffer, showing QDs in the cytoplasm near the cell membrane and further inside the cell. All scale bars indicate 2 μm.

Compared to other delivery approaches, the primary advantage of OPL is that it is relatively high throughput, allowing for delivery to whole wells of cells simultaneously. Further, if exposure to the hypertonic delivery media and the hypotonic lysis media is limited, OPL has relatively low cytotoxicity. This was confirmed by both cell viability assays and live/dead imaging as summarized in Figure 2.3.

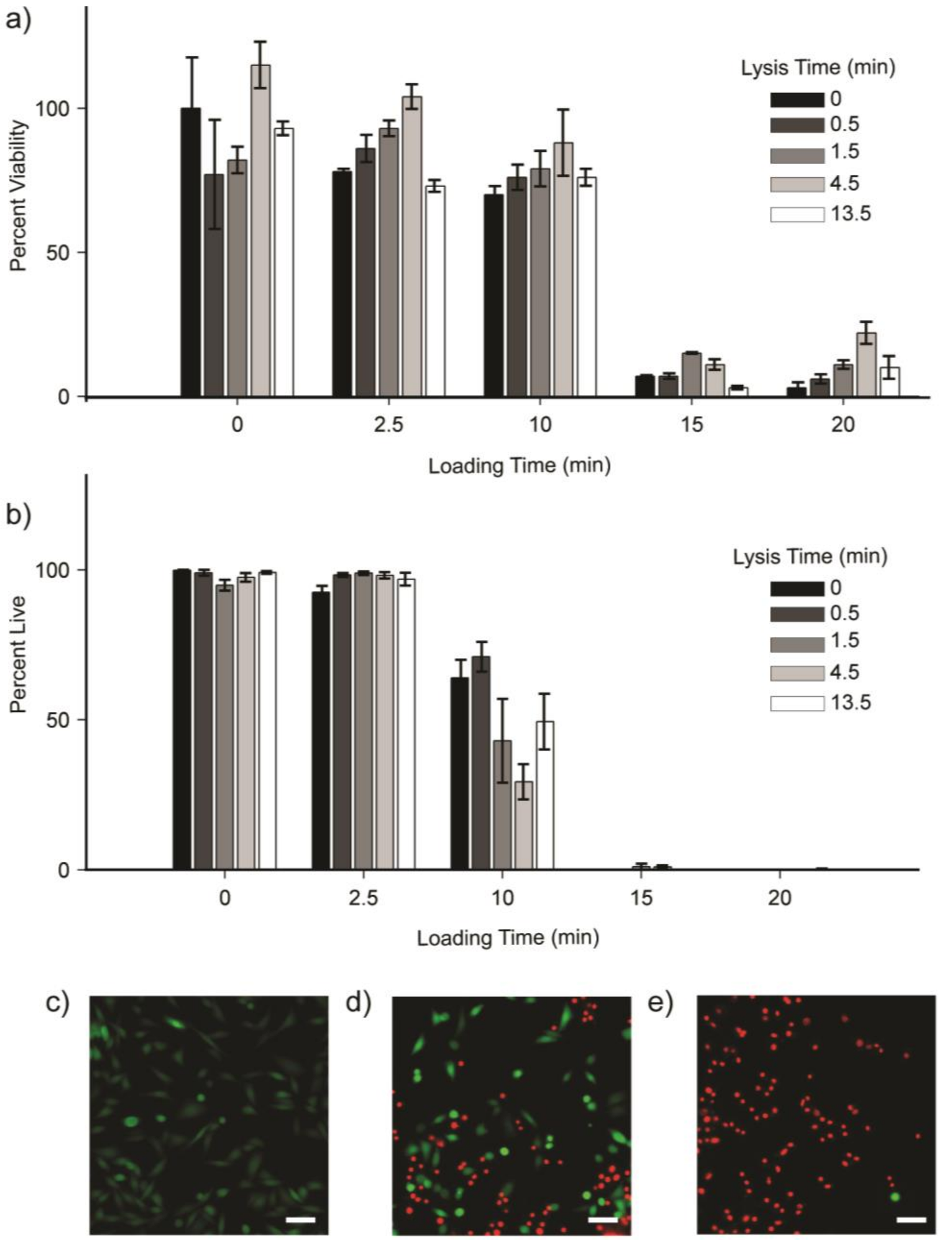

Figure 2.3. Live/dead and viability after loading and lysis treatments. (a) CCK-8 viability assay for the indicated loading and lysis times. (b) Live/dead analysis using Calcein AM and EtH-1 for the indicated loading and lysis times. n = 3 for all experimental conditions. Error bars in panels (a) and (b) indicate s.e.m. Sample images depict loading times of (c) 2.5, (d) 10, and (e) 15 min, all with 1.5 min lysis. All scale bars indicate 50 μm.

2.1.3 Imaging Approach

In order to perform single-molecule imaging of cytoplasmic QDs, we utilized highly-inclined laminar optical sheet (HILO) microscopy. HILO microscopy provides similar signal-to-noise ratio and fast wide-field acquisition to traditional total internal reflection fluorescence (TIRF) microscopy.[28] However, HILO allows for the acquisition of images at distances greater than 100-200 nm above the coverslip-cell interface.[28]

Since we're using HILO, in order to ensure that we were only imaging and QDs in the intracellular space, a cell membrane impermeant QD-quencher was utilized. In this case, we used bromocresol green (BCG), which has strong absorbance around 600 nm that allows it to quench emitted fluorescence light of the QDs being used in this study. As shown by Valentine, et. al., BCG does not cross the cell membrane, and it requires access to the surface of the QD in order to quench its emission.[29] This combination of properties allows BCG to serve as an extracellular quencher, which lets us ensure that we're imaging intracellular QDs exclusively.

2.2 Data and Results

2.2.1 Analysis Methodology

After obtaining HILO fluorescence microscopy movies of intracellular QDs delivery by OPL, we preformed single-particle tracking analyzing using the previously mentioned u-Track algorithm.[30] The resulting single-particle trajectories were then analyzed by two routes: (1) diffusion analysis and (2) single-molecule optical analysis.

2.2.1.1 Mobility Analysis

As previously described, mean-square displacement (MSD) analysis is a powerful tool to study the random motion of particles that is often used to interpret SPT results. A common model for intracellular diffusion is the anomalous diffusion model, which is given as

$$MSD(\tau) = 4D\tau^{\alpha}, \tag{2.1}$$

where $MSD(\tau)$ is the mean squared displacement as a function of time lag, τ, D is the diffusion coefficient and α is a unitless confinement parameter. In the anomalous diffusion model, when α is equal to 1, then the model simplifies to the Brownian diffusion model; when $\alpha < 1$, then this indicates a subdiffusion or a level of confinement that is typical of the behavior seen in the cytoplasm due to macromolecular crowding; and when $\alpha > 1$, this indicates some form of superdiffusion or directed motion, often arising from motor proteins or similar subcellular mechanisms.[31,32] To make our model more complete and to account for the localization uncertainty of the SPT algorithm, the model had to be adjusted to

$$MSD(\tau) = 4D\tau^{\alpha} + 4\sigma_{xy}^{2}, \tag{2.2}$$

where σ_{xy} is the average localization error for each trajectory, which is an output parameter of the SPT algorithm. Addition of the localization error to the diffusion model was confirmed to be necessary, as when it was left out this led to the appearance of artifactual subpopulations at low alpha values, as shown in Figure 2.4.

a) $MSD(\tau) = 4D\tau^{\alpha}$

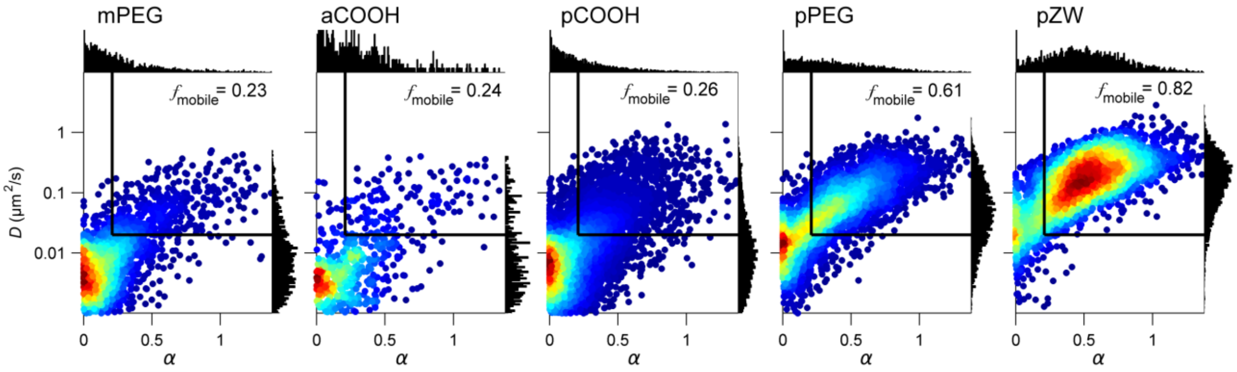

b) $MSD(\tau) = 4D\tau^{\alpha} + 4\sigma_{xy}^{2}$

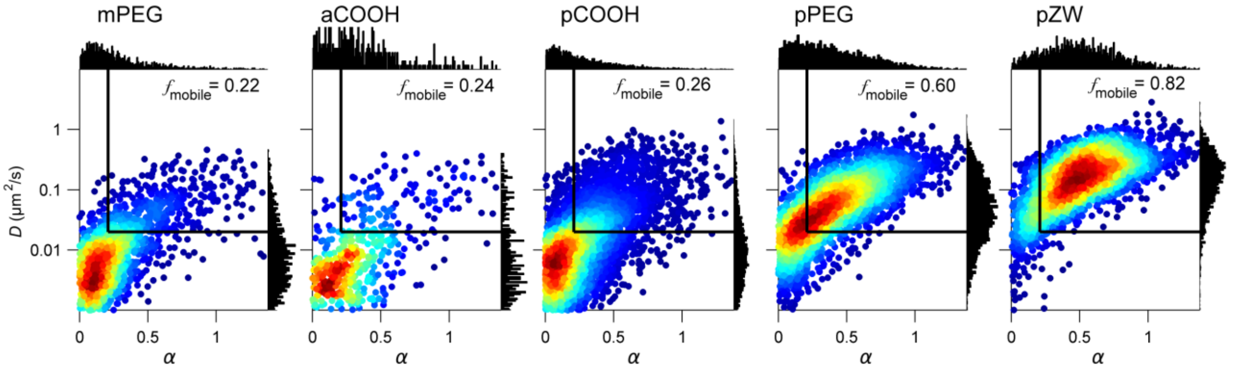

Figure 2.4. Localization error correction. Heat maps compare D versus α plots for intracellular QDs with 5 coatings, using the same data from Figure 4a in the main text. (a) Data derived from *MSD* fitting to the anomalous diffusion model without the localization error correction factor. (b) Data derived from *MSD* fitting to the anomalous diffusion model with the localization error correction factor.

Another aspect of the model that had to be optimized was the number of time lag points to fit to. Extensive analytical and simulation work has been done showing that careful selection of τ_{fit} is necessary for accurate D estimations.[33,34] Extensive recommendations have been for fitting to a Brownian motion models.[35,36] However, the literature reports on anomalous diffusion are more sparse. Kepten and colleagues recommend that τ_{fit} be fixed as 10 time lags for anomalous diffusion, given for tracks in the regime of strong subdiffusion to weak superdiffusion (α = 0.3-1.3) with low localization error.[37] However, given the nature of QDs diffusing in and out of the focal plane that yields many trajectories that are shorter than 100 frames, it was necessary to determine an alternative for such short trajectories. Thus, we used a variable definition for τ_{fit}, where τ_{fit} is 10 frames if the trajectory length is shorter than 100 frames and τ_{fit} is defined as ¼ of the total trajectory length.

2.2.1.2 Optical Analysis

Parallel to the diffusion analysis, single-molecule brightness values were analyzed to extract information about the number of QDs in a detected spot or trajectory. As the measured average size of a single QD is significantly smaller than the diffraction limit of 600 nm wavelength light, small clusters of QDs and single QDs would all appear as diffraction-limited spots in fluorescence microscopy. However, since the QDs synthesized in our lab have a relatively uniform and narrow distribution of brightness values when measured diffusing in glycerol (Fig 2.5), it's possible to infer the number of QDs present in a given spot or trajectory by evaluating the fluctuations in the single-molecule brightness.

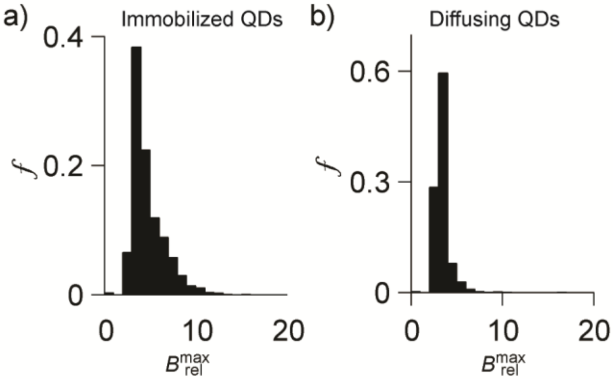

Figure 2.5. Distributions of maximum single-particle relative brightness ($B_{\mathrm{rel}}^{\mathrm{max}}$) for QDs (a) immobilized on a glass coverslip or (b) diffusing in 98% glycerol, demonstrating uniform brightness in a cell-free environment. *f* = frequency.

Brightness measurements were taken as previously described by averaging the intensity over a 3x3 pixel area centered on the tracked coordinates for each trajectory in each frame. From these intensity time traces, it was possible to extract the maximum relative brightness for each trajectory ($B_{\mathrm{rel}}^{\mathrm{max}}$).

A well-known property of single QDs is their fluorescence intermittency, also known as "blinking".[38] This property allows us to identify single QDs, as they exhibit a clear "off" stat and one "on" state at a single intensity, as opposed to clusters of QDs exhibit multiple "on" intensities (Fig 2.6).

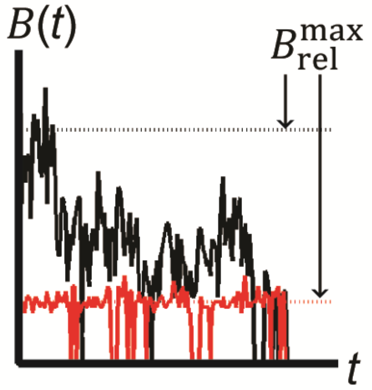

Figure 2.6. For optical analysis, the brightness per trajectory at each time point, $B(t)$, is analyzed to determine its maximum relative value, $B_{\mathrm{rel}}^{\mathrm{max}}$, to calculate the number of QDs per cluster, n_{QD}. Representative data show intensity time traces of a single QD (red) a QD cluster (black).

For each cell, the mean single-QD brightness (B_{rel}^{1}) could be calculated by identifying the center-value of the first peak in the corresponding $B_{\mathrm{rel}}^{\mathrm{max}}$ distribution by using the first derivative of this distribution, which is defined by the following equation:

$$B_{\mathrm{rel}}^{1} = \left(\frac{\mathrm{d}N}{\mathrm{d}B_{\mathrm{rel}}^{\mathrm{max}}}\right)_{0,1} \tag{2.3}$$

where N is the number of trajectories as a function of $B_{\mathrm{rel}}^{\mathrm{max}}$.

The calculated vale of B_{rel}^{1} could be used to convert all of the $B_{\mathrm{rel}}^{\mathrm{max}}$ values for that cell to the more concrete value of n_{QD}, the number of QDs in that trajectory, by the following formula:

$$n_{\mathrm{QD}} = \frac{B_{\mathrm{rel}}^{\mathrm{max}}}{B_{\mathrm{rel}}^{1}}, \tag{2.4}$$

2.2.1.3 Defining New Single-Cell Metrics

Using the trajectory-level information of D, α, and n_{QD} we were able to define a number of novel single-cell metrics to quantify the intracellular state of the delivered QDs in the terms of their mobility and clustering. These included the f_{mobile}, the fraction of mobile trajectories; f_1, the fraction of trajectories that consisted of single-QDs; and $f_{1,mobile}$, the fraction of trajectories that are both single-QDs and mobile. The relationship of these subsets to each other and which analysis methodology the derive from are summarized in Figure 2.7.

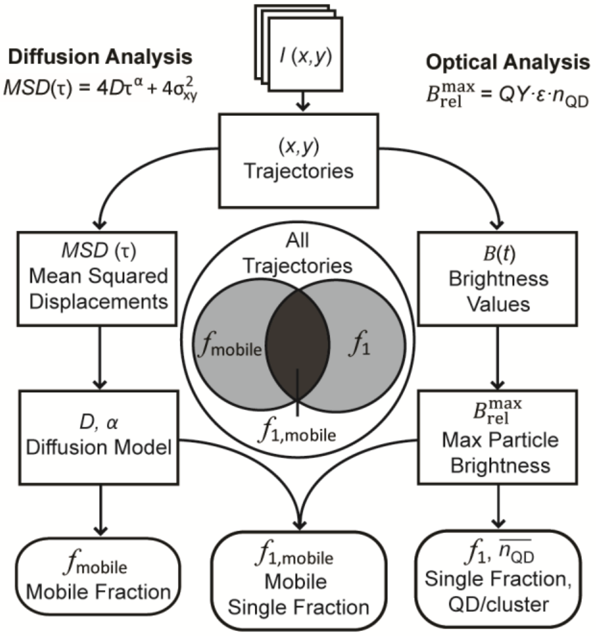

Figure 2.7. Schematic of combined single particle mobility and clustering analysis. Single particle trajectories (x(t),y(t)) are extracted from raw image stacks of I(x,y), and each trajectory is analyzed by diffusion (left) and optical metrics (right). For diffusion analysis, mean squared displacement (MSD) curves for each trajectory are fit to an anomalous diffusion model to yield a diffusion coefficient, D, and confinement parameter, α. These values for each trajectory are aggregated across all cells for a given experimental condition and thresholds are imposed to determine the mobile fraction, f_{mobile}. For optical analysis, the brightness per trajectory at each time point, B(t), is analyzed to determine its maximum relative value, B_{rel}^{max}, to calculate the number of QDs per cluster, n_{QD}. The distribution of all B_{rel}^{max} values for each cell is then analyzed to extract the fraction that is single, f_1, and the average number of QDs per cluster, $\overline{n_{QD}}$, and then aggregated across all cells for each experimental condition. The diffusion and optical analyses are then combined to analyze specific particle populations to determine the fraction that are both single and mobile, $f_{1,mobile}$, represented in the Venn diagram at center. Parameters in rectangles are determined for each trajectory, whereas parameters in rounded boxes are determined for a population of QDs in a one cell or multiple cells.

The mobile fraction, f_{mobile}, required the selection of threshold values for D and α above which a trajectory would be considered mobile and free to diffuse in the cytosol. These threshold values were set empirically by comparing the calculated D and α parameter distributions of QD immobilized on a coverslip to both QDs diffusing in an aqueous glycerol solution and QDs diffusing in the cell cytosol. HILO videos from all 3 conditions were processed as previously described to obtain fitted D and α values for all detected trajectories. Ultimately, the QD diffusing in the cell cytosol were used as the positive control, because detailed investigation showed that on average QDs diffusing in glycerol with similar diffusion coefficients stayed in the focal plan for shorter periods of time (Figure 2.8). This may be due to some sort of z-confinement provided by the cells.

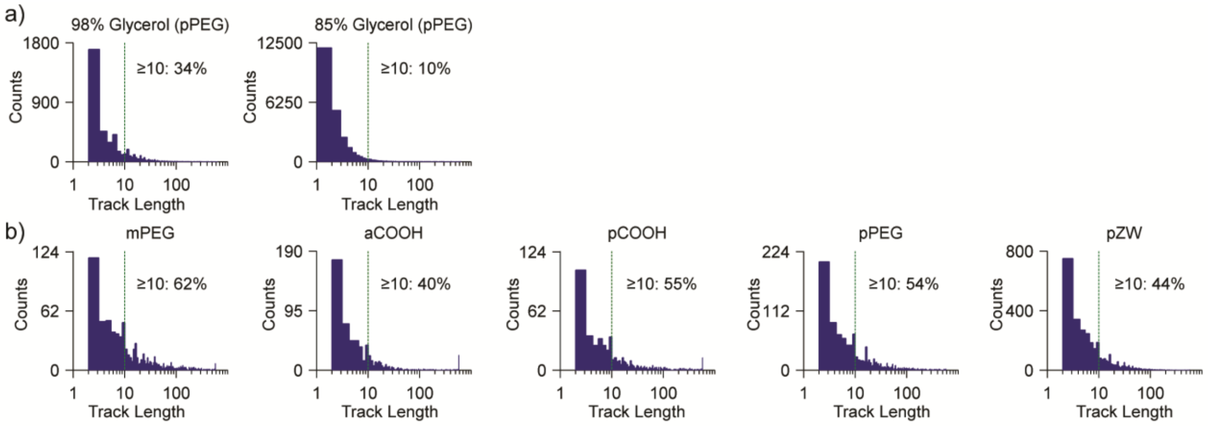

Figure 2.8. Track length histograms of QDs in glycerol solution or cells. (a) Track length distributions of QDs diffusing in aqueous solutions of glycerol with indicated glycerol weight percentage. The percentage of tracks longer than 10 frames is noted for both solutions. The reduced number of >10-frame tracks in the 85% glycerol solution sets a maximum value of measurable *D* by 2D SPT. (b) Track length distributions for QDs with the 5 different coatings in CHO cells. Note that the pZW-QD and pPEG-QD samples have higher measured *D* compared with QDs diffusing in 98% glycerol because they demonstrate a larger percentage of tracks longer than 10 frames, due to z-axis confinement. Data correspond to the same as that of Figure 4a-b.

One-dimensional receiver operator curve analysis was performed on the immobilized QDs and the pZW QDs in cells for both D and α and threshold of $D > 0.020$ $\mu m^2 s^{-1}$ and $\alpha > 0.21$ were set by finding the points that maximized sensitivity and specificity (Figure 2.9).

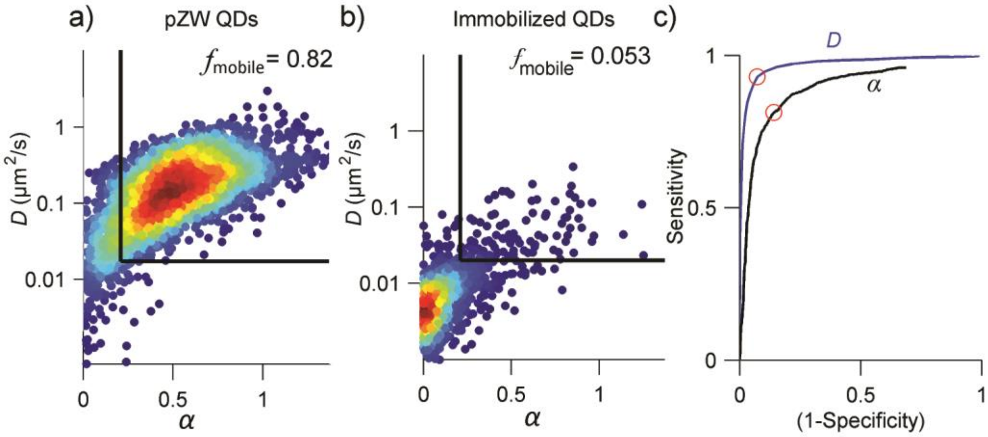

Figure 2.9. Receiver operator curve analysis. (a) Heat map of diffusion coefficient, D, versus confinement parameter, α for pZW-coated QDs in cell cytosol. Thresholds imposed for mobility are shown as black lines, yielding f_{mobile} shown in each plot. (b) Heat map of D versus α for immobilized QDs. (c) Receiver operating characteristic (ROC) curves distinguishing immobilized QDs from pZW-coated QDs in CHO cells, independently for D (blue) and α (black). Cutoffs that maximize both sensitivity and specificity (D > 0.020 µm^2 s^{-1} and α > 0.21) are marked by red circles.

The fraction of trajectories that represented single QDs, as opposed to small clusters of multiple QDs was calculated by the following formula:

$$f_1 = \frac{\int_{B_{\text{rel}}^0}^{B_{\text{rel}}^1+(B_{\text{rel}}^1-B_{\text{rel}}^0)} N(B_{\text{rel}}^{\max})\,\mathrm{d}B_{\text{rel}}^{\max}}{\int_0^\infty N\left(B_{\text{rel}}^{\max}\right)\,\mathrm{d}B_{\text{rel}}^{\max}} \tag{2.5}$$

B_{rel}^0 is the minimum brightness value of the $B_{\text{rel}}^{\max}$ distribution. This equation counts the number of trajectories that are single QDs by integrating the area under the curve of the single-QD peak and divides that number by the total number of trajectories in that cell. This method of counting the number of single-QD trajectories is based on the previous finding that single QDs have symmetrical distributions.[38] The mean of the single-QD peak was set at B_{rel}^1, and the half-width of the peak was calculated as the difference between B_{rel}^1 and B_{rel}^0. With the assumption that the single-QD peak was symmetrical the upper bound of the integration was set at B_{rel}^1 plus the half-width, resulting in the integral bounds used in the number of Equation 2.5.

This method of setting the upper-bound for the single-QD peak has the possibility of misidentifying non-single trajectories as single (false positives). To account for this, we calculated the frequency of incorrect single-QD counts based on the assumption that the single QD distribution is symmetrical. To determine how many of these trajectories were false positives, we calculated a maximum false positive fraction (FPR) for each brightness distribution, where FPR is defined as the number of trajectories misidentified as single divided by the total number of trajectories assigned as single. The number of misidentified trajectories was determined by assuming that the single-QD peak was symmetrical, which allowed us to estimate the expected number of single trajectories. This value could be subtracted from the total number of trajectories assigned as single to determine the number of trajectories misidentified as single. All cells with false positive ratios greater than 0.25 were excluded from downstream analysis, as this indicated that the single-QDs could not be accurately counted for that dataset (Figure 2.10).

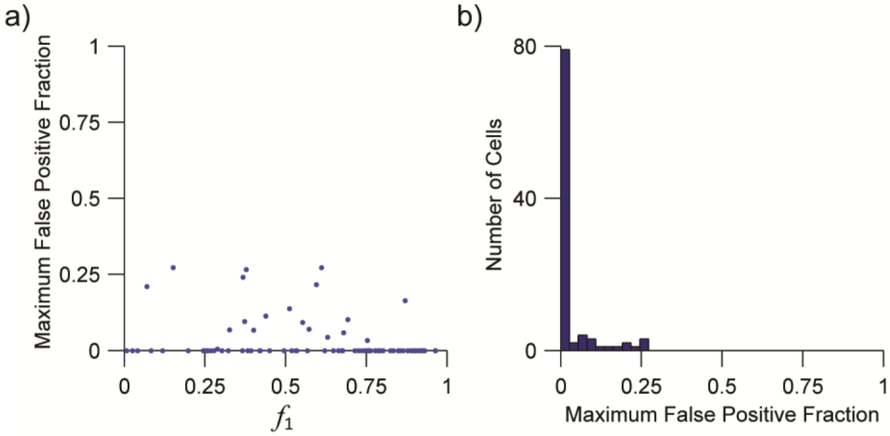

Figure 2.10. f_1 error analysis. (a) Scatter plot of f_1 and FPR values. (b) Histograms of FPR values. Number of data points are indicated by the area under the histogram.

Since both the D and α threshold used to calculate f_{mobile} and the counting method for calculating f_1 are independent, we were able to calculate a third metric: $f_{1,\text{mobile}}$, the fraction of trajectories that correspond to single-QDs that were "free" in the cytosol. $f_{1,\text{mobile}}$ is perhaps the most important metric as this is the desired state for many intracellular nanoparticles.

In addition to these fractions, we defined two metrics to quantify delivery efficiency and efficacy. The first parameter is N_{cell}, the total number of QDs delivered to the cell, can be calculated simply by summing n_{QD} for all trajectories:

$$N_{\text{cell}} = \sum_{0}^{\infty} n_{QD} = \frac{1}{B_{\text{rel}}^{1}} \sum_{0}^{\infty} N\,(B_{\text{rel}}^{\max}) \tag{2.6}$$

Similarly, N_{mobile} can be calculated by only including n_{QD} values from trajectories with D and α values above the previously determined thresholds.

2.3 Discussion

We describe a new analysis technique combining single-molecule diffusion and brightness analysis. This approach further yielded novel single-cell metrics that can be used to interrogate nanoparticle delivery mechanisms and intracellular particle state and final fate. Notably, the metrics N_{cell} and N_{mobile} are not absolute numbers, as the focal plane in which the QDs are imaged is thinner than the thickness of the cell. However, this limitation could be overcome by implementing imaging techniques that extend the z-range and are compatible with SPT, such as multifocal plane microscopy.[39,40]

With recent advances in instrumentation, probes, and image analysis software, the capacity to perform single-molecule tracking is now widely available.[17,41–43] With the new metrics we presented, it may be further possible to accurately apply pharmacodynamics models relating dose to efficacy and potency for nanoparticle therapeutics, which present unique challenges due to uncertainty of numerous transport parameters.[44] Additionally, even though this method currently limited to imaging cultured cells, it could also potentially be applied to evaluate delivery in living tissues in both intracellular and extracellular domains using imaging techniques with both rapid acquisition and high depth penetration, such as spinning disk confocal microscopy, light sheet microscopy, or holographic multiphoton imaging.[45,46]

Furthermore, since the parameters underlying the single-cell metrics (i.e. D, α, and n_{QD}) are defined for each trajectory there is a potential to define new single-cell metrics or to analyze subsets of trajectories with desired qualities. This could especially have a lot of potential if any new trajectory-level information can be extracted for further correlations, such as colocalization with another fluorescently label or structure. Such an application is presented in the fluorescence colocalization analysis presented in Chapter 4.

2.4 Methods

Transmission Electron Microscopy of Cells. Cells were cultured as monolayers on multi-well plates and fixed overnight at 4°C with 2.5% glutaraldehyde in 0.1 M cacodylate buffer (pH 7.4). Cells were then washed with the same buffer and post- fixed in 1% osmium tetroxide with 1.5% potassium ferrocyanide in the same buffer for one hour. The samples were subsequently rinsed with 2 or 3 exchanges of de-ionized water, dehydrated through an ethanol series ending with three exchanges of 100% absolute ethanol, and then embedded in Eponate 12 resin (Ted Pella, Inc.) by placing resin-infiltrated cells in a 60°C oven for 2 days. Upon resin polymerization, hardened resin blocks with monolayer cells on the bottom surface were removed from the culture plate, sawed into smaller pieces, and thin-sectioned parallel to the cell surface at 70 nm. Sections were then picked up with 200 mesh copper grids, stained with 5% aqueous uranyl acetate and 2% lead citrate, and viewed on a Hitachi H-7500 transmission electron microscope (Hitachi High Technologies America, Inc.) equipped with a BioScan CCD camera (Gatan, Inc.).

Cytotoxicity Studies. CHO cells were seeded in a 96-well plate (Greiner Bio-One) at a density of 20,000 cells per well, 24 hours prior to treatments. For the cytotoxicity study, 10 µL of Cell Counting Kit-8 (Dojindo Molecular Techniques, Inc.) was added to each well. After 3 hours, the absorbance of each well was measured at 450 nm using a Synergy HT microplate reader (BioTek Instruments, Inc.). For the viability study, 2 µM calcein AM (Santa Crux Biotechnology, Inc.) and 4 µM ethidium homodimer-1 (Setareh Biotech) were added to each well and incubated for 15 minutes at 37°C. Live/dead imaging was performed with a 20× 0.50 NA Plan-Neoufluar dry objective. Both calcein AM and ethidium homodimer-1 were excited using a 100 W halogen lamp, with excitation and emission light filtered by GFP and Cy3 filter sets (Zeiss), respectively. For the DAPI membrane-permeability measurement, CHO cells seeded at a density of 40,000 cells mL^{-1} in a LabTek chamber were loaded with 40 nM pPEG QDs with standard parameters of 10 minute hypertonic loading and 3 minute hypotonic lysis. The cells were then incubated with 1 µg/mL of DAPI (Sigma Aldrich), which allowed us to distinguish live cells from dead cells. Then we located cells with and without DAPI stain and acquired HILO images of the intracellular QDs and performed standard SPT and diffusion analysis.

Single Particle Tracking (SPT) and Diffusion Analysis. Single-molecule videos were analyzed by SPT using the MATLAB u-track software package developed by Jaqaman, *et al.*[30] to determine centroid pixel positions (x_o, y_o) for trajectories at each time point. Custom MATLAB scripts were used to calculate mean squared displacement (*MSD*) versus time increment (τ) curves for each particle trajectory and were fit to a model of anomalous diffusion in Equation 1.[31,32,47,48] For tracks longer than 100 frames, curves were fit for the first 10 time increments, whereas ¼ of the track length was fit for shorter tracks. Tracks shorter than 10 frames were discarded. These lengths were selected based on recommendations of Kepten and colleagues for tracks in the regime of strong subdiffusion to weak superdiffusion (α = 0.3-1.3) with low localization error.[37] We evaluated the impact of the localization error on D versus α heat maps and evaluated the impact of time increment span for curve fitting and found that both had fairly small impact on absolute mobile fractions. Curve fits were filtered based on the calculated error of the fitting parameters with error tolerances of 0.05 $\mu m^2/s$ for D and 0.15 for α.

$B_{\text{rel}}^{\text{max}}$ Calculation. $B_{\text{rel}}^{\text{max}}$ was calculated as the mode of the top 6% of the $B(t)$ distribution of its complete trajectory:

$$B_{\text{rel}}^{\text{max}} = Mo\ [B(0.94\ \leq P(B) \leq 1)], \tag{2.7}$$

where $P(B)$ is the probability distribution of brightness values from an intensity time trace, $B(t)$. Because QDs randomly fluctuate between on and off states (blinking), only the brightest state was considered in calculating $B_{\text{rel}}^{\text{max}}$, and we previously determined that the single-QD on-state brightness is homogeneous among for uniform QDs with this composition (Fig. 2.5).[38]

2.5 References

1. Chou, L. Y. T., Ming, K. & Chan, W. C. W. Strategies for the intracellular delivery of nanoparticles. *Chem. Soc. Rev.* **40,** 233–245 (2011).
2. Mitragotri, S., Burke, P. A. & Langer, R. Overcoming the challenges in administering biopharmaceuticals: formulation and delivery strategies. *Nat. Rev. Drug Discov.* **13,** 655 (2014).

3. Torchilin, V. P. Multifunctional, stimuli-sensitive nanoparticulate systems for drug delivery. *Nat. Rev. Drug Discov.* **13,** 813 (2014).
4. Zuris, J. A. *et al.* Cationic lipid-mediated delivery of proteins enables efficient protein-based genome editing in vitro and in vivo. *Nat. Biotechnol.* **33,** 73 (2015).
5. Time to deliver. *Nat. Biotechnol.* **32,** 961 (2014).
6. Martens, T. F., Remaut, K., Demeester, J., De Smedt, S. C. & Braeckmans, K. Intracellular delivery of nanomaterials: how to catch endosomal escape in the act. *Nano Today* **9,** 344–364 (2014).
7. Lukacs, G. L. *et al.* Cell Biology and Metabolism: Size-dependent DNA Mobility in Cytoplasm and Nucleus Size-dependent DNA Mobility in Cytoplasm and Nucleus. *J. Biol. Chem.* **275,** 1–6 (2000).
8. Luby-Phelps, K. & Taylor, D. L. Subcellular Compartmentalization by Local Differentiation of Cytoplasmic Structure. *Cell Motil. Cytoskeleton* **37,** 28–37 (1988).
9. Rehman, Z. ur, Hoekstra, D. & Zuhorn, I. S. Mechanism of polyplex-and lipoplex-mediated delivery of nucleic acids: real-time visualization of transient membrane destabilization without endosomal lysis. *ACS Nano* **7,** 3767–3777 (2013).
10. Richard, J. P. *et al.* Cell-penetrating peptides A reevaluation of the mechanism of cellular uptake. *J. Biol. Chem.* **278,** 585–590 (2003).
11. Schnell, U., Dijk, F., Sjollema, K. A. & Giepmans, B. N. G. Immunolabeling artifacts and the need for live-cell imaging. *Nat. Methods* **9,** 152–158 (2012).
12. Nienhaus, K. & Nienhaus, G. U. Fluorescent proteins for live-cell imaging with super-resolution. *Chem. Soc. Rev.* **43,** 1088–1106 (2014).
13. Stratmann, S. A. & van Oijen, A. M. DNA replication at the single-molecule level. *Chem. Soc. Rev.* **43,** 1201–1220 (2014).
14. Kanchanawong, P. *et al.* Nanoscale architecture of integrin-based cell adhesions. *Nature* **468,** 580–584 (2010).
15. Low-Nam, S. T. *et al.* ErbB1 dimerization is promoted by domain co-confinement and stabilized by ligand binding. *Nat. Struct. Mol. Biol.* **18,** 1244–1249 (2011).
16. Xia, T., Li, N. & Fang, X. Single-molecule fluorescence imaging in living cells. *Annu. Rev. Phys. Chem.* **64,** 459–480 (2013).
17. Kusumi, A., Tsunoyama, T. A., Hirosawa, K. M., Kasai, R. S. & Fujiwara, T. K. Tracking single molecules at work in living cells. *Nat. Chem. Biol.* **10,** 524–532 (2014).
18. Liu, Z., Lavis, L. D. & Betzig, E. Imaging live-cell dynamics and structure at the single-molecule level. *Mol. Cell* **58,** 644–659 (2015).
19. Pierobon, P. & Cappello, G. Quantum dots to tail single bio-molecules inside living cells. *Adv. Drug Deliv. Rev.* **64,** 167–178 (2012).
20. Michalet, X. *et al.* Quantum dots for live cells, in vivo imaging, and diagnostics. *Science* **307,** 538–544 (2005).
21. Smith, A. M., Duan, H., Mohs, A. M. & Nie, S. Bioconjugated quantum dots for in vivo molecular and cellular imaging. *Adv. Drug Deliv. Rev.* **60,** 1226–1240 (2008).
22. Pinaud, F., Clarke, S., Sittner, A. & Dahan, M. Probing cellular events, one quantum dot at a time. *Nat. Methods* **7,** 275–285 (2010).
23. Ma, L. *et al.* Multidentate Polymer Coatings for Compact and Homogeneous Quantum Dots with Efficient Bioconjugation. *J. Am. Chem. Soc.* **138,** 3382–3394 (2016).
24. Cai, E. *et al.* Stable small quantum dots for synaptic receptor tracking on live neurons. *Angew. Chemie* **126,** 12692–12696 (2014).

25. Wang, Y. *et al.* Small quantum dots conjugated to nanobodies as immunofluorescence probes for nanometric microscopy. *Bioconjug. Chem.* **25,** 2205–2211 (2014).
26. Okada, C. Y. & Rechsteiner, M. Introduction of macromolecules into cultured mammalian cells by osmotic lysis of pinocytic vesicles. *Cell* **29,** 33–41 (1982).
27. Yi, H., Leunissen, J. L. M., Shi, G.-M., Gutekunst, C.-A. & Hersch, S. M. A novel procedure for pre-embedding double immunogold--silver labeling at the ultrastructural level. *J. Histochem. Cytochem.* **49,** 279–283 (2001).
28. Tokunaga, M., Imamoto, N. & Sakata-Sogawa, K. Highly inclined thin illumination enables clear single-molecule imaging in cells. *Nat. Methods* **5,** 159–161 (2008).
29. Valentine, C. D., Verkman, A. S. & Haggie, P. M. Protein Trafficking Rates Assessed by Quantum Dot Quenching with Bromocresol Green. *Traffic* **13,** 25–29 (2012).
30. Jaqaman, K. *et al.* Robust single-particle tracking in live-cell time-lapse sequences. *Nat. Methods* **5,** 695–702 (2008).
31. Banks, D. S. & Fradin, C. Anomalous diffusion of proteins due to molecular crowding. *Biophys. J.* **89,** 2960–2971 (2005).
32. Weiss, M., Elsner, M., Kartberg, F. & Nilsson, T. Anomalous subdiffusion is a measure for cytoplasmic crowding in living cells. *Biophys. J.* **87,** 3518–3524 (2004).
33. Saxton, M. J. & Jacobson, K. Single-particle tracking: applications to membrane dynamics. *Annu. Rev. Biophys. Biomol. Struct.* **26,** 373–99 (1997).
34. Qian, H., Sheetz, M. P. & Elson, E. L. Single particle tracking. Analysis of diffusion and flow in two-dimensional systems. *Biophys. J.* **60,** 910–921 (1991).
35. Michalet, X. Mean square displacement analysis of single-particle trajectories with localization error: Brownian motion in an isotropic medium. *Phys. Rev. E* **82,** 41914 (2010).
36. Michalet, X. & Berglund, A. J. Optimal diffusion coefficient estimation in single-particle tracking. *Phys. Rev. E* **85,** 61916 (2012).
37. Kepten, E., Weron, A., Sikora, G., Burnecki, K. & Garini, Y. Guidelines for the fitting of anomalous diffusion mean square displacement graphs from single particle tracking experiments. *PLoS One* **10,** e0117722 (2015).
38. Lim, S. J. *et al.* Brightness-equalized quantum dots. *Nat. Commun.* **6,** 8210 (2015).
39. Ram, S., Prabhat, P., Chao, J., Sally Ward, E. & Ober, R. J. High accuracy 3D quantum dot tracking with multifocal plane microscopy for the study of fast intracellular dynamics in live cells. *Biophys. J.* **95,** 6025–6043 (2008).
40. Ram, S., Prabhat, P., Ward, E. S. & Ober, R. J. Improved single particle localization accuracy with dual objective multifocal plane microscopy. *Opt. Express* **17,** 6881 (2009).
41. Li, G.-W. & Xie, X. S. Central dogma at the single-molecule level in living cells. *Nature* **475,** 308 (2011).
42. Wu, B., Buxbaum, A. R., Katz, Z. B., Yoon, Y. J. & Singer, R. H. Quantifying protein-mRNA interactions in single live cells. *Cell* **162,** 211–220 (2015).
43. Manzo, C. & Garcia-Parajo, M. F. A review of progress in single particle tracking: from methods to biophysical insights. *Reports Prog. Phys.* **78,** 124601 (2015).
44. Li, M., Zou, P., Tyner, K. & Lee, S. Physiologically based pharmacokinetic (PBPK) modeling of pharmaceutical nanoparticles. *AAPS J.* **19,** 26–42 (2017).
45. Gonda, K., Watanabe, T. M., Ohuchi, N. & Higuchi, H. In vivo nano-imaging of membrane dynamics in metastatic tumor cells using quantum dots. *J. Biol. Chem.* **285,** 2750–2757 (2010).

46. Zhang, R. *et al.* Two-Photon 3D FIONA of Individual Quantum Dots in an Aqueous Environment. *Nano Lett.* **11,** 4074–4078 (2011).
47. Szymanski, J. & Weiss, M. Elucidating the origin of anomalous diffusion in crowded fluids. *Phys. Rev. Lett.* **103,** 38102 (2009).
48. Gal, N. & Weihs, D. Experimental evidence of strong anomalous diffusion in living cells. *Phys. Rev. E* **81,** 20903 (2010).

CHAPTER 3: OPTIMIZING QUANTUM DOT SURFACES FOR CYTOPLASMIC DELIVERY

3.1 Background

Macromolecule fate in the intracellular space is strongly influenced by the surface properties of the given material. Anionic nucleic acids are effectively immobile in cells for molecular weights > 100 kDa, whereas neutral colloids of equal mass are mobile.[1]

Surface properties also impact the efficacy of macromolecule delivery as well. OPL-mediated gene delivery of anionic nucleic acids[2] and their complexes with cationic polymers[3] has relatively low efficacy compared with the high delivery efficacy of proteins, which can be characterized as zwitterionic colloids. The strong impact of surface properties is likely to play a role in nanoparticle uptake and mobility as well.

To investigate the impact of different nanoparticle surface properties on intracellular delivery and fate, we prepared QDs with diverse surface properties. All QDs were based on (CdSe)CdZnS (core)shell nanocrystals with 5.7 nm diameter and 605 nm fluorescence emission (Figure 3.1).

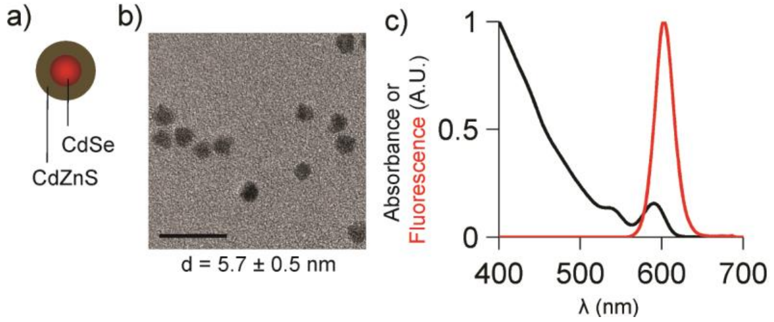

Figure 3.1 Characterization of quantum dot cores. (a) Schematic depiction of (core)shell (CdSe)CdZnS quantum dots (QDs). (b) Transmission electron micrograph of QDs; scale bar = 20 nm. (c) Absorbance and fluorescence spectra of QDs in hexane.

The QDs were coated with five different polymer structures that are detailed in Figure 3.2. The polymer coatings were based on monodentate thiol-terminated polyethylene glycol (mPEG), a series of polydentate ligands with tunable hydrophilic groups including carboxylic acids (pCOOH), polyethylene glycol (pPEG), and zwitterions (pZW), and amphiphilic polymers functionalized with carboxylic acids (aCOOH).

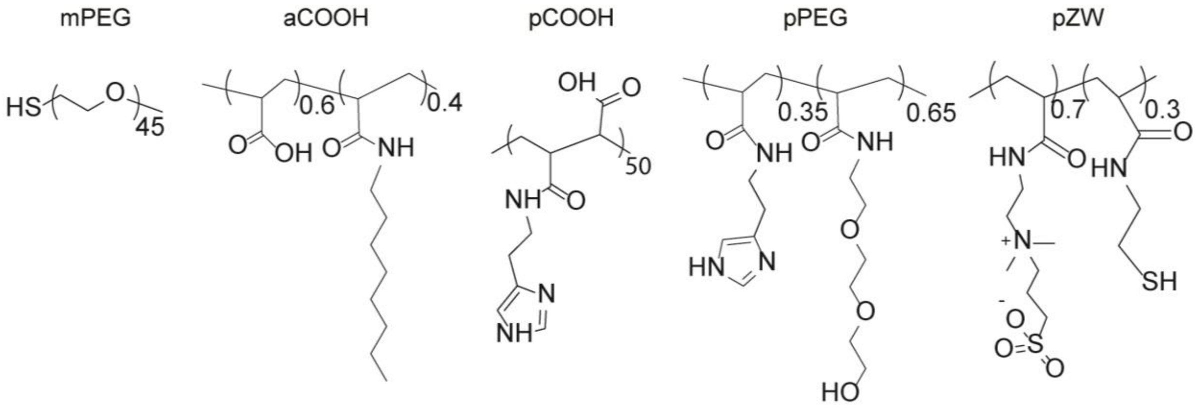

Figure 3.2. Chemical structures of polymeric QD coatings used in this work.

It is important to note that all final QDs had hydrodynamic diameters between 7-12 nm, as measured by dynamic light scattering (DLS). The surface charges of the different coatings were vastly different, with mPEG, pPEG, and pZW having nearly neutral surface charge and aCOOH and pCOOH had zeta potentials between -30 and -45 mV (Fig 3.3).

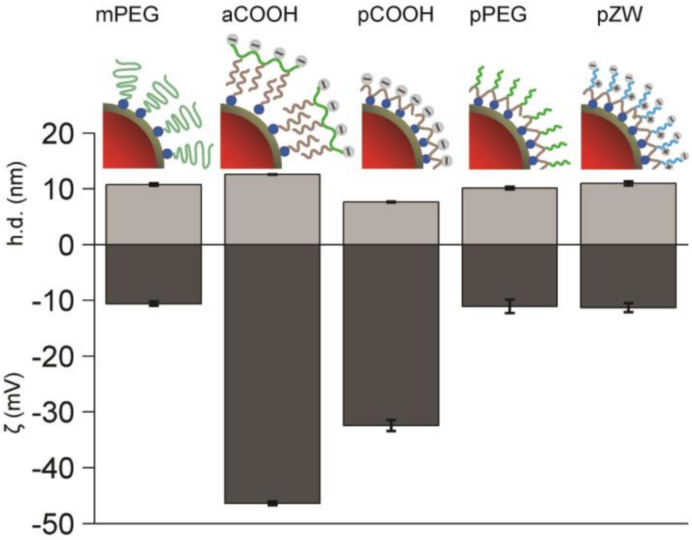

Figure 3.3 Schematic depictions of each QD coating (not to scale), showing differences in the number of binding groups (blue circles) per ligand. The coating naming convention indicates the binding mode (m = monodentate, a = amphiphilic, p = polydentate). Hydrodynamic diameter (h.d.) measured by dynamic light scattering (DLS) and zeta potential (ζ) were acquired in pH 7.4 buffer. n = 3 for all QD coatings, and all error bars indicate s.e.m.

All QDs were stable for months except for mPEG-QDs, as monodentate ligands slowly detach upon dilution in oxidizing conditions, although these QDs were stable in concentrated stock solutions for several days (Figure 3.4).[4,5]

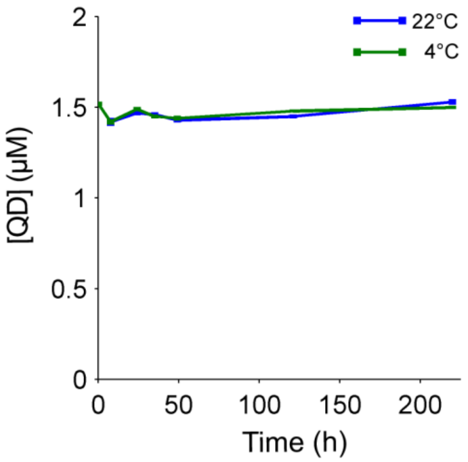

Figure 3.4. Stability of mPEG-QDs in 50 mM borate buffer. Stability was measured by centrifuging at 7000 x *g* for 10 minutes to remove aggregates that may have formed due to coating instability. Concentrations were determined by measuring absorbance values at 350 nm. n = 3 for both temperature conditions. Error bars indicate s.e.m.

3.2 Data and Analysis

3.2.1 QD Surface Comparison Results

HILO fluorescence movies of intracellular QDs were acquired for at least seven cells for each coating type approximately 1 hour after delivery by OPL to Chinese hamster ovarian cancer (CHO-K1) cells. SPT analysis was performed on all of the movies and the tracks were analyzed in terms of single-molecule diffusion and brightness, as described in the previous chapter. The diffusion analysis results are summarized in Fig 3.5a. Based on the empirical thresholds described previously ($D > 0.020$ μm^2 s^{-1}, $\alpha > 0.21$), the mPEG QDs, which had unstable coatings with neutral surface charge, and the aCOOH and pCOOH QDs, both of which had stable coatings with highly negative surface charge, showed majority immobile trajectories. On the other hand, the pPEG and pZW coated QDs, both of which had stable and electrostatically neutral surfaces, show 60-82% mobile trajectories. These trends show that both stable and neutral surface coatings are necessary for intracellular mobility.

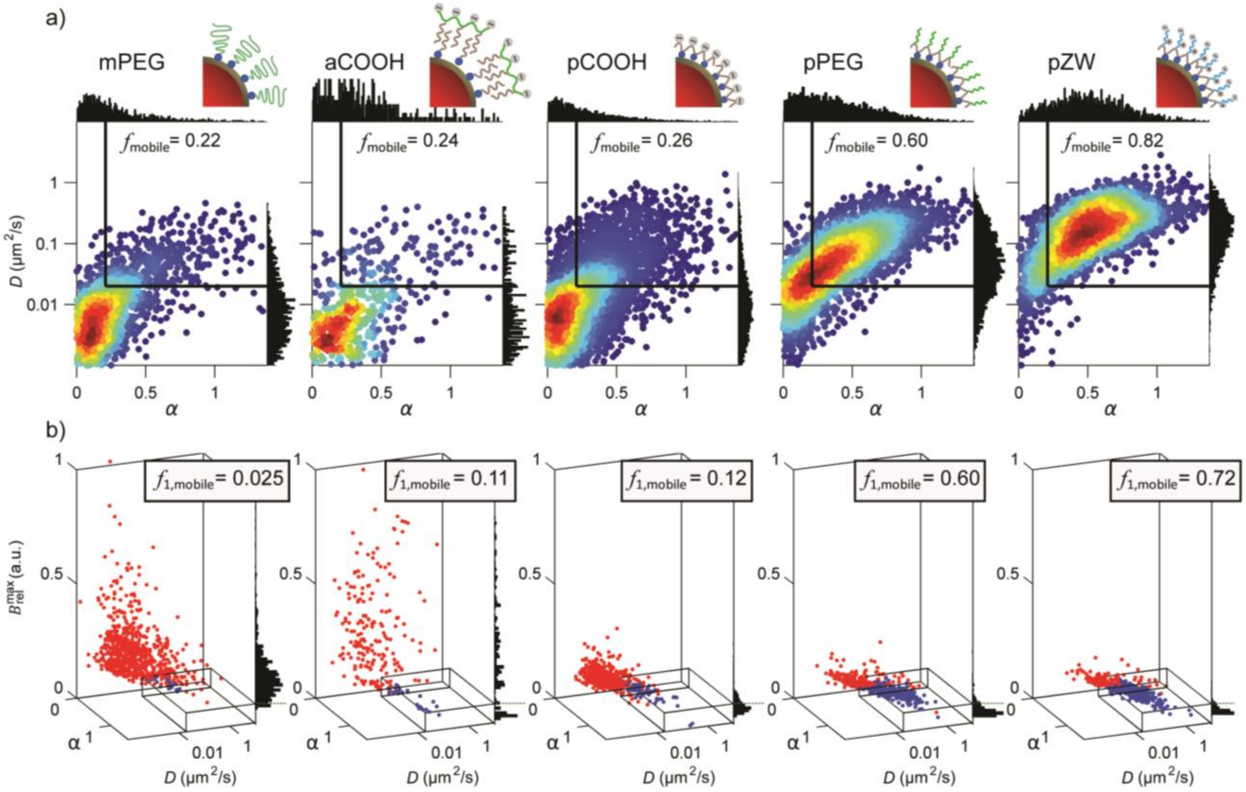

Figure 3.5. Coating-dependent behavior of intracellular quantum dots. (a) Heat maps of diffusion coefficient, *D*, versus confinement parameter, *α*. Histograms of *D* and *α* are projected on the *x* and *y* axes, respectively, and thresholds imposed for mobility are shown as black lines, yielding f_{mobile} shown in each plot. n = 7, 7, 16, 11, and 18 CHO cells for mPEG, aCOOH, pCOOH, pPEG, and pZW, respectively. (b) Representative 3D plots of *D* versus *α* versus $\boldsymbol{B}_{\mathbf{rel}}^{\mathbf{max}}$ for the different quantum dot (QD) coatings in individual cells. The box indicates the same threshold from (a), in addition to a $\boldsymbol{B}_{\mathbf{rel}}^{\mathbf{max}}$ threshold for delineating populations of single QDs to determine $f_{1,\text{mobile}}$, which is in the inset of each plot.

Figure 3.5b shows 3D scatter plots of $B_{\text{rel}}^{\text{max}}$ for each particle type together with both mobility parameters. Each QD coating class exhibited a distinct level of clustering, indicated by the distributions of points along the z-axis. The rectangular box in the bottom right of each plot indicates the region designating those that are both mobile and single ($f_{1,\text{mobile}}$), with trajectories color-coded to indicate whether they fall in the brightness population of single QDs (blue) or clusters (red). The mPEG and aCOOH QDs demonstrated substantial clustering inside cells, indicated by numerous red spots at high $B_{\text{rel}}^{\text{max}}$ values. However, pPEG, pZW, and the mostly immobile pCOOH QDs all had f_1 fractions greater than 45%. These are single-cell data; Figure 3.6 shows representative cell-to-cell variability. Notably, although the pCOOH QDs are almost entirely immobile, they also have a high single-QD fraction, showing that stable multidentate coatings are necessary for delivery of single QDs and for avoiding clustering.

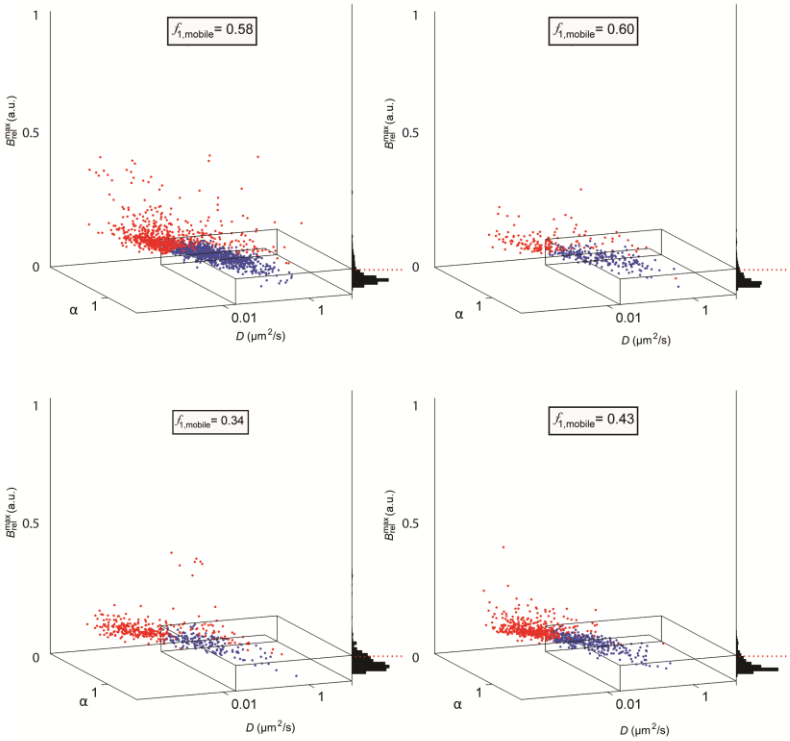

Figure 3.6. 3D plots of D versus α versus B_{rel}^{max} for pPEG QDs. Heterogeneity of brightness distributions and QD clustering is apparent between different cells.

3.2.2 Validation of QD Diffusion Results

In order to validate and understand the parameters derived from the single-trajectory analysis the results were compared to traditional analytical, experimental, and computational methods. This included: ensemble level MSD analysis, fluorescence correlation spectroscopy (FCS) measurements, and analysis of simulated single-particle trajectories.

Ensemble MSD Analysis. Ensemble MSD curves were calculated by averaging over all trajectories within each coating class. These results are plotted in Figure 3.7, showing the clear distinguishable differences between the different materials at the ensemble level. The mean *D* values spanned between 0.02 to 0.2 μm^2 s^{-1} and were similar when calculated from individual trajectories or as an ensemble, however the average α was substantially smaller when calculated per trajectory (0.26 – 0.49) compared with pooled data (0.44 – 0.70) (Table 3.1). The values calculated from individual tracks are presumably more accurate, as each trajectory was fit using a measured localization error for each track, which could be highly variable between tracks.

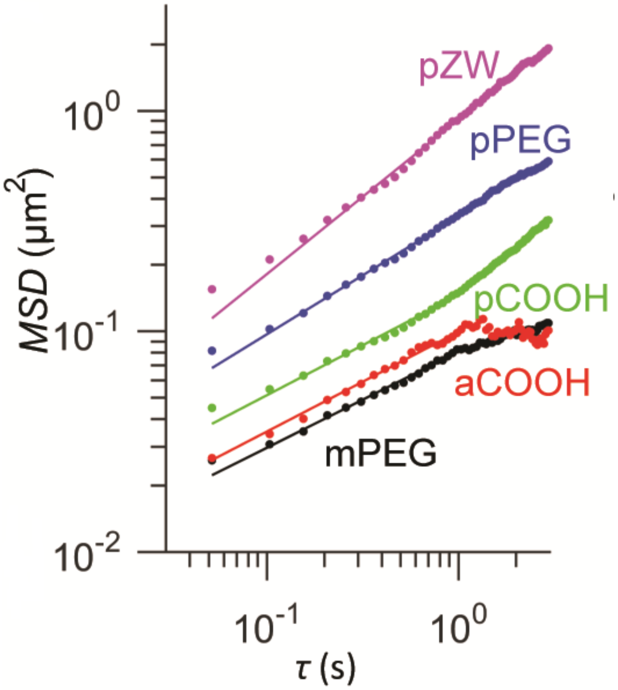

Figure 3.7. Ensemble average *MSD* plot for all recorded trajectories fit to Equation 1 for the first 20 time increments. Average *D* and α values from ensemble and single-trajectory analyses are summarized in Table 3.1.

Table 3.1. Average diffusion coefficients and confinement parameters for data in Fig. 3.5 and 3.7

	Single-Trajectory Analysis		Ensemble Analysis	
	$\bar{D}$ (μm^{2}s^{-1})	$\bar{\alpha}$	$\bar{D}$ (μm^{2}s^{-1})	$\bar{\alpha}$
mPEG	0.023	0.26	0.020	0.44
aCOOH	0.030	0.34	0.025	0.46
pCOOH	0.037	0.24	0.036	0.46
pPEG	0.090	0.37	0.083	0.54
pZW	0.22	0.49	0.23	0.70

Fluorescence Correlation Spectroscopy. FCS is a well-established technique that is used to characterize the diffusion of small fluorescent molecules. Recently, FCS has been explored to measure the diffusion of QDs.[6,7] However, there are many challenges with this due to the fact that FCS is an ensemble technique that need many extrinsically determined parameters to fit *D* accurately, and this is further complicated by the fluorescence intermittency and dark fraction of QDs, both of which are on similar time scales of the diffusion of QDs in aqueous solution.[6,8]

HeLa cells were loaded with pPEG-QDs, and the QD behavior was characterized by both HILO imaging followed by SPT analysis and FCS measurements. These results are summarized in Figure 3.8 and Table 3.2.

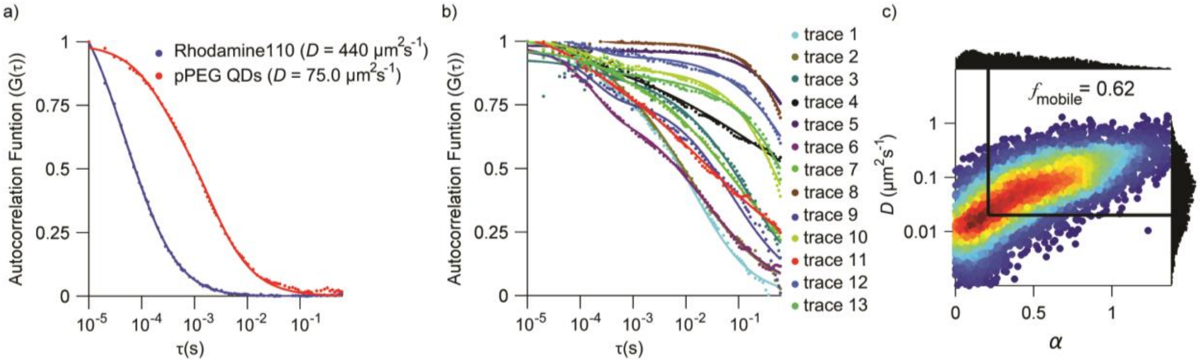

Figure 3.8. Fluorescence correlation spectroscopy (FCS) data. (a) FCS autocorrelation curves for Rhodamine 110 and pPEG-QDs in aqueous buffer fit to a Brownian diffusion model. (b) FCS autocorrelation curves for pPEG-QDs delivered by OPL to HeLa cells, fit to the multi-component anomalous diffusion model shown in Equation 3.3. n = 13 samples. Fit parameters for the components of each trace are shown in Supplementary Table 2. (c) Heat map of D versus α for pPEG-coated QDs delivered to HeLa cells, calculated by SPT data. n = 9 cells.

Table 3.2. FCS fit parameters for pPEG-QDs delivered to HeLa cells. Parameters correspond to those defined in Equation 3.3.

	$\tau_{D,1}$(s)	D_1 (μm^2/s)	α_1	A_1	$\tau_{D,2}$(s)	D_2 (μm^2/s)	α_2	A_2	R^2
trace 1	0.0073	4.50	0.83	0.65	0.037	0.90	0.92	0.35	0.9957
trace 2	0.009	3.50	0.57	1.0	--	--	--	--	0.9979
trace 3	0.054	0.61	0.52	0.41	0.16	0.20	0.80	0.59	0.9818
trace 4	0.69	0.045	0.24	1.0	--	--	--	--	0.9900
trace 5	2.98	0.011	0.85	1.0	--	--	--	--	0.9893
trace 6	0.021	1.54	0.60	1.0	--	--	--	--	0.9984
trace 7	0.071	0.46	0.49	1.0	--	--	--	--	0.9980
trace 8	1.70	0.019	0.94	1.0	--	--	--	--	0.9936
trace 9	0.073	0.45	0.71	1.0	--	--	--	--	0.9798
trace 10	0.52	0.063	0.98	0.74	0.92	0.036	0.41	0.26	0.9901
trace 11	0.029	1.15	0.34	1.0	--	--	--	--	0.9976
trace 12	1.72	0.020	0.66	1.0	--	--	--	--	0.9825
trace 13	0.82	0.040	1.0	0.59	0.84	0.039	0.36	0.41	0.9681

The average D measured with SPT was 0.10 μm^2 s^{-1} and $\alpha = 0.45$, while the ensemble average for FCS was 0.84 μm^2 s^{-1} and $\alpha = 0.66$. FCS also showed a wide range of D values in different cell regions as well as multimodal behavior in single locations. However highly immobile populations were not clearly resolved with the technique, which is likely the source of the small discrepancy between average D values, together with differences in time lag at which each is defined (1 second for SPT and τ_D for FCS).

Analysis of Simulated Trajectories. Previous analytical, computational, and experimental work has shown that measuring diffusion coefficients by MSD analysis of single-particle trajectories has statistical limitations to its accuracy, and a natural spread in the fitted diffusion coefficients that arises from this analysis method.[9–12] This can be overcome by maximizing the track length.[9–12] However, the reality of experimental acquisition conditions does not allow this parameter to be controlled, as particles may randomly move out of the focal plane or "blink" off long enough to prevent accurate reconnection of long tracks.

In this regard, we simulated a number of trajectories with different inputs for D, α, σ_{xy}, and track lengths. These simulated trajectories were analyzed by the same single-particle diffusion analysis used for the experimentally acquired trajectories to characterize the spread of fitting parameters of the MSD analysis. Analyzing simulated tracks allowed us to isolate the impact of specific parameters. For instance, varying the track length from 10-500 frames while holding all other factors constant showed that the distinctive spread and 45 degree "tilt" in the D versus α heat maps arose from the predominance of short tracks (Figure 3.9).

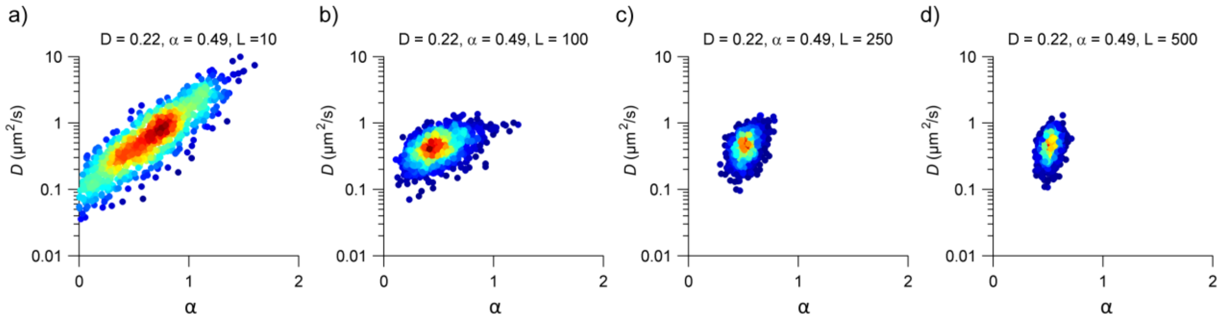

Figure 3.9. Simulation analysis of track length impact. Heat map of *D* versus *α* for 1000 trajectories with D = 0.22 μm^2 s^{-1} and α = 0.49 (average values for pZW-QDs) with fixed track lengths of (a) 10, (b) 100, (c) 250, and (d) 500 frames. Simulated localization error values were derived from experimentally measured average values from pZW-QDs.

Additionally, we used the power of analyzing simulated trajectories to understand what real D and α values were underlying the fitted *D* and *α* values for the experimental results. As track length is a critical factor influencing the parameter distributions (Fig 3.10) were imposed as constraints in all of the simulations evaluating *D*-*α* pairs.

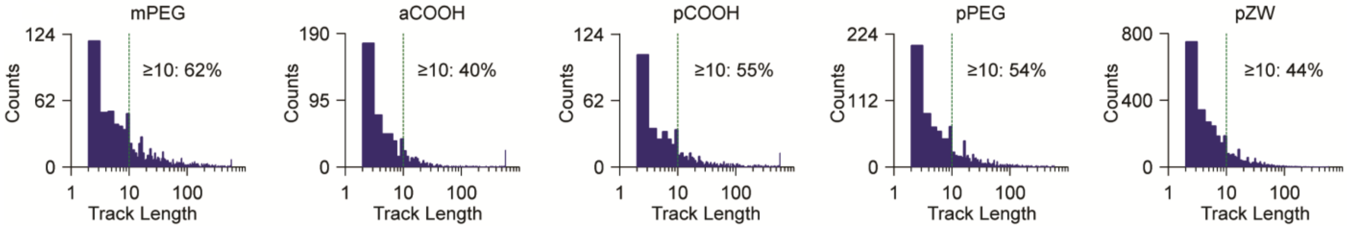

Figure 3.10. Track length histograms of QDs in cells. Track length distributions for QDs with the 5 different coatings in CHO cells. Note that the pZW-QD and pPEG-QD samples have higher measured *D* compared with QDs diffusing in 98% glycerol because they demonstrate a larger percentage of tracks longer than 10 frames, due to z-axis confinement. Data correspond to the same as that of Figure 3.5a-b.

Similarly, experimentally measured localization error values were imposed for each QD coating type. Using these experimentally measured constraints, we simulated appropriate ranges of D and α for mPEG and pZW QDs in order to see the impact of different D and α inputs on the output parameter distributions (Figs 3.11-12).

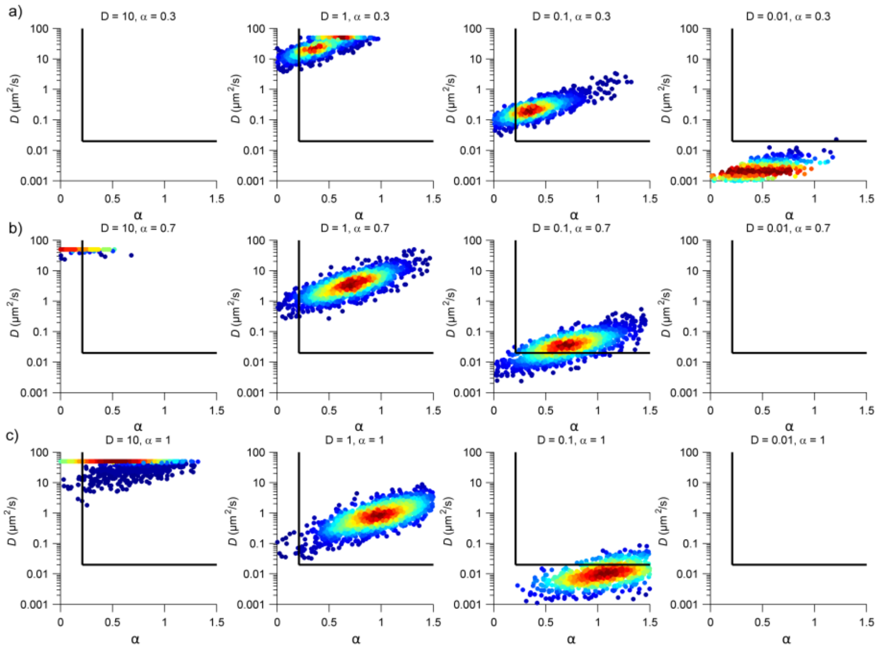

Figure 3.11. Simulation analysis of the impact of *D* and *α*. Track length distributions were derived from empirical results from pZW QDs (see Supplementary Figure 18) with 1610 trajectories. Heat maps show *D* versus *α* with *D* ranging from 0.01 to 10 μm^2 s^{-1} in each column and *α* = (a) 0.3, (b) 0.7, and (c) 1. Simulated localization error values were derived from experimentally measured values from pZW QDs.

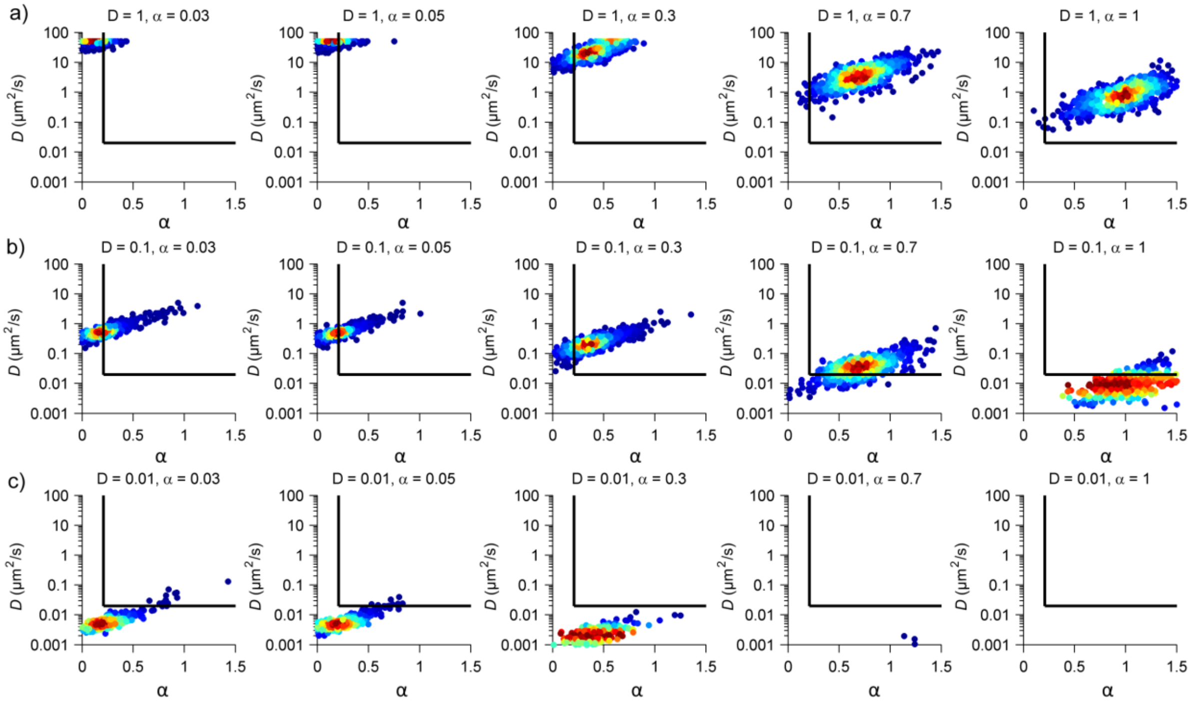

Figure 3.12. Simulation analysis of the impact of *D* and *α*. Track length distributions were derived from empirical results from mPEG QDs (see Supplementary Figure 13) with 1610 trajectories. Heat maps show *D* versus *α* with *α* ranging from 0.03 to 1 in each column and *D* of (a) 1, (b) 0.1, and (c) 0.01 μm^2 s^{-1}. Simulated localization error values were derived from experimentally measured values from mPEG QDs.

When comparing the experimental data to the simulation results, it is clear that the distributions observed in cells were too polydisperse to reflect a single population and must have derived from a range of mobility parameters. An analysis of the error associated with *D* vs *α* values derived from simulated data showed that both values were fairly accurate except when *D* was small such that the mobility was in the same range as the localization error (Fig 3.13).

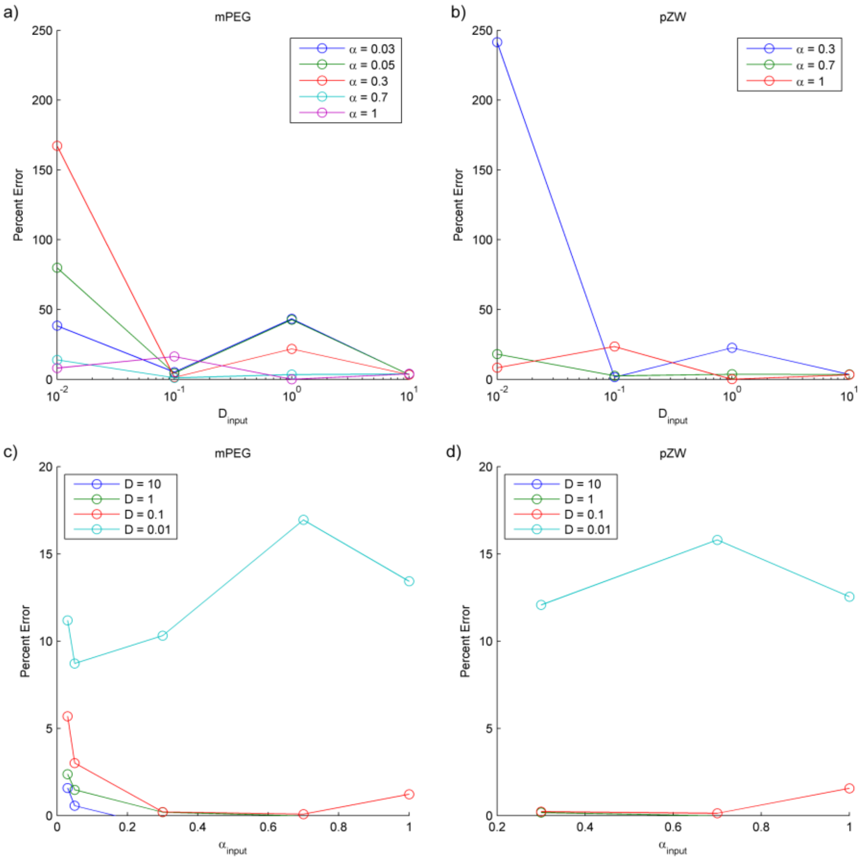

Figure 3.13. Error in D and α measured from simulation results. (a,b) Plots show percent difference between the calculated average D and input D for track length distributions and localization error values derived from empirical data from (a) mPEG-QDs and (b) pZW-QDs. (c,d) Plots show percent difference between the calculated average α value and input α values for track length distributions and localization error values derived from empirical data from (c) mPEG-QDs and (d) pZW-QDs.

Since it doesn't appear that the experimental results could have arisen from homogenous populations with single D and α values, we summed up the results of multiple sets of simulated trajectories to show a possible range of D and α values that may have been underlying the mPEG and pZW experimental results (Fig 3.14).

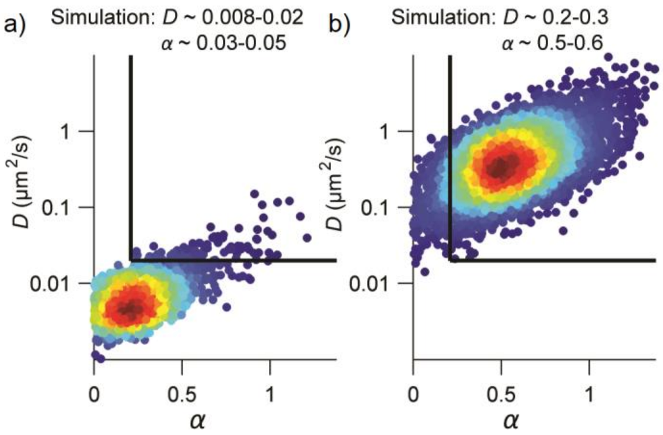

Figure 3.14. Sums of simulated trajectories approximating experimental results (a) Heat map of *D* versus *α* for simulated trajectories generated using *D* and *α* inputs across the indicated ranges to approximate the mPEG-QD distribution. (b) Heat map of *D* versus *α* for simulated trajectories generated using *D* and *α* inputs across the indicated ranges to approximate the pZW distribution.

3.2.3 Single-Cell Metrics: QD Surface Comparison

As previously noted, pPEG and pZW had the highest fractions of QDs that had cytoplasmic freedom and low levels of aggregation, while the mPEG, pCOOH, and aCOOH coatings yielded clustered or immobile QDs. These results are summarized in Figure 3.15. The mechanisms underlying these trends could be further understood by looking at trends in the other single-cell metrics defined in the previous chapter.

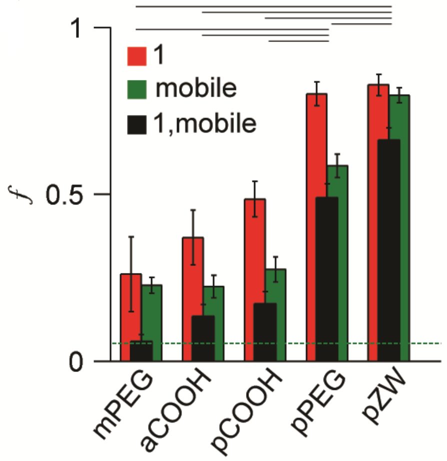

Figure 3.15. Data for each QD coating show f_{1}, f_{mobile}, and $f_{1,mobile}$. The green dashed line indicates the lower limit for f_{mobile} (0.053) corresponding to the localization error. Horizontal black lines indicate $p < 0.05$, calculated using Student's t-test, for $f_{1,mobile}$ comparisons. n = 7, 7, 16, 11, and 18 cells for mPEG, aCOOH, pCOOH, pPEG, and pZW, respectively.

Trends in the total number of QDs delivered per cell, N_{cell}, and the final number of mobile QDs per cell, N_{mobile}, reveal differences in the uptake mechanisms for the different QD coatings. (Fig 3.16a) If the mechanism underlying OPL delivery is simply fluid-phase transport, then N_{cell} should theoretically be 100-150 for all QDs, independent of coating, based on an estimated influx volume of ~10 fL in the hypertonic loading step.[2] N_{cell} for pZW-QDs (159 ± 20) was indeed close to this expected value, suggesting that pure fluid transport was responsible for uptake for this coating. However, the higher N_{cell} values for all other QDs, reaching 1,963 ± 270 for mPEG-QDs, indicates a parallel secondary uptake process, likely via membrane adsorption. Additionally, Figure 3.16b shows the surprising result that despite uptake varying by more than 12-fold, N_{mobile} was statistically indistinguishable for QDs coated with mPEG, pCOOH, pPEG, and pZW, with N_{mobile} spanning 72-172, which overlaps with the range expected for pure fluid-phase transport. Note that N_{mobile} for aCOOH-QDs was significantly smaller compared with all of the neutral QDs ($p < 0.05$), likely due to strong anionic charge that can electrostatically repel the plasma membrane during loading.

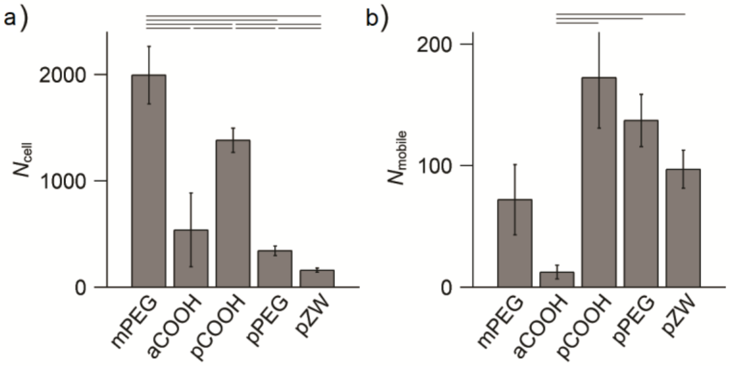

Figure 3.16. Uptake efficiency and mobility. (a) Number of internalized QDs per cell for 40 nM loading concentrations. For mPEG and pCOOH, data are linear extrapolations from 10 nM concentrations due to high spot intensity due to clustering. (b) Mobile QDs per cell. n = 7, 7, 16, 11, and 18 cells for mPEG, aCOOH, pCOOH, pPEG, and pZW, respectively.

In order to investigate this possible secondary uptake mechanism, we repeated the delivery of mPEG-QDs in the presence of adsorption-blocking agents (casein) and observed a vastly different diffusive pattern and significant shifts in the uptake efficiency (Fig 3.17a). N_{cell} decreased to 23% of its value without blocking agents ($p = 0.036$) and f_{mobile} increased by 77% ($p = 0.018$, calculated using Student's *t*-test,) (Fig. 3.17b). On the other hand, for mPEG-QDs, N_{mobile} did not change significantly with the addition of blocking agents during delivery ($p = 0.60$; Figure 3.17c, calculated using Student's *t*-test,) despite a drastic reduction in N_{cell}, presumably because osmotic transport that yields mobile cytoplasmic QDs is not mediated by adsorption.

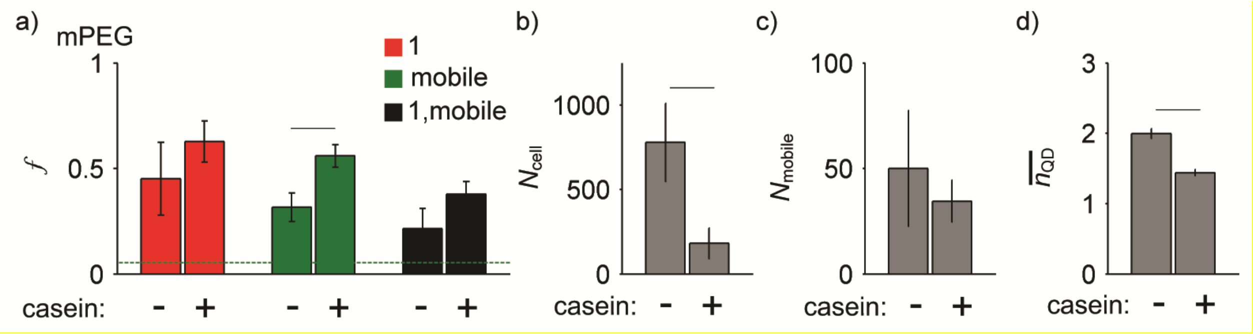

Figure 3.17. Mobility, delivery, and clustering metrics for QDs. QDs coated with mPEG were loaded into CHO cells, with and without casein added to block nonspecific binding. (a) Aggregated data are plotted to show $f_{1,}$ f_{mobile}, and $f_{1,mobile}$ for mPEG-QDs with and without casein blocking. The green dashed line in indicates the lower limit for f_{mobile} (0.040) which corresponds to the localization error. (b) Number of internalized QDs per cell for mPEG-QDs with and without blocking for 10 nM loading concentration. The sharp decrease in N_{cell} for the mPEG QDs with the addition of casein to block nonspecific adsorption demonstrates that nonspecific interaction with the cell surface is likely to be the underlying mechanism for the high level of intracellular delivery for mPEG-coated QDs. (c) Total number of mobile mPEG-QDs per cell for each condition, showing that blocking does not significantly alter the number of mobile QDs per cell. (d) Effect of casein blocking on mPEG-QD clustering. The decrease in $\overline{\boldsymbol{n}_{\mathbf{QD}}}$ for mPEG with casein similarly demonstrates that nonspecific adsorption is associated higher levels of QD clustering. Horizontal black lines indicate $p < 0.05$. For all experimental conditions, n = 6 cells per group. All error bars indicate s.e.m.

The second key step for any intracellular delivery process that utilizes endosomal pathways is typically some sort of endosomal escape or release mechanism. In our QD-surface comparison, we observed that f_{mobile} negatively correlated with N_{cell}, as shown in Figure 3.18. This indicates that that endosomal release is inefficient in cells with large N_{cell}. This negative correlation is indicative of the challenge in designing materials to balance both increased uptake efficiency and effective endosomal escape.

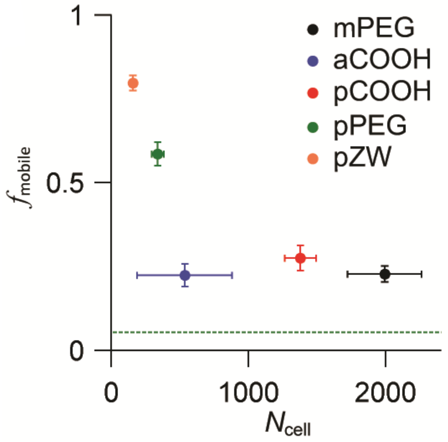

Figure 3.18. Negative correlation between f_{mobile} and N_{cell} for coatings demonstrates that materials with high mobile fractions deliver less efficiently. n = 7, 7, 16, 11, and 18 cells for mPEG, aCOOH, pCOOH, pPEG, and pZW, respectively.

To gain further insight into how internalization differs between the coatings, we separately analyzed single QDs and clusters to determine how clustering impacts mobility. Figure 3.19 shows a negative correlation of average cluster sizes, $\overline{n_{QD}}$, with f_{mobile} showing that clustering is associated with lower mobility.

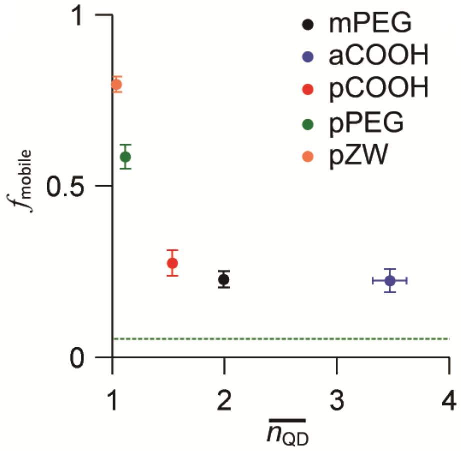

Figure 3.19. Negative correlation between f_{mobile} and $\overline{n_{QD}}$, for coatings demonstrates that QDs are clustered in cells in which they are immobile. n = 7, 7, 16, 11, and 18 cells for mPEG, aCOOH, pCOOH, pPEG, and pZW, respectively.

This negative correlation could either be due to clusters having inherently lower mobility due to their increased size or because whatever process immobilized the QDs also facilitated the clustering of the nanoparticles. Figure 3.20 shows plots of $f_{1,\mathrm{mobile}} / f_1$ and $f_{>1,\mathrm{mobile}} / f_{>1}$. For coatings for which $f_{1,\mathrm{mobile}} / f_1 > f_{>1,\mathrm{mobile}} / f_{>1}$, we can infer that clustering restricts mobility, either because clusters are too large to exit endosomes, or because the endosomes cannot rupture. This was indeed the case that clustering restricted mobility for pCOOH, aCOOH, and pPEG QDs ($p <$ 0.07, calculated using Student's *t*-test,), all of which loaded well beyond the limits of osmotic transport, likely due to adsorption to membrane components. However for both pZW and mPEG, $f_{1,\mathrm{mobile}} / f_1$ and $f_{>1,\mathrm{mobile}} / f_{>1}$ were statistically indistinguishable ($p > 0.5$). This similarity is logical for pZW-QDs, which were nearly entirely mobile, but this is suggests a unique uptake pathway for mPEG QDs that prevented release even when internalized individually in single endosomes. These QDs were unstable at low concentrations, so adsorption to endosomes likely prevented endosomal escape.

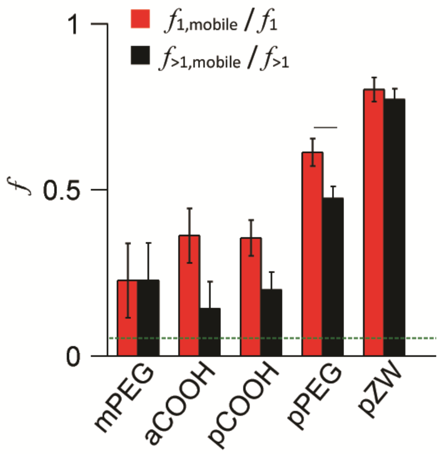

Figure 3.20. Comparison of $f_{1,\mathrm{mobile}} / f_1$ and $f_{>1,\mathrm{mobile}} / f_{>1}$ reflect mobility for single QDs and clusters, respectively. Horizontal lines indicate $p < 0.05$ within coating types only. n = 7, 7, 16, 11, and 18 cells for mPEG, aCOOH, pCOOH, pPEG, and pZW, respectively.

3.2.4 Single-Cell Metrics: Cell Type Comparison

We analyzed the impact of cell type using CHO cells, HeLa human cervical cancer cells, and A431 human epidermoid cancer cells, the latter of which were analyzed separately for single cells and cells that grew in clumps with cell-cell junctions that reduce the accessible membrane surface area. This comparison was done using pPEG-QDs, which showed a mix of both cytoplasmic and immobile states in our initial comparison of QD surface coatings in CHO cells. As shown in Figure 3.21a, cell type had less impact on f_1, f_{mobile}, and $f_{1,\text{mobile}}$ compared with the impact of QD coating, which is consistent with previous ensemble studies of OPL.[2] However, f_1 was significantly larger for CHO cells, which may reflect distinct pinocytotic mechanisms due to their small size and surface area.[13] On the other hand, HeLa cells exhibited significantly lower f_1, higher N_{cell}, and higher N_{mobile} (Fig. 3.21b-c). The higher N_{cell} and N_{mobile} values may be explained by the larger average surface area of the HeLa cells, which is likely associated with higher adsorption-dependent uptake (Fig. 3.21d). Cell type also had a significant impact on clustering that also correlated with membrane surface area (Fig. 3.21e). Only the smallest CHO cells exhibited enhanced endosomal escape for single QDs compared to clusters ($f_{1,\text{mobile}} / f_1 > f_{>1,\text{mobile}} / f_{>1}$), shown in Figure 3.21f.

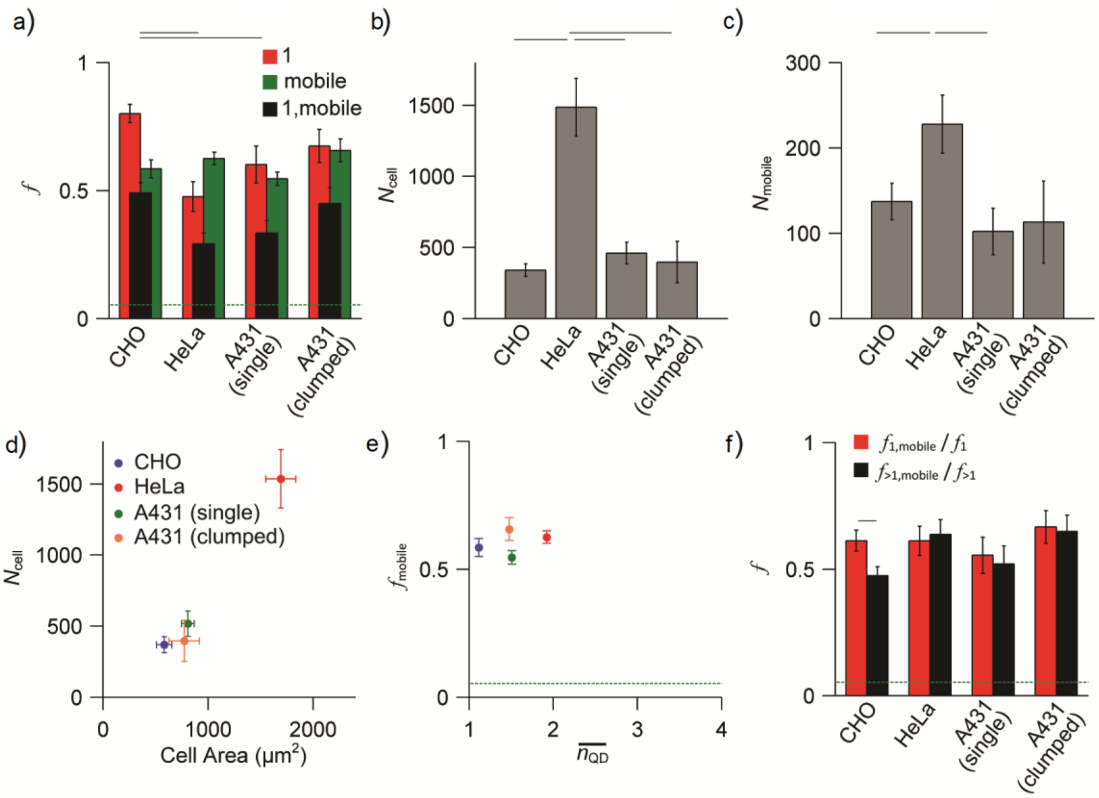

Figure 3.21. Impact of cell type on OPL delivery. (a) Data for three cell types (A431, CHO-K1, and HeLa), showing f_1, f_{mobile}, and $f_{1,\mathrm{mobile}}$. For A431 cells, single and clumped cells were analyzed separately. Horizontal lines indicate $p < 0.05$ for $f_{1,\mathrm{mobile}}$. (b) Number of internalized QDs per cell. (c) Mobile QDs per cell. (d) N_{cell} correlates with the average cell area. (e) Little correlation is observed between f_{mobile} and $\overline{\boldsymbol{n}_{\mathbf{QD}}}$, but different cell types have distinct clustering. Cell types are indicated by color codes in panel (d). (f) Comparison of $f_{1,\mathrm{mobile}} / f_1$ and $f_{>1,\mathrm{mobile}} / f_{>1}$ reflect mobility for single QDs and clusters, respectively. Horizontal lines indicate $p < 0.05$ within cell types only. All cell type comparisons used pPEG-QDs, with n = 10, 9, 7, and 9 cells for CHO, HeLa, single A431, and clumped A431 cells, respectively. All error bars are s.e.m.

3.3 Discussion

The new single-cell metrics presented here, allow for investigations of delivery mechanisms and intracellular particle state in ways that have not been accessible before. N_{cell} and f_{mobile}, reflect the efficiency of transport into the cell and the efficiency of endosomal release, respectively, the two critical steps in cytoplasmic delivery. The derived metrics n_{QD}, f_1, and $f_{1,\mathrm{mobile}}$, yield important insights into the state of the internalized materials and the endosomal release mechanism. These outcomes require the unique photophysical properties of QDs, with bright and stable emission that is homogeneous across a population of nanoparticles.[4] Specifically, these properties allow correspondence of brightness to absolute particle number as well as long-term tracking, which are not possible with organic dyes.[14]

The major finding from our analyses is that pZW-QDs are uniquely suited to cytoplasmic delivery through OPL. The pPEG-QDs had similar physical properties but smaller f_{mobile}, likely due to nonspecific binding evident from higher N_{cell}. The differences in mobility between the pZW and pPEG QDs and the increased efficiency of endosomal escape for the pZW-QDs may be due to different levels of hydration and different interactions with intracellular proteins. Molecular simulations comparing zwitterionic and nonionic PEG based materials have shown that zwitterionic materials exhibit stronger hydration than nonionic PEG materials and that PEG materials interfere with the hydrophobic domains of proteins while zwitterionic materials have limited interaction with these domains.[15] However, f_{mobile} for pPEG-QDs increased substantially when delivered through liposomal vesicles, reaching 78%, which further shows that adsorption processes occurring during delivery can have a dominating impact on final intracellular state. The other major finding from the surface comparisons was that unstable or highly charged surface coatings result in immobilized intracellular nanoparticles. When PEG was only weakly attached (mPEG-QDs), N_{cell} drastically increased for OPL delivery, while endosomal escape was drastically reduced. Proteins that exhibit membrane adsorption were found to exhibit similar outcomes.[16] Uptake was further enhanced when the magnitude of electrostatic charge was greater (aCOOH-QDs, pCOOH-QDs) likely due to binding to cationic protein domains, but endosomal release was further diminished, likely due to rapid acidification of the vesicles and neutralization of the ionically stabilized colloids.[17,18] These outcomes suggest that for intracellular targeting with molecular probes, stable and neutral surfaces are ideal.

Based on these results, it is evident that total cell uptake measurements are not suited for optimizing cytoplasmic delivery because the absolute number of delivered cargo N_{cell} was highly disproportional to N_{mobile}, as QDs with smallest N_{cell} values (pPEG-QDs, pZW-QDs) had similar N_{mobile} values to those with the largest N_{cell} values (mPEG-QDs). Importantly, these live-cell analyses were much more quantitative compared with analysis of TEM images, which were exceptionally challenging to quantify and exhibited significant fixation artifacts. In particular, QDs were often observed near the cell periphery (Figure 2.2), which was not reflected in living cells.

The spread of measured values strongly depends on track length (Figure 3.9). The accuracy of measured D and α values can be improved by using a faster video frame rate or methods that extend the z-range to increase track lengths, and by using brighter QDs to increase the photon flux to reduce localization error. However brighter emitters would necessitate the use of larger sizes that may no longer physically reflect proteins being emulated.

Our analysis techniques and surface modulation methods can be widely adopted to improve our understanding of cell delivery processes,[19–21] which are plagued by the need to balance the seemingly opposing processes of endocytosis and endosomal escape, both of which can now be independently assessed in single cells.

3.4 Methods

Quantum Dot Synthesis. *(All QD synthesis done by Sung Jun Lim, UIUC)* Nanocrystals composed of (core)shell (CdSe)CdZnS were synthesized in organic solvents.[4] In sequential steps, 3.0 nm CdSe cores were synthesized and shells composed of 3.2 monolayers of CdS and 1.5 monolayers of ZnS were grown layer-by-layer. The resulting nanocrystals were coated with oleylamine and oleic acid and were purified by acetone precipitation and hexane-methanol extractions. Coating with pPEG,[5] pCOOH,[5] pZW,[22] and aCOOH[4] was performed according to our previously reported methodologies described in Supplementary Methods. For coating with mPEG, QDs in hexane were transferred to *N*-methlyformamide using tetramethylammonium hydroxide[5] and mixed with a 5,000-fold molar excess of methoxy-PEG-SH (2,000 Da; Rapp Polymere) at 60°C under nitrogen atmosphere with stirring for 3 hours. The QDs were then precipitated using anhydrous diethyl ether, dispersed in methanol, and precipitated again with a mixture of hexane and chloroform. The nanocrystals were then dispersed in 50 mM sodium borate buffer and centrifuged to remove possible aggregates. These QDs were stable for more than one week under ambient conditions at >1 μM concentration (Figure 3.4)

Optical Spectroscopy. *(Performed by Sung Jun Lim, UIUC)* Fluorescent spectra were measured using a NanoLog Horiba Jobin Yvon with Fluo Essence V3.5 software (Horiba Scientific). UV-Vis spectra were obtained using a Cary series UV-Vis-NIR spectrophotometer with Cary WinUV Scan Application Version 6.00 1551 software (Agilent Technologies).

Transmission Electron Microscopy of QDs. *(Performed by Sung Jun Lim, UIUC)* TEM images were obtained using a JEOL 2010 LaB6 high-resolution microscope in the Frederick Seitz Materials Research Laboratory Central Research Facilities at University of Illinois. For QDs in organic solvents, samples were prepared by placing a drop of dilute QD solution in hexane on an ultrathin carbon film TEM grid (Ted Pella; Product # 01824) and then wicking the solution off with a tissue.

pPEG and pCOOH Quantum Dot Coating. *(Ligands synthesized by and QDs coated by Liang Ma, UIUC)* A methanol solution of tetramethylammonium hydroxide (25%) was added to a biphasic mixture of *N*-methylformamide (NMF) and purified QDs in hexane. The suspension was stirred vigorously for 1 hour until the QDs were completely transferred to the NMF phase. Hexane was removed, and the NMF solution was washed with hexane twice. Residual hexane and methanol were evaporated under vacuum. A solution of pPEG or pCOOH in NMF (5:1 imidazole to QD surface atom) was added dropwise to the hydroxide-coated QDs in NMF (1 µM, 0.4 mL) with stirring under nitrogen atmosphere. The reaction was allowed to proceed at 110°C for 2 hours. The coated QDs were precipitated from NMF using anhydrous diethyl ether. The QDs were then dispersed in 50 mM sodium borate buffer (pH 8.5) and centrifuged to remove possible aggregates. The QDs were purified using centrifugal filtration (Amicon Ultra 50 kDa molecular weight cutoff) in 50 mM sodium borate buffer. The dilution–filtration cycle was performed five times.

pZW Quantum Dot Coating. *(Ligands synthesized by and QDs coated by Liang Ma, UIUC)* Purified QDs in hexane were transferred to NMF using the same method as for the pPEG and pCOOH polymers. pZW polymer dissolved in NMF was mixed with the hydroxide-coated QDs in NMF (1 µM, 0.4 mL) (5:1 thiol to QD surface atom) and purged with nitrogen for 2 minutes. The mixture was stirred at 110°C for 4 hours and then diluted with 50 mM sodium borate buffer (pH 8.5). The QDs were purified using centrifugal filtration (50 kDa molecular weight cutoff) in 50 mM sodium borate buffer. The dilution–filtration cycle was performed five times.

aCOOH Quantum Dot Coating. *(QDs coated by Liang Ma, UIUC)* Purified QDs were dispersed in chloroform (∼1 μM, 2-10 mL) and mixed with a 2,000-2,500-fold molar excess of aCOOH. Chloroform was slowly evaporated under vacuum with vigorous stirring. After complete evaporation, a 10 mM sodium hydroxide solution in distilled water (2–3 mL nmol^{-1}) was added and stirred for several hours until the amphipol-coated QDs were fully dispersed. Finally, the solution was centrifuged to remove possible aggregates.

mPEG-QD Stability. The stability of mPEG coated QDs in 50 mM sodium borate buffer was measured by centrifugation at 7000*g* for 10 minutes to remove any aggregates that may have formed due to coating instability. Concentrations were determined by measuring absorbance at 350 nm using a NanoDrop ND-1000 Spectrophotometer (Thermo Fisher Scientific).

DLS and Zeta Potential. *(Measurements taken by Liang Ma, UIUC)* Dynamic light scattering and zeta potentiometry were performed using a Zetasizer Nano ZS (Malvern Instruments Ltd.) with samples dispersed in 10 mM phosphate buffer (pH 7.4).

Cell Culture and Quantum Dot Delivery. A431, CHO, and HeLa cells (ATCC) were seeded at a density of 20,000 cells/cm^2 in LabTek chambers (Thermo Scientific), 24 hours before OPL treatment. CHO cells were cultured in Kaighn’s Modification of Ham’s F-12 Medium (Cell Media Facility, School of Chemical Sciences, UIUC). A431 cells and HeLa cells were cultured in Dulbecco’s Modified Eagle’s Medium (DMEM; Cell Media Facility, School of Chemical Sciences, UIUC) with 10% fetal bovine serum (FBS; HyClone) and 1% penicillin/streptomycin (P/S; Mediatech). Cells were washed twice with phosphate buffered saline, and the hypertonic loading reagent (Life Technologies) containing QDs (10 or 40 nM) was added. Cells were incubated for 10 minutes at 37°C, and then the medium was removed and replaced with hypotonic lysis medium composed of 6 parts incomplete DMEM without phenol red and 4 parts deionized water, for 3 minutes at 37°C. The medium was then replaced with complete DMEM without phenol red and the cells were incubated for 10 minutes at 37°C. Nuclei were stained with Hoechst (Sigma-Aldrich) for 20 minutes, followed by washing and treatment with BCG (200 μM; Sigma-Aldrich) in phenol red-free DMEM to quench any extracellular QDs, and cells were imaged within 45 minutes. The protocol was optimized to ensure that the majority of cells were viable (Figure 3.3). Hypertonic medium was the most toxic, so a maximum 10 minute exposure time was used. DAPI dye was used to positively identify dead cells, and positively-stained cells had similar D values as those not permeable to DAPI, indicating temporary permeabilization rather than death.[23] Notably, some cells observed by TEM demonstrated membrane damage, but major cellular structures remained intact. Further evaluation of cellular effects, such as changes in gene expression, were not pursued. For the passive uptake of QD, CHO cells were seeded at a density of 20,000 cells/cm^2 in LabTek chambers 24 hours before addition of 10 nM pPEG QDs in complete medium without phenol red. Uptake was assessed by microscopy after 24 hours, immediately after washing.

Fluorescence Microscopy. Fluorescence imaging was performed using wide-field illumination on a Zeiss Axio Observer.Z1 inverted microscope with a 100X 1.45 NA alpha Plan-Fluar oil immersion objective. QD images in cells were acquired with HILO excitation with a 488nm 100mW optically pumped semiconductor laser with 15% laser power at optimized HILO angles for our system (~60° from normal). Excitation light was excluded using a 482/18 nm laser-line bandpass filter (Semrock), and emission light was filtered with a 600/37 nm bandpass filter (Semrock). Images were acquired using a Photometrics eXcelon Evolve 512 EMCCD using Zeiss Zen software. QDs were imaged at 19.6 frames per second, 40 minutes after equilibration at 37°C with a focal plane set at the largest cross-section of the cell, a few microns above the center of the nucleus.

FCS Studies. HeLa cells were seeded at a density of ~84,000 cells/cm^2 in glass-bottom CellView dishes (Greiner Bio-One) 24 hours before OPL delivery of 240 nM pPEG-QDs. FCS data were acquired on an Alba FCS instrument (ISS) with a diode laser (470 nm) for excitation and single-photon avalanche photodiode detector. Each trace was acquired for 30 seconds at a frequency of 100,000 Hz.

To measure the confocal spot size of the FCS instrument, FCS data were acquired for a dye standard with known diffusion coefficient (Rhodamine 110; D = 17.6×10^{-10} m^{2}s^{-1}), and the resulting autocorrelation function, $G(\tau)$, was fit to the following equation:

$$G(\tau) = \frac{1}{N}\frac{\left[1 - F + F\exp\left(-\frac{\tau}{\tau_{triplet}}\right)\right]}{1 - F}\left(1 + \frac{\tau}{\tau_D}\right)^{-1}\left[1 + \frac{\tau}{\tau_D}\left(\frac{\omega_{xy}}{\omega_z}\right)^2\right]^{-\frac{1}{2}} \qquad (3.1)$$

where N is the average number of particles in the confocal volume, F is the triplet fraction, $\tau_{triplet}$ is the characteristic blinking time of the dye, τ_D is the characteristic decay time associated with the diffusion of the dye through the confocal volume, ω_{xy} is the xy-radius of the confocal spot, and ω_z is the z-radius of the confocal spot.[6] The spot sizes of $\omega_{xy} = 0.363$ µm and $\omega_z = 3.07$ µm were used as fixed parameters for subsequent FCS curve fittings.

To measure the characteristic blinking time for our QDs (τ_{blink}), FCS data for pPEG-coated QDs in aqueous buffer were acquired, and the resulting autocorrelation function was fit to the following equation:

$$G(\tau) = \frac{1}{N}\left[1 + \theta \exp\left(-\frac{\tau}{\tau_{triplet}}\right)\right]\left(1 + \frac{\tau}{\tau_D}\right)^{-1}\left[1 + \frac{\tau}{\tau_D}\left(\frac{\omega_{xy}}{\omega_z}\right)^2\right]^{-\frac{1}{2}} \tag{3.2}$$

where θ is a factor that accounts for the number of particles in a nonfluorescent state.[24] The result of this measurement was τ_{blink}= 187 µs, which was used as a fixed parameter for subsequent fitting of FCS curve fittings.

Autocorrelation functions for pPEG-QDs in cells were fit to a multicomponent anomalous diffusion model shown below:

$$G(\tau) = \frac{1}{N}\left[1 + \theta \exp\left(-\frac{\tau}{\tau_{triplet}}\right)\right]\sum_n A_n\left[1 + \left(\frac{\tau}{\tau_{D,n}}\right)^{\alpha_n}\right]^{-1}\left[1 + \left(\frac{\tau}{\tau_{D,n}}\right)^{\alpha_n}\left(\frac{\omega_{xy}}{\omega_z}\right)^2\right]^{-\frac{1}{2}} \tag{3.3}$$

where α_n is the confinement parameter for the nth component, and A_n is the fractional contribution the nth component to the total curve. Each fit was calculated with 1 to 4 components. Minima of the Akaike information criteria (AIC) were used to determine the number of fitted components. The diffusion coefficient D_n for each component was calculated by using the following equation:[8]

$$D_n = \frac{\omega_{xy}^2}{4\tau_{D,n}} \tag{3.4}$$

Simulation Analysis. Trajectories were simulated using the MATLAB *wfbm* function, which generates a fractional Brownian motion trajectory with specified α, when normalized by standard deviation. Trajectories were scaled by D, and a series of normally distributed measurement errors were added to each position in each dimension.[25] Measurement errors derived from a distribution with zero mean and a standard deviation derived from the mean experimental localization error from the SPT analysis for each QD coating class. Track lengths were truncated to match the distribution of experimentally measured track lengths for each QD coating (Figure 5.10). These simulated trajectories were analyzed using the diffusion analysis method described above.

Nonspecific Adsorption Experiments. HeLa cells were seeded at a density of 72,000 cells/cm^2 in CellView dishes (VWR), 24 hours before OPL treatment. Cells were washed twice with phosphate buffered saline, and the hypertonic loading reagent (Life Technologies) containing mPEG-QDs (10 nM) with or without 0.5x casein blocking buffer (Sigma-Aldrich) was added. Cells were incubated for 10 minutes at 37°C, and the medium was removed and replaced with hypotonic lysis medium. All subsequent steps for OPL delivery described in the main text methods were then followed.

Statistical Analysis. All error bars are standard error of the mean values, unless indicated otherwise. All p-values were calculated using a two-tailed t-test, unless indicated otherwise.

3.5 References

1. Dix, J. A. & Verkman, A. S. Crowding effects on diffusion in solutions and cells. *Annu. Rev. Biophys.* **37,** 247–63 (2008).
2. Okada, C. Y. & Rechsteiner, M. Introduction of macromolecules into cultured mammalian cells by osmotic lysis of pinocytic vesicles. *Cell* **29,** 33–41 (1982).
3. Bausinger, R. *et al.* The Transport of Nanosized Gene Carriers Unraveled by Live-Cell Imaging. *Angew. Chemie Int. Ed.* **45,** 1568–1572 (2006).
4. Lim, S. J. *et al.* Brightness-equalized quantum dots. *Nat. Commun.* **6,** 8210 (2015).
5. Ma, L. *et al.* Multidentate Polymer Coatings for Compact and Homogeneous Quantum

Dots with Efficient Bioconjugation. *J. Am. Chem. Soc.* **138,** 3382–3394 (2016).
6. Bachir, A. I., Kolin, D. L., Heinze, K. G., Hebert, B. & Wiseman, P. W. A guide to accurate measurement of diffusion using fluorescence correlation techniques with blinking quantum dot nanoparticle labels. *J. Chem. Phys.* **128,** 06B607 (2008).
7. Sheung, J. Y. *et al.* Structural Contributions to Hydrodynamic Diameter for Quantum Dots Optimized for Live-Cell Single-Molecule Tracking. *J. Phys. Chem. C* **122,** 17406–17412 (2018).
8. Banks, D. S., Tressler, C., Peters, R. D., Höfling, F. & Fradin, C. Characterizing anomalous diffusion in crowded polymer solutions and gels over five decades in time with variable-lengthscale fluorescence correlation spectroscopy. *Soft Matter* **12,** 4190–4203 (2016).
9. Saxton, M. J. & Jacobson, K. Single-particle tracking: applications to membrane dynamics. *Annu. Rev. Biophys. Biomol. Struct.* **26,** 373–99 (1997).
10. Qian, H., Sheetz, M. P. & Elson, E. L. Single particle tracking. Analysis of diffusion and flow in two-dimensional systems. *Biophys. J.* **60,** 910–921 (1991).
11. Ernst, D. & Köhler, J. Measuring a diffusion coefficient by single-particle tracking: statistical analysis of experimental mean squared displacement curves. *Phys. Chem. Chem. Phys.* **15,** 845–849 (2013).
12. Ernst, D. & Köhler, J. How the number of fitting points for the slope of the mean-square displacement influences the experimentally determined particle size distribution from single-particle tracking. *Phys. Chem. Chem. Phys.* **15,** 3429–3432 (2013).
13. Sinha, B. *et al.* Cells respond to mechanical stress by rapid disassembly of caveolae. *Cell* **144,** 402–413 (2011).
14. Gilleron, J. *et al.* Image-based analysis of lipid nanoparticle--mediated siRNA delivery, intracellular trafficking and endosomal escape. *Nat. Biotechnol.* **31,** 638 (2013).
15. Shao, Q. & Jiang, S. Molecular understanding and design of zwitterionic materials. *Adv. Mater.* **27,** 15–26 (2015).
16. McElligott, M. A. & Dice, J. F. Microinjection of cultured cells using red-cell-mediated fusion and osmotic lysis of pinosomes: a review of methods and applications. *Biosci. Rep.* **4,** 451–466 (1984).
17. Park, R. D., Sullivan, P. C. & Storrie, B. Hypertonic sucrose inhibition of endocytic transport suggests multiple early endocytic compartments. *J. Cell. Physiol.* **135,** 443–450 (1988).
18. Storrie, B., Pool, R. R., Sachdeva, M., Maurey, K. M. & Oliver, C. Evidence for both prelysosomal and lysosomal intermediates in endocytic pathways. *J. Cell Biol.* **98,** 108–115 (1984).
19. Time to deliver. *Nat. Biotechnol.* **32,** 961 (2014).
20. Stewart, M. P., Lorenz, A., Dahlman, J. & Sahay, G. Challenges in carrier-mediated intracellular delivery: moving beyond endosomal barriers. *Wiley Interdiscip. Rev. Nanomedicine Nanobiotechnology* **8,** 465–478 (2016).
21. Stewart, M. P. *et al.* In vitro and ex vivo strategies for intracellular delivery. *Nature* **538,** 183 (2016).
22. Lim, S. J. *et al.* Lipoprotein Nanoplatelets: Brightly Fluorescent, Zwitterionic Probes with Rapid Cellular Entry. *J. Am. Chem. Soc.* **138,** 64–67 (2016).
23. Chakrabarti, R., Pfeiffer, N. E., Wylie, D. E. & Schuster, S. M. Incorporation of monoclonal antibodies into cells by osmotic permeabilization. Effect on cellular metabolism. *J. Biol. Chem.* **264,** 8214–8221 (1989).
24. Bestvater, F. *et al.* EMCCD-based spectrally resolved fluorescence correlation

spectroscopy. *Opt. Express* **18,** 23818–23828 (2010).
25. Kepten, E., Weron, A., Sikora, G., Burnecki, K. & Garini, Y. Guidelines for the fitting of anomalous diffusion mean square displacement graphs from single particle tracking experiments. *PLoS One* **10,** e0117722 (2015).

CHAPTER 4: SINGLE QUANTUM DOT TRACKING TO OPTIMIZE LABELING OF INTRACELLULAR PROTEINS IN LIVING CELLS

4.1 Background

4.1.1 Labeling Intracellular Proteins in Living Cells

A longstanding goal in biology is to understand the behavior of proteins, especially those involved in cell signaling, in their native cellular environments. Although many advances have been made in understanding the behavior of purified proteins *in vitro*, there is still a major gap in understanding how this information translates into the cellular environment, especially at the single-molecule level. This level of information will require the ability to follow single proteins at time scales ranging from seconds to minutes. This would not be possible with fluorescent proteins, which can only be tracked for seconds before they photobleach. With their superior brightness and photostability, QDs are uniquely positioned to fill this role.[1]

QD labeling of membrane-bound proteins and receptors have revealed many previously unknown mechanisms in cell signaling and neuron biology. However, there is still a major challenge to deliver QDs targeted to specific intracellular proteins in order to track them to reveal single-molecule dynamics. Although there have been seminal demonstrations of the intracellular delivery of QDs that localize to specific subcellular regions via localization sequences and the delivery of QD-motor protein conjugates that demonstrate the distinctive linear motion of motor proteins, none of these studies had quantitative confirmation of binding to specific intracellular targets or appropriate controls demonstrating the degree to which the targeting is specific.[2–4] More recent studies have reported varying degrees of intracellular labeling.[5,6] However, the results presented only have qualitative evidence of labeling[5] or show homogeneous over-labeling of the target[6]. In this chapter, we present the labeling of a fusion protein with QD-probes delivered via OPL to live cells, along with quantitative comparison of the labeling efficiency with specific control comparisons.

4.1.2 HaloTag Protein System

The first step in labeling a cytoplasmic protein with a QD probe is to design a coupling strategy. Here we target proteins expressed as fusions to the HaloTag protein. HaloTag protein is a modified bacterial haloalkane dehalogenase that bonds with aliphatic hydrocarbons with halide groups.[7] This binding is covalent, efficient, and occurs fast, with a second-order rate constant of $2.7\times10^6\ M^{-1}s^{-1}$, which is comparable to that of streptavidin-biotin. [7] The structure of the HaloTag protein and how it binds with a commercially available chloroalkane-based ligand is depicted in Figure 4.1

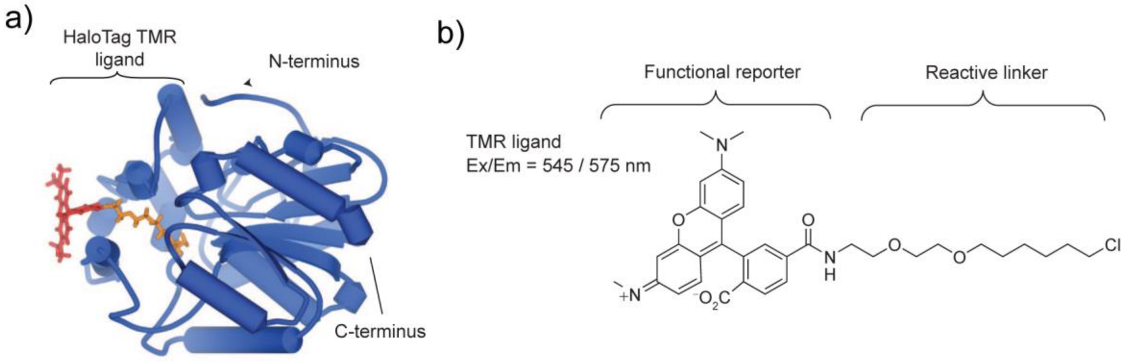

Figure 4.1 HaloTag protein system. (a) Model of the HaloTag protein with covalently bound TMR HaloLigand. (b) Detailed chemical structure of the commercially available TMR HaloLigand from Promega. Figure adapted from Ref 7.

4.2 Data and Results

4.2.1 Transgene Target System

Our chosen target system for was a fusion protein HaloTag-GFP-ActA. ActA is a protein that binds to the cytoplasmic face of the outer mitochondrial membrane.[8] The HaloTag-GFP-

ActA plasmid was provided as a gift from the Selvin Lab at UIUC. The plasmid is described in further detail in Teng, et. al. in their recent publication.[9] The design of the probe allows for positive identification of cells expression the fusion protein via the GFP subunit (Fig 4.2b). HeLa cells were transiently transfected with this plasmid using Lipofectamine2000. Details of the transfection protocol can be found in the Methods section. We confirmed the presence of the HaloTag subunit by testing with the commercially available TMR- HaloLigand from Promega Corporation. The spatially identical GFP and TMR signals confirmed the successful expression of the HaloTag-GFP-ActA transgene (Fig 4.2b-c).

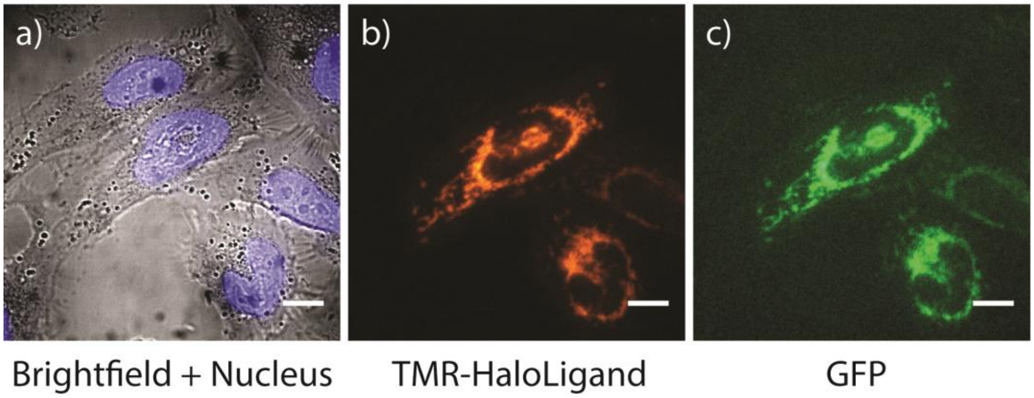

Figure 4.2 Fluorescence images of HeLa cells transfected with HaloTag-GFP-ActA at 100x magnification confirming the expression of the fusion protein. (a) Transmitted light and nuclear stain (blue) (b) TMR-HaloLigand labeling of the HaloTag subunit of the HaloTag-GFP-ActA fusion protein. (c) GFP fluorescence channel with identical spatial distribution to the TMR-HaloLigand signal. All scale bars are 10 μm.

4.2.2 QD Imaging Probe Design

In designing a QD-probe to target HaloTag-GFP fusion proteins intracellularly three major requirements needed to be met: (i) minimal spectral overlap with GFP, (ii) monodispersity, and (iii) chemically active targeting ligand for HaloTag labelling.

Even at emission wavelengths longer than 550 nm GFP has a long “red tail” that is characteristic of many fluorescent proteins and organic dyes. This spectral bleed through to the red emission range is particularly problematic for single-molecule imaging, which requires low background for accurate single particle detection. In order to minimize interference from GFP, we used a HgCdSe(CdS/CdZnS) core(shell) QDs with emission at 800 nm, which is sufficiently red-shifted into the near infrared in order to avoid bleed through from GFP (Fig 4.3).[10]

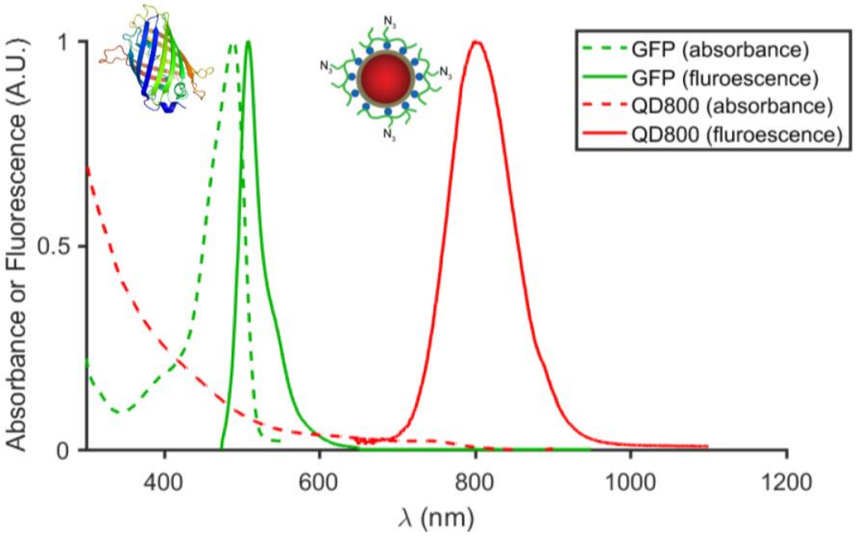

Figure 4.3 Minimizing spectral overlap of GFP and QD800 fluorescence. Absorbance and fluorescence spectra of GFP and 800 nm emitting QDs. GFP spectral information and inset schematic depiction adapted from references [11,12].

We coated these QDs with a modified version of the pPEG coating from the previous chapter that has azide functional groups to allow for conjugation of appropriate targeting ligands (detailed structure in Fig 4.4a). This coating resulted in a water soluble QD population that was almost entirely monodisperse (see Fig 4.4b).

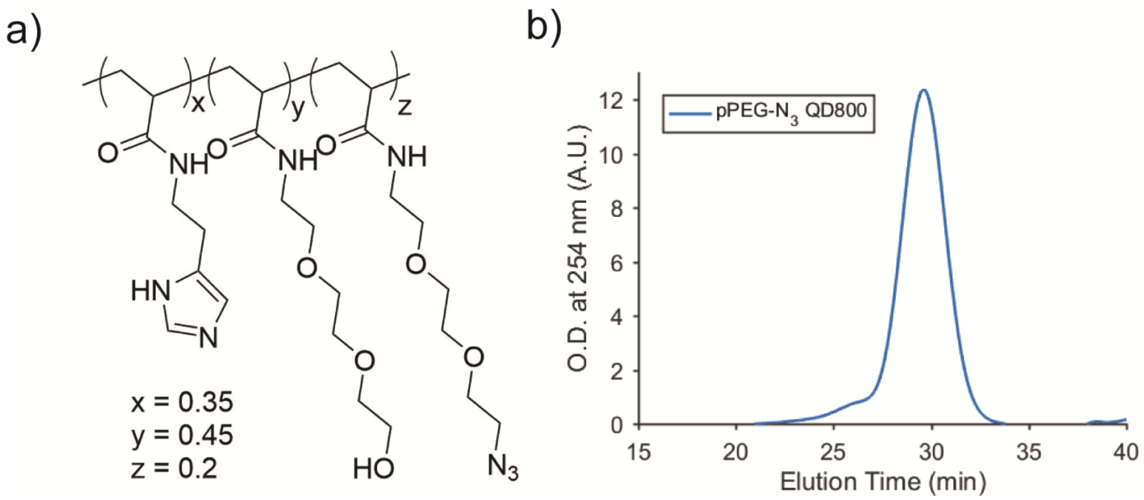

Figure 4.4 pPEG-N_3 coated QD800. (a) Detailed structure of pPEG coating ligand with azide functional groups for bioconjugation. (b) FPLC characterization of pPEG-N_3-coated QD800 showing a monodisperse population.

As described earlier, using the HaloTag requires chloroalkane groups on the targeting molecule. Here we use a type of copper-free click-chemistry to accomplish this. Click-chemistry is a class of biocompatible conjugation strategies that have high specificity and efficiency. For use with semiconductor nanocrystals, it is important to specifically use copper-free click chemistry, as copper catalysts are not compatible with QDs. We used an azide-alkyne based click-chemistry.[13] Specifically, the pPEG polymer coating, which was introduced in the previous chapter, was modified to have terminal azide groups, which are reactive after QD-coating (Figure 4.4a). [14] These azide groups can be conjugated to the strained alkyne dibenzycyclooctyne (DBCO), as depicted in Figure 4.5, in a reaction that proceeds with high efficiency, without catalysts in aequeous solution. [13]

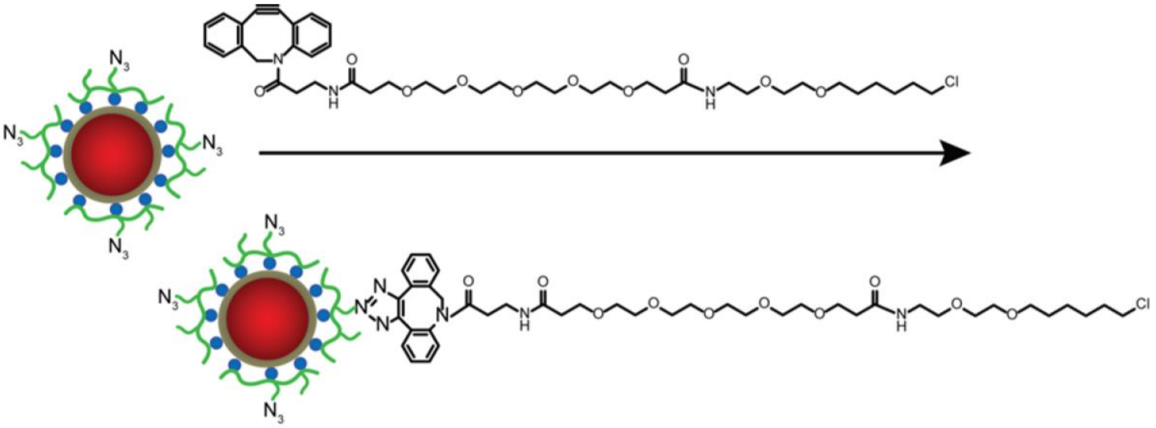

Figure 4.5 Schematic depiction of DBCO-chloroalkane conjugation to pPEG-N_3-coated QDs via DBCO-azide copper-free click chemistry.

Confirmation of the chloroalkane-QD conjugation was confirmed by gel electrophoresis. The amount of chloroalkane had to be balanced because if the chloroalkane: QD ratio was too low, then HaloTag protein-QD binding was incomplete or undetectable (see Fig 4.6). On the other hand, the conjugation of too much of the hydrophobic chloroalkane molecules would destabilize the pPEG coating causing QD aggregation.

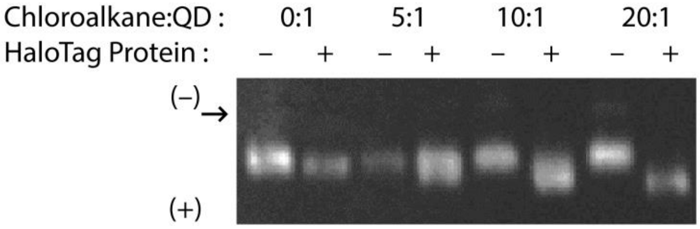

Figure 4.6 Chloroalkane-QD conjugation and ratio optimization. Gel electrophoresis results showing the optimized chloroalkane:QD ratio where the amount of gel shift in the lanes with HaloTag protein indicate the amount of QD-protein binding. The chloroalkane:QD ratio of each sample and whether or not the QDs were incubated for 1h with 10x molar excess HaloTag protein is indicated above each lane. The arrow indicates the position of the wells where the samples were initially loaded, and the (+) and (-) signs indicate the polarity of the gel. The 0:1 ratio shows no gel shift, hence no protein binding; 5:1 and 10:1 show partial protein binding; and 20:1 shows a complete shift of the gel band, hence complete binding of the QDs to the HaloTag protein.

Thus, we found the minimal chloroalkane:QD ratio that resulted in a stable chloroalkane-QD conjugate was 20:1. The specificity of the final conjugate to the ligand tunnel of the HaloTag protein (see Figure 4.1), we tested the reactivity of the chloroalkane-QD conjugates with HaloTag protein that had been incubated with 10x molar excess TMR-HaloLigand demonstrating that the chloroalkane-QDs did not have nonspecific binding to other protein residues (see Fig 4.7).

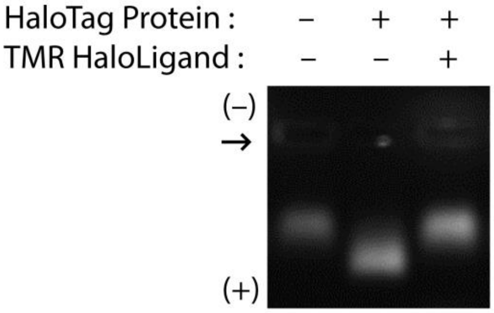

Figure 4.7 Chloroalkane-QD specificity for HaloTag protein. Gel electrophoresis results showing the specificity of 20:1 chloroalkane-QDs. The presence or absence of 10x molar excess TMR HaloLigand and whether or not the QDs were incubated for 1h with 10x molar excess HaloTag protein is indicated above each lane. The arrow indicates the position of the wells where the samples were initially loaded, and the (+) and (-) signs indicate the polarity of the gel. The lane without HaloTag protein and without the TMR HaloLigand indicates the distance that the QDs migrated without binding to the HaloTag protein; the lane with HaloTag protein but no TMR HaloLigand indicates the gel shift introduced from protein binding. As the band in the lane with both HaloTag protein and TMR HaloLigand has the same migration distance as the first well, this indicates a lack of QD-protein binding and the specificity of the 20:1 chloroalkane QDs for the HaloTag protein.

4.2.3 Mitochondrial Labeling

***Experimental Details*:** Chloroalkane-QD delivery by OPL was identical to the optimized delivery conditions describe in chapters 4 and 5 with a few key exceptions. First of all, BCG does not work as an extracellular quencher for QDs with 800 nm emission, as the peak absorbance of BCG does not align with the emission peak of these QDs. Instead we used indocyanine green (ICG), a small molecule dye that has strong absorbance around 800 nm in aqueous solution making it well suited to be an extracellular quencher for GFP (see Fig 4.8).[15] Both the quenching capability and cell membrane impermeability were confirmed experimentally.

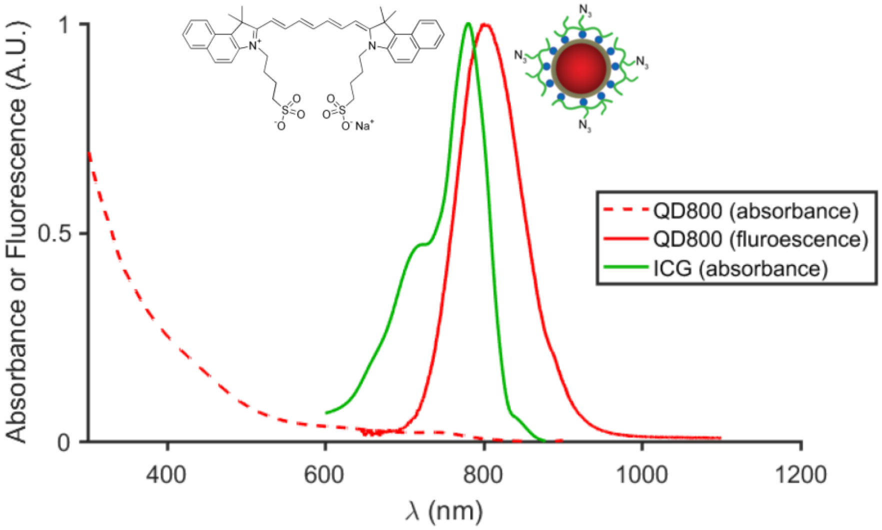

Figure 4.8 Suitability of indocyanine green (ICG) as an extracellular quencher for 800nm emitting QDs. Absorption spectrum for ICG and spectra for QD800, demonstrating strong overlap of ICG absorption and QD800 fluorescence emission. ICG spectral information adapted from Ref 15.

Additionally, QD imaging was performed 4 h after QD delivery, as opposed to less than 1 h when studying QD diffusion and delivery. This is because although the HaloTag- chloroalkane reaction is very efficient *in vitro*, the intracellular environment is vastly different due to crowding, lower effective concentrations, etc., which is expected to slow down reaction rates (refs). We empirically found that much longer time periods were required to see evidence of QD QDs binding to the HaloTag protein targets. On a similar note, the QD delivery concentration had to be increased to 160 nM for two reasons: (1) Higher numbers of QDs were necessary to clearly visualize QDs binding to their target proteins and (2) conjugation of additional hydrophobic groups to the QD surface appeared to decrease the efficiency of QD delivery by OPL at a given concentration. This is likely due to decreased QD interaction with the extracellular membrane, similar to the trend described in Chapter 3 in section 3.2.3.

In order to have a control for comparison, a subset of the cells being imaged were treated to block the HaloTag subunit of the fusion protein using a cell membrane permeable Biotin HaloLigand purchased from Promega. The details of this HaloTag blocking are in the methods section below under the heading *HaloTag Pre-Blocking*. Given the specificity of the chloroalkane-QDs in binding to the HaloTag protein, if there is a measurable difference in the behavior of the QD probes in these two groups, then we should be able to establish the successful QD-labeling of the target fusion protein.

Analysis Workflow: HILO movies of the intracellular QDs were analyzed by SPT and single-molecule diffusion analysis, as detailed in Chapter 4. A simple look at the D-α space does not show a clear difference between the two groups (Figure 4.9).

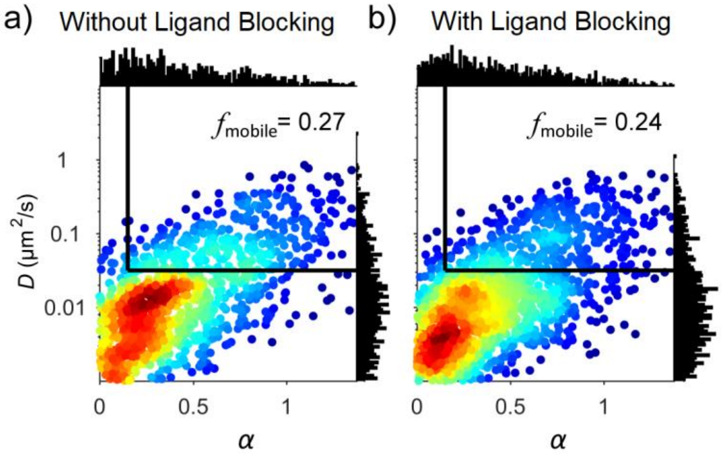

Figure 4.9 D vs α heat maps of chloroalkane-QD mobility 4h after delivery with and without ligand blocking. Heat map of diffusion coefficient, D, versus confinement parameter, α for Histograms of D and α are projected on the x and y axes, respectively, and thresholds imposed for mobility are shown as black lines, yielding f_{mobile} shown in each plot. (a) Without ligand blocking and (b) With ligand blocking. n = 13 and 16 cells respectively.

However, a qualitative assessment of where the immobilized trajectories are relative to the GFP signal for both groups shows that in the group without ligand blocking the immobilized QDs appear to have an increased association with the GFP signal, while this is not the case for the group with ligand blocking (Figure 4.10). Since the key outcome in this experiment was the labeling of the Halo-GFP-ActA fusion protein expressed on the mitochondrial membrane, we had to quantitatively assess the colocalization of the detected QD spots with the GFP signal.

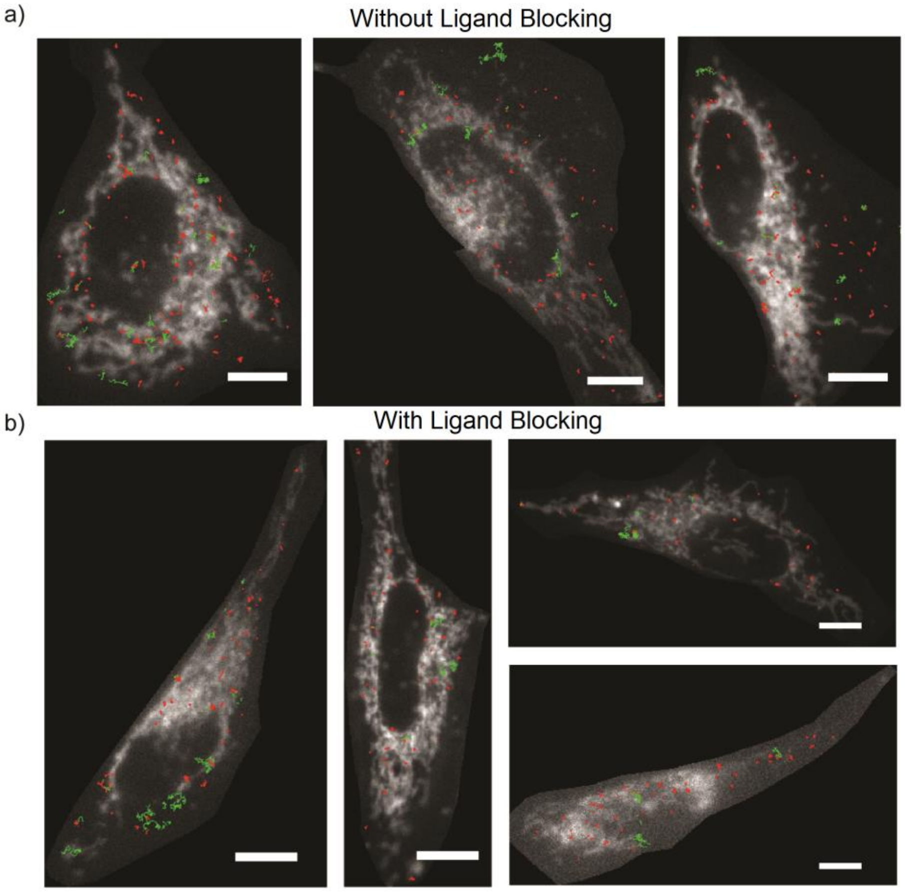

Figure 4.10 Representative images of QD colocalization with GFP fluorescence. GFP fluorescence images with superimposed single-particle tracks from chloroalkane-QDs, with the green trajectories corresponding to mobile QDs and red trajectories corresponding to immobile QDs for a) the group without ligand blocking and (b) the group with ligand blocking and showing qualitative association of the immobilized QDs with the GFP signal in the group without ligand blocking. All scale bars are 10 μm.

Traditional fluorescence colocalization approaches and metrics are defined to quantify the degree of colocalization of two fluorescently labeled proteins, usually in order to see if the two proteins are co-expressed and have a spatial relationship.[16,17] However, these metrics do not work well with our data because there are far more Halo-GFP-ActA than the amount of QDs available. In this case, we needed to define a new colocalization score that could quantify the relative GFP intensity associated with the detected QD positions. This GFP colocalization score (CS_{GFP}) was defined as follows for a given single-particle trajectory:

$$CS_{GFP} \equiv \frac{1}{L}\sum_{i=1}^{L}\frac{I_{GFP}(x_i, y_i) - I_{GFP,bg}}{2^n} \tag{4.1}$$

where L is the length of the trajectory in frames, $I_{\mathrm{GFP}}(x_i,y_i)$ is the average GFP intensity of a 3x3 pixel area centered on the (x,y) coordinated of the single-particle trajectory at the i^{th} time point or frame, $I_{\mathrm{GFP,bg}}$ is the average background intensity of the GFP channel, and n is the bit depth that the GFP fluorescence was acquired at ($n = 8$ in our case). The denominator and background subtraction normalized the colocalization score so that it is a unitless score that varies between 0 and 1, where 0 means the trajectory has not association with the GFP signal and 1 means the trajectory was fully colocalized with GFP with saturated pixels.

Colocalization Results: We analyzed 13 videos of cells in the group without ligand blocking and 16 videos for the group with ligand blocking and calculated the CS_{GFP} for reach detected trajectory. This resulted in a total of 1096 trajectories and colocalization scores for the group without ligand blocking and 14871 trajectories and scores for the group with ligand blocking. The distributions of colocalization results for both groups are compared in Figure 4.11 below.

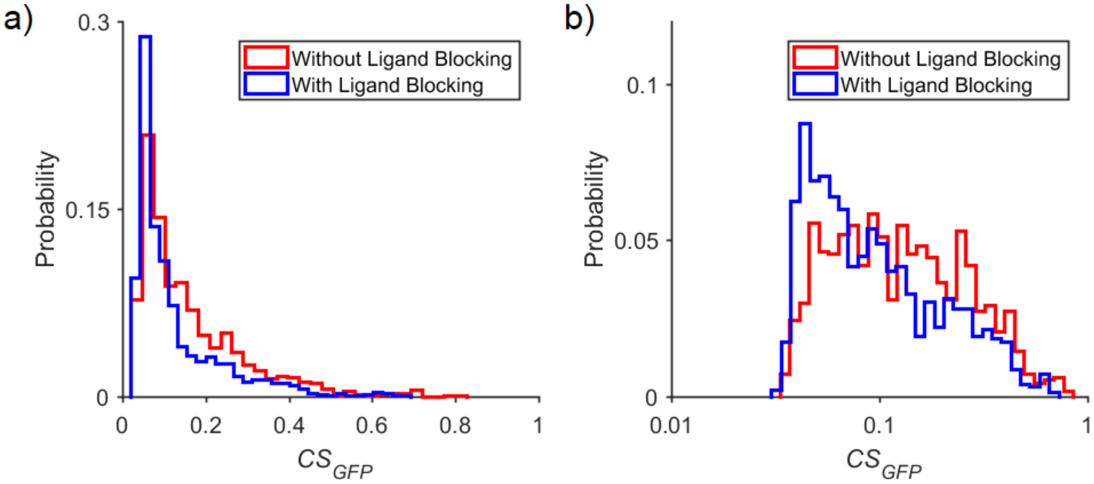

Figure 4.11 Histograms comparing GFP colocalization scores without ligand blocking (red) and with ligand blocking (blue) shown in (a) linear scale and (b) logarithmic scale, to emphasize the range over which the differences between the two groups are clearer.

As the calculated colocalization scores are trajectory-level data, it is also possible to compare the CS_{GFP} values for just the subset of immobile QDs, as defined by the thresholds calculated in Chapter 2 (Figure 4.12).

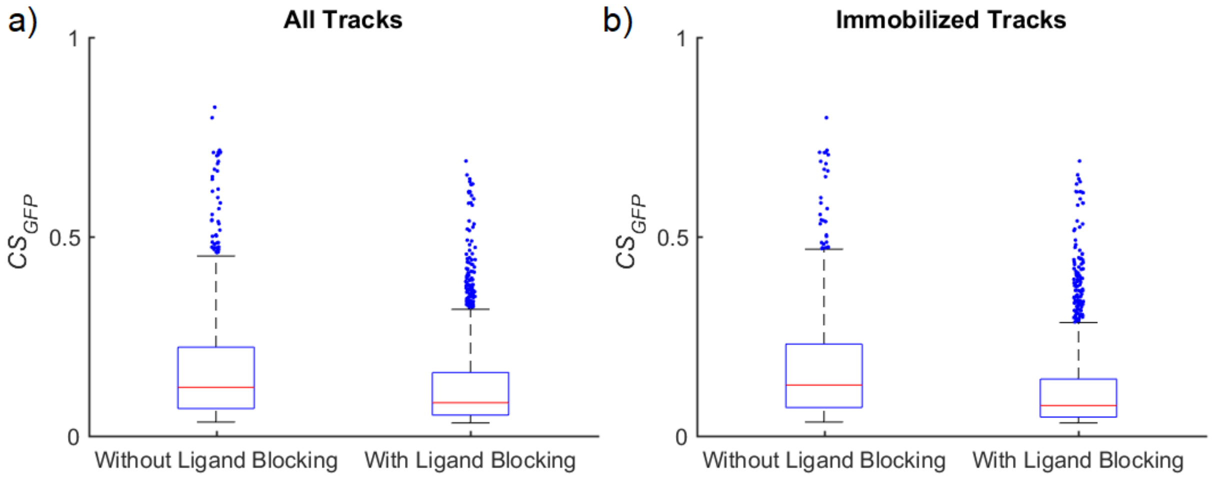

Figure 4.12 Box plots of GFP colocalization scores for (a) the set of all detected tracks and (b) the subset of immobile tracks. The red line in the box corresponds to the median of the corresponding datasets, and the upper and lower bounds of the box mark the first and third quartile of the data. The length of the whiskers corresponds to 1.5 time the adjacent interquartile range, with any data points outside of these bounds represented by blue points.

As the CS_{GFP} distributions in Figure 4.10 don't appear to be normally distributed, we used a two-sided Wilcoxon rank sum test, which is equivalent to the Mann Whitney U-test, to test the hypothesis that the two distributions are statistically distinct with unequal median values. Comparing the set of all trajectories with this test resulted in a p-value of 6.073×10^{-23}, and comparing the subset of just the immobilized QDs yielded a p-value of 7.24×10^{-34}, showing that the two groups have statistically distinct levels of colocalization with GFP.

4.3 Discussion

Here we presented specific targeting of intracellular proteins in live cells with externally delivered QD-probes. Furthermore, we used quantitative verification of the targeted labeling by characterization of the degree of colocalization with the target fusion protein showing an increased colocalization of the QD-probe with the target protein in the group without ligand blocking. Additionally, in the subset of the immobilized QD-probes the group without ligand blocking showed even higher levels of colocalization with the target protein when compared to the group with ligand blocking.

Currently, there are two competing processes resulting in immobilized QDs: (1) specific immobilization from the chloroalkane-QDs binding to the HaloTag protein target and (2) the nonspecific background binding of the QDs. With the current targeting methodology, 3-4 hours are necessary for the QD-probes to show distinct association with the mitochondria. However, in this time period, the level of background binding is significant enough to decrease the mobile fraction of the QDs to nearly 25%. This means that in the time required for the chloroalkane-QDs to bind to their target, QD-probes in the group with ligand blocking could also randomly immobilize in the proximity of the target proteins, yielding to apparent or false-positive binding to the target.

The degree of targeting and distinction over background binding could be improved in two major ways: (1) by reducing the background binding over the time period required for the probe to bind to the target molecule or (2) by increasing the efficiency of the probe binding to the target molecule, so that the required time period is shorter. The first goal could be achieved by using a pZW-based coating with azide functional groups that may remain mobile and diffusive over the time period required for the targeting chemistry to proceed to completion, as zwitterions are less likely to destabilize due to their increased level of hydration and limited interaction with the hydrophobic domains of intracellular proteins.[18] Additionally, we could try to model the process of random or nonspecific immobilization to see what the CS_{GFP} would be given a particular GFP spatial distribution for completely random immobilization due to background binding.

4.4 Methods

Quantum Dot Synthesis. *(QDs synthesized by Suresh Sarkar, UIUC)* Nanocrystals composed of (core)shell ($Hg_xCd_{(1-x)}Se$)CdZnS were synthesized in organic solvents.[10] In sequential steps, ~3.2 nm CdSe cores were synthesized and Hg exchange process was performed taking the CdSe core in chloroform.[10] After the purification, $Hg_xCd_{(1-x)}Se$ core was capped with shells composed of 3.2 monolayers of CdS and 1.5 monolayers of ZnS grown layer-by-layer. The final nanocystals were purified by several times precipitation with 1:5 mixture of methanol and acetone followed by re-dispersing in hexane.

pPEG-N_3 Quantum Dot Coating. *(QDs coated and characterized by Zhiyuan Han, UIUC)* A methanol solution of tetramethylammonium hydroxide (25%) was added to a biphasic mixture of *N*-methylformamide (NMF) and purified QDs in hexane. The suspension was stirred vigorously for 1 hour until the QDs were completely transferred to the NMF phase. Hexane was removed, and the NMF solution was washed with hexane twice. Residual hexane and methanol were evaporated under vacuum. A solution of pPEG-N_3 in NMF (5:1 imidazole to QD surface atom) was added dropwise to the hydroxide-coated QDs in NMF (1 µM, 0.4 mL) with stirring under nitrogen atmosphere. The reaction was allowed to proceed at 110°C for 2 hours. The coated QDs were precipitated from NMF using anhydrous diethyl ether. The QDs were then dispersed in 50 mM sodium borate buffer (pH 8.5) and centrifuged to remove possible aggregates. The QDs were purified using centrifugal filtration (Amicon Ultra 50 kDa molecular weight cutoff) in 50 mM sodium borate buffer. The dilution–filtration cycle was performed five times. Monodispersity of coated QDs was assessed by size exclusion chromatography.

Synthesis of DBCO modified chloroalkane. *(Synthesized by Liang Ma, UIUC)* Chloroalkane amine was first synthesized according to literature reports.[19] Then 3.22 mg of chloroalkane amine (14.4 μmol) in dry DMF (100 μl) was mixed with 2 mg of DBCO-TEG$_5$-NHS ester (2.8 μmol) in dry DMF (200 μl). After addition of 9.3 mg of DIPEA (12 μl), the mixture was incubated overnight under shaking. The successful synthesis of DBCO modified chloroalkane was confirmed by ESI-MS (low resolution, positive mode): calculated for $C_{42}H_{60}ClN_3O_{10}$, m/z 801.4 $[M]^+$; found 802.4 $[M+H]^+$. The product was used without purification for the next step.

Chloroalkane-QD Preparation. Chloroalkane-QD conjugates were prepared within 24h of usage in cells. Conjugation was performed by mixing pPEG-N$_3$-coated QDs with DBCO-chloroalkane in 50 mM borate buffer (20:1 molar ratio of chloroalkane:QD), with the final QD concentration being approximately 1μM. The conjugation was allowed to proceed for 10-12 h at room temperature, after which the free DBCO-chloroalkane was purified 4 times using a centrifugal filter with a 30 kDa molecular weight cutoff (Millipore). Conjugation was confirmed using electrophoresis in a hybrid polyacrylamide-agarose gel (2% polyacrylamide and 0.5% agarose) at 4° C.

Cell Culture and Plasmid Transfection. HeLa cells (ATCC) were seeded at a density of 150,000 cells/cm^2 in LabTek chambers (Thermo Scientific), 3 days before delivery of QD conjugates. Cells were cultured in Dulbecco's Modified Eagle's Medium (DMEM; Mediatech) with 10% fetal bovine serum (FBS; HyClone) and 1% penicillin/streptomycin (P/S; Mediatech). 12-24 hours after initial seeding, cells were transfected with ActA-GFP-HaloTag plasmid, which was provided by Prof. Paul Selvin's lab (UIUC). Lipoefectamine-DNA complexes were prepared (for each well to be transfected) by mixing 0.8 μg plasmid with 2 μL Lipofectamine2000 (Invitrogen) in 100 μL incomplete DMEM for 20 minutes. Before addition of the lipofectamine-DNA complexes to the cultured cells, the culture media was replaced with DMEM supplement only with 10% FBS, and then 100 μL of the DMEM with lipofectamine-DNA was added. The transfection was allowed to proceed for 3h, after which the culture media was replaced with DMEM with 10% FBS. Transgene expression was verified by fluorescence microscopy 24-48h after transfection.

HaloTag Pre-Blocking. Before starting the QD delivery process, 10 μM of HaloTag biotin ligand (Promega, Product No. G828B) was added to the designated control wells for 100 minutes, in order to pre-block the target HaloTag proteins. In the subsequent designated steps, 10 μM of HaloTag biotin ligand was also included for the control wells in order to provide continuous blocking of the HaloTag target proteins.

Quantum Dot Delivery. Cells were washed twice with phosphate buffered saline, and the hypertonic loading reagent (Life Technologies) containing 160 nM chloroalkane-QD conjugates was added (HaloTag pre-blocking included for control wells). Cells were incubated for 10 minutes at 37°C, and then the medium was removed and replaced with hypotonic lysis medium composed of 6 parts incomplete DMEM without phenol red and 4 parts deionized water, for 3 minutes at 37°C. The medium was then replaced with complete DMEM without phenol red and the cells were incubated for 10 minutes at 37°C, after which the media was replaced with fresh phenol red free DMEM. The cells were incubated at 37°C for 4 h in order to allow the QD-conjugates to label the HaloTag target proteins (HaloTag pre-blocking included for control wells). Immediately before imaging, indocynanine green (1.44 µM; Pfaltz and Bauer) diluted in phenol red-free DMEM was added to quench any extracellular QDs.

Fluorescence Microscopy. Fluorescence imaging was performed using wide-field illumination on a Zeiss Axio Observer.Z1 inverted microscope with a 100X 1.45 NA alpha Plan-Fluar oil immersion objective. Before QD images were acquired a single GFP channel image was acquired using lamp excitation and a standard GFP filter set (Zeiss). QD images in cells were acquired with HILO excitation with a 488nm 100mW optically pumped semiconductor laser with 15% laser power at optimized HILO angles for our system (~60° from normal). Excitation light was excluded using a 482/18 laser-line bandpass filter (Semrock), and emission light was filtered with a 835/70 bandpass filter (Semrock). Images were acquired using a Photometrics eXcelon Evolve 512 EMCCD using Zeiss Zen software. QD-conjugates were imaged 4 h after delivery at 19.6 frames per second, over the course of an hour at 37°C with a focal plane set at the largest cross-section of the cell.

Diffusion Analysis. Single-molecule videos were analyzed by SPT using the MATLAB u-track software package developed by Jaqaman, *et al.*[20] to determine centroid pixel positions (x_o,y_o) for trajectories at each time point t. Custom MATLAB scripts were used to calculate mean squared displacement (MSD) versus time increment (τ) curves for each particle trajectory and were fit to a model of anomalous diffusion in Equation 2.2.[21–24] For tracks longer than 100 frames, curves were fit for the first 10 time increments, whereas ¼ of the track length was fit for shorter tracks. Tracks shorter than 10 frames were discarded. These lengths were selected based on recommendations of Kepten and colleagues for tracks in the regime of strong subdiffusion to weak superdiffusion ($\alpha = 0.3$-1.3) with low localization error.[25] Curve fits were filtered based on the calculated error of the fitting parameters with error tolerances of 0.05 $\mu m^2/s$ for D and 0.15 for α.

Colocalization Analysis. The degree of QD colocalization with GFP signal was calculated for each detected track by calculating a GFP-colocalization score (CS_{GFP}) as described by Equation 4.1. This was accomplished by calculating the background-subtracted GFP intensity of a 3x3 pixel area centered on the (x,y) coordinates of the single-particle trajectory for each frame from the corresponding single frame GFP image. As indicated in Equation 4.1, the CS_{GFP} scores were normalized over the length of the trajectory and the bit depth of the image, which yields a unitless score for each trajectory that ranges between 0 and 1, where 0 means the trajectory has not association with the GFP signal and 1 means the trajectory was fully colocalized with GFP with saturated pixels.

4.5 References

1. Pinaud, F., Clarke, S., Sittner, A. & Dahan, M. Probing cellular events, one quantum dot at a time. *Nat. Methods* **7,** 275–285 (2010).
2. Derfus, A. M., Chan, W. C. W. & Bhatia, S. N. Intracellular delivery of quantum dots for live cell labeling and organelle tracking. *Adv. Mater.* **16,** 961–966 (2004).
3. Courty, S., Luccardini, C., Bellaiche, Y., Cappello, G. & Dahan, M. Tracking individual kinesin motors in living cells using single quantum-dot imaging. *Nano Lett.* **6,** 1491–1495 (2006).
4. Nelson, S. R., Ali, M. Y., Trybus, K. M. & Warshaw, D. M. Random walk of processive, quantum dot-labeled myosin Va molecules within the actin cortex of COS-7 cells. *Biophys. J.* **97,** 509 (2009).
5. Etoc, F. *et al.* Non-specific interactions govern cytosolic diffusion of nanosized objects in mammalian cells. *Nat. Mater.* **17,** 740 (2018).
6. Liu, J. *et al.* Repeated photoporation with graphene quantum dots enables homogeneous labeling of live cells with extrinsic markers for fluorescence microscopy. *Light Sci. Appl.* **7,** 47 (2018).
7. Los, G. V *et al.* HaloTag: a novel protein labeling technology for cell imaging and protein

analysis. *ACS Chem. Biol.* **3,** 373–382 (2008).

8. Pistor, S., Chakraborty, T., Niebuhr, K., Domann, E. & Wehland, J. The ActA protein of Listeria monocytogenes acts as a nucleator inducing reorganization of the actin cytoskeleton. *EMBO J.* **13,** 758–763 (1994).
9. Teng, K. W. *et al.* Labeling proteins inside living cells using external fluorophores for microscopy. *eLife* **5,** e20378 (2016).
10. Lim, S. J. *et al.* Brightness-equalized quantum dots. *Nat. Commun.* **6,** 8210 (2015).
11. Commons, W. File:GFP structure.png --- Wikimedia Commons{,} the free media repository. (2013).
12. Fluorescence SpectraViewer | Thermo Fisher Scientific - US. Available at: https://www.thermofisher.com/us/en/home/life-science/cell-analysis/labeling-chemistry/fluorescence-spectraviewer.html. (Accessed: 30th August 2018)
13. Baskin, J. M. *et al.* Copper-free click chemistry for dynamic in vivo imaging. *Proc. Natl. Acad. Sci.* **104,** 16793–16797 (2007).
14. Ma, L. *et al.* Multidentate Polymer Coatings for Compact and Homogeneous Quantum Dots with Efficient Bioconjugation. *J. Am. Chem. Soc.* **138,** 3382–3394 (2016).
15. Landsman, M. L., Kwant, G., Mook, G. A. & Zijlstra, W. G. Light-absorbing properties, stability, and spectral stabilization of indocyanine green. *J. Appl. Physiol.* **40,** 575–583 (1976).
16. Zinchuk, V., Zinchuk, O. & Okada, T. Quantitative colocalization analysis of multicolor confocal immunofluorescence microscopy images: pushing pixels to explore biological phenomena. *Acta Histochem. Cytochem.* **40,** 101–111 (2007).
17. Wu, Y., Zinchuk, V., Grossenbacher-Zinchuk, O. & Stefani, E. Critical evaluation of quantitative colocalization analysis in confocal fluorescence microscopy. *Interdiscip. Sci. Comput. Life Sci.* **4,** 27–37 (2012).
18. Shao, Q. & Jiang, S. Molecular understanding and design of zwitterionic materials. *Adv. Mater.* **27,** 15–26 (2015).
19. Neklesa, T. K. *et al.* Small-molecule hydrophobic tagging--induced degradation of HaloTag fusion proteins. *Nat. Chem. Biol.* **7,** 538 (2011).
20. Jaqaman, K. *et al.* Robust single-particle tracking in live-cell time-lapse sequences. *Nat. Methods* **5,** 695–702 (2008).
21. Banks, D. S. & Fradin, C. Anomalous diffusion of proteins due to molecular crowding. *Biophys. J.* **89,** 2960–2971 (2005).
22. Szymanski, J. & Weiss, M. Elucidating the origin of anomalous diffusion in crowded fluids. *Phys. Rev. Lett.* **103,** 38102 (2009).
23. Gal, N. & Weihs, D. Experimental evidence of strong anomalous diffusion in living cells. *Phys. Rev. E* **81,** 20903 (2010).
24. Weiss, M., Elsner, M., Kartberg, F. & Nilsson, T. Anomalous subdiffusion is a measure for cytoplasmic crowding in living cells. *Biophys. J.* **87,** 3518–3524 (2004).
25. Kepten, E., Weron, A., Sikora, G., Burnecki, K. & Garini, Y. Guidelines for the fitting of anomalous diffusion mean square displacement graphs from single particle tracking experiments. *PLoS One* **10,** e0117722 (2015).

CHAPTER 5: SINGLE QUANTUM DOT TRACKING TO MEASURE HYDRODYNAMIC SIZES DISTRIBUTIONS

5.1 Background

5.1.1 Nanoparticle Size Measurement Techniques

Accurate high-throughput characterization of nanoparticles is necessary to push forward the development of standardized, effective nanoparticle-based therapeutics. Current methods such as dynamic light scattering and fluorescence correlations spectroscopy are indirect ensemble techniques that require complex time series analysis to extract physical sizes, and these techniques have serious shortcomings in characterizing heterogenous nanoparticle populations.[1] Chromatography-based techniques such as size-exclusion chromatography can characterize heterogenous populations with good resolution, but they require correspondence to known standard curves in order to report absolute size measurements.[2,3]

The speed and high signal-to-noise ratio of sensitive widefield fluorescence imaging techniques such as highly inclined laminar optical sheet (HILO) microscopy allows for the characterization of a large field of potentially heterogeneous nanoparticles via direct measurement of the diffusive behavior of the nanoparticles. If other parameters, such as the viscosity and ambient temperature are known, then the diffusion coefficient can be directly converted into a hydrodynamic diameter (D_{HD}) using the Stokes-Einstein equation, which is given as follows:

$$D_{HD} = \frac{k_b T}{2\,\pi \eta D},$$

where k_b is the Boltzmann constant, T is temperature, η is viscosity, and D is the diffusion coefficient. Single-particle tracking (SPT) based size measurement has been applied in a commercial system that uses scattering. However, this scattering-based SPT technique is plagued by issues of nonspecific signal from sample contamination, and it is only able to accurately measure sizes of particles with D_{HD} >100 nm.[4,5] Here we present the initial development of a fluorescence microscopy based SPT measurement technique to accurately measure the hydrodynamic diameters of particles with $D_{HD} < 100$ nm.

5.1.2 Track Length Optimization for Accurate Size Measurement

Studies of *MSD* analysis of single-particle tracks deriving from first principles[6], Monte Carlo simulations[7], and experiments following one particle for thousands of frames[8] have demonstrated that when fitting to a Brownian diffusion model, longer unbroken trajectories are required for accurate fitting of the diffusion coefficient. As *MSD* analysis of single particle trajectories is a process that is subject to the limitations of experimental acquisition, such as localization error, finite length trajectories, and acquisition limitations, there is always some sort of spread of the distribution when calculating D_{HD} from SPT information. Qian, et. al. and Saxton showed from first principles and analysis of simulated trajectories what the distribution of fitted diffusion coefficients looks like under different experimental conditions.[6,7] Further they demonstrated that the key parameter for accurate diffusion coefficient measurement is to have long tracks.[6,7] This trend has been experimentally confirmed in follow-up studies that one particle for thousands of frames.[8]

5.2 Data and Results

5.2.1 Experimental Setup

In order to obtain single-particle tracks with sufficiently long lengths, we used aqueous solutions of glycerol with high weight percentages of glycerol (93-95%). Since the viscosities of such solutions of glycerol are well documented, given the ambient temperature we can calculate the viscosity of any aqueous solution of glycerol.[9,10] To investigate a range of nanoparticle sizes, pPEG-coated QDs with three different core sizes were prepared. The detailed characterization can be seen in Figure 5.1. The sizes measured by SEC serve as the gold standard that all further analysis steps are checked against.

The experimental data that was collected were 1000 frame long HILO movies of the pPEG-coated QDs diluted in 93, 95, and 98% glycerol solutions. These videos had dense fields of view that were processed to extract single-particle tracks using the FIJI plugin TrackMate.[11] Since TrackMate can run as a multi-threaded process, this allowed for the fast processing of many dense fields of diffusing particles.

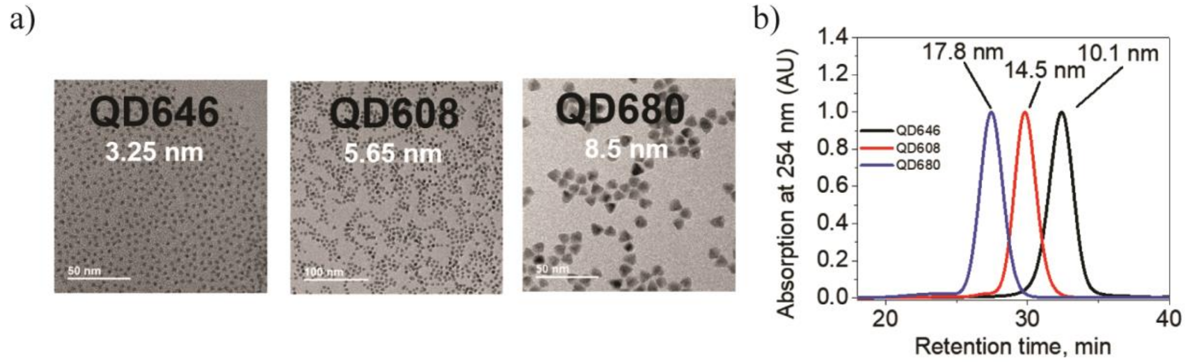

Figure 5.1 Characterization of 3 different sizes of pPEG-coated QDs (a) TEM images of bare QD cores with average core size superimposed on the images, (b) Size measurement of pPEG-coated QDs by size exclusion chromatography (SEC). Measured size from known standard curve indicated on the plot by the color-coded curves.

5.2.2 Mean Square Displacement and τ_{fit} Optimization

The *MSD* values of the SPT outputs were fit to the following Brownian diffusion model

$$MSD(\tau) = 4D\tau + 4\sigma_{xy}^2, \tag{5.1}$$

where σ_{xy} is the average localization error for each trajectory, which is an output parameter of the SPT algorithm. Optimizing the number of time lags to use for the *MSD* fitting, τ_{fit}, is a complex problem that has been addressed by experts in the field in different ways.[12,13] This is because a balance needs to be struck between using a small value for τ_{fit}, which may be influenced by inaccuracies in localization error measurement, and using large values for τ_{fit}, which is prone to error from the calculation of *MSD* values at long time lags with small sample numbers. Furthermore, as seen previously in Chapter 2 (Figure 2.8) imaging diffusing QDs with HILO leads to a distribution of track lengths, which makes it unclear what the optimal value for τ_{fit} would be.

In this regards, we proceeded with τ_{fit} optimization by testing out a series of fixed values (τ_{fit} = 4, 10, 25, 50, and 100) for all trajectories for QD680 diffusing in 93, 95, and 98% glycerol. Additionally, based on the recommendation from Michalet's analytical optimization for *MSD* fitting within particular parameters[13], we used the following equation for a variable definition of τ_{fit}:

$$\tau_{optim} = 3 + (4.5L^{0.4} - 8.5)^{1.2} \tag{5.2}$$

where τ_{optim} is the optimal τ_{fit} value and L is the length of the trajectory in frames. The results of both the fixed τ_{fit} and variable τ_{fit} fittings are summarized in Figure 5.2.

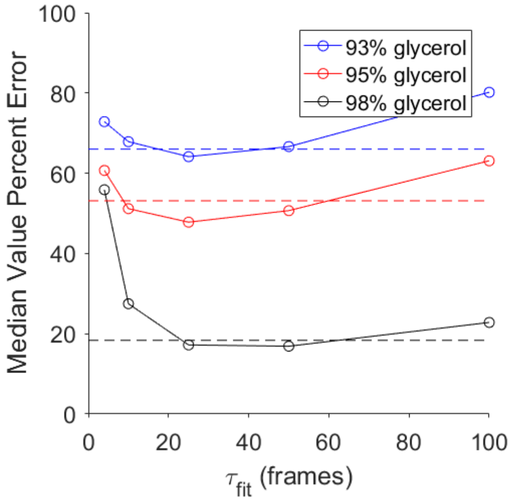

Figure 5.2 Plots of error in the median values of fitted D_{HD} for $\tau_{fit} = 4, 25, 50,$ and 100 calculated from experimentally acquired diffusion data of QD680 in 93, 95, and 98% glycerol. The dashed lines of the corresponding colors correspond to the error results from the τ_{optim} recommendation from Michalet.[13]

Due to the wide track length distribution resulting from the acquisition conditions, a fixed τ_{fit} value typically results in some degree of overestimation of D_{HD} that is exaggerated at the extreme values of the shortest and longest τ_{fit} values. Notably, the highest viscosity solutions have the lowest fitting error for, regardless of how τ_{fit} is defined. Furthermore, the variable τ_{optim} always yields error comparable to the lowest value produced by the best fixed τ_{fit} results. The accuracy of τ_{optim} is further confirmed when looking at the D_{HD} distributions (Figure 5.3). However, one outstanding question is the underlying factors for the spread the D_{HD} distributions.

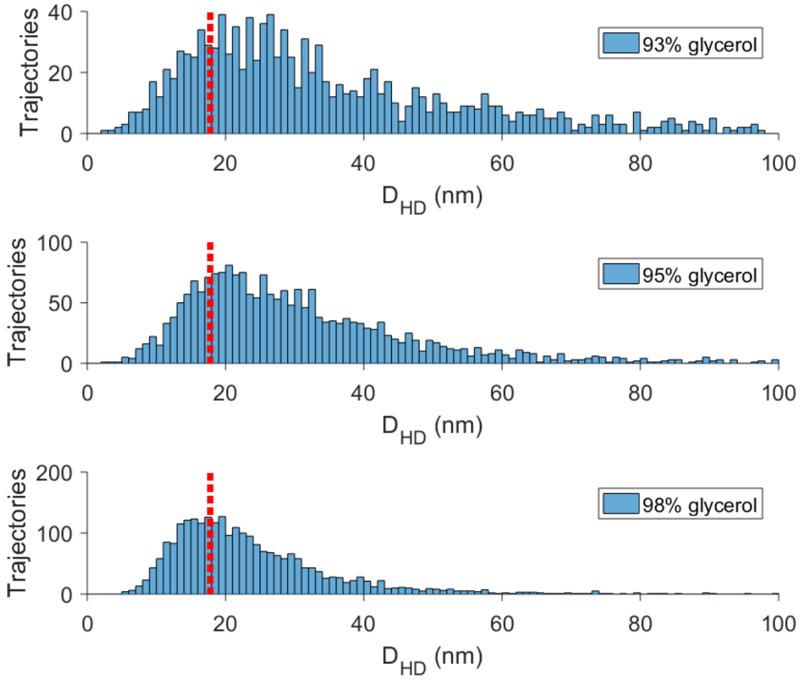

Figure 5.3 Histograms of fitted D_{HD} using the τ_{optim} recommendation from Michalet.[13] Calculated from experimentally acquired diffusion data of QD680 in 93, 95, and 98% glycerol. The red dashed line indicated the expected size by FPLC of 17.8 nm.

5.2.3 Verification of Hydrodynamic Diameter Distributions by Simulated Trajectories

In order to investigate the characteristics of our imaging and analysis technique we analyzed simulated trajectories based on the experimental data that was collected. Brownian motion was simulated using MATLAB *wfbm* function. The expected value for the diffusion coefficient, based on the size measured by SEC, was the primary input for the simulated trajectories. We truncated the trajectories based on the experimentally measure distribution of track lengths. Additionally, localization error was imposed as part of the simulation based experimentally measured values. Finally, these simulated trajectories were analyzed using the same *MSD* analysis approach detailed above with a range of fixed τ_{fit} values and τ_{optim}. The results of the simulated trajectory analyses are shown in Figure 5.4. Interestingly, τ_{optim} still approximates the best results from fixed τ_{fit} values. The most striking result of the simulation results is that even with an input of a single diffusion coefficient and using τ_{optim} results in an almost identical distribution of fitted D_{HD} values (Figure 5.5).

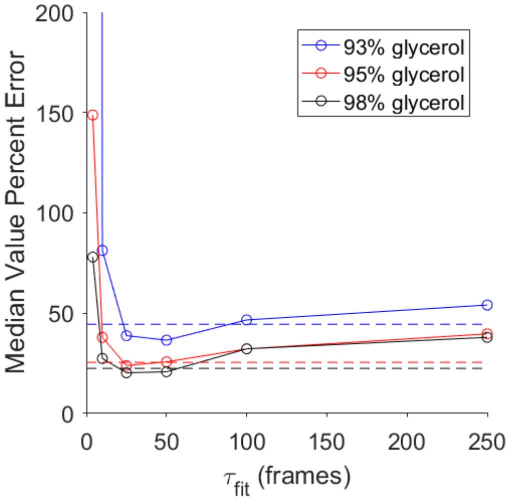

Figure 5.4 Plots of error in the median values of fitted D_{HD} for τ_{fit} = 4, 25, 50, and 100 calculated from simulated trajectories of QD680 in 93, 95, and 98% glycerol. The dashed lines of the corresponding colors correspond to the error results from the τ_{optim} recommendation from Michalet.[12]

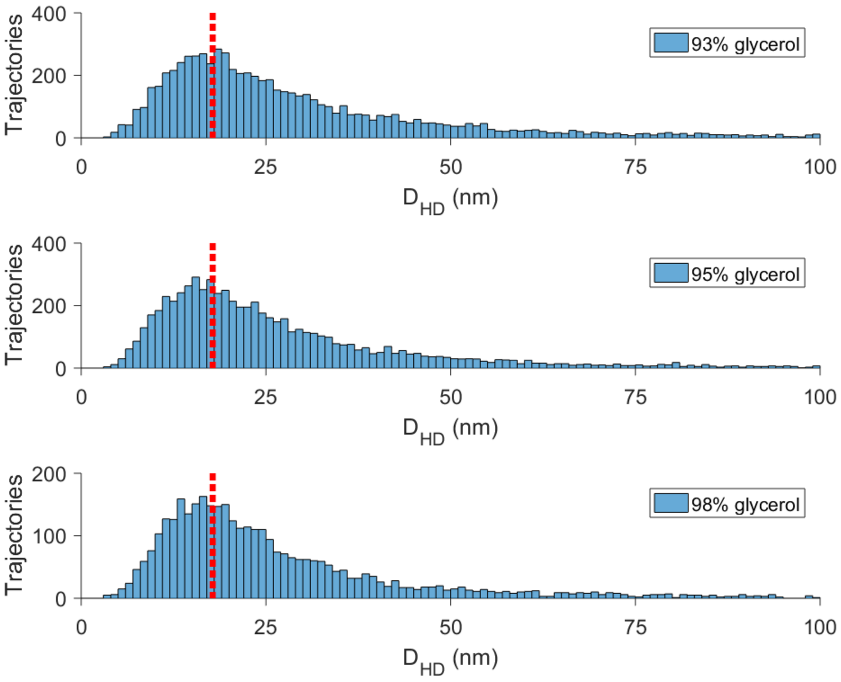

Figure 5.5 Histograms of fitted D_{HD} using the τ_{optim} recommendation from Michalet.[13] Calculated from simulated trajectories of QD680 in 93, 95, and 98% glycerol. The red dashed line indicated the expected size by FPLC of 17.8 nm.

5.3 Discussion

Here we demonstrated a direct measurement of nanoparticle size in the range of 20 nm D_{HD} using HILO microscopy based SPT analysis. This beats the lower limit of accurate size measurement by comparable scattering-based SPT analysis by nearly 80 nm.

By using an optimized variable definition for τ_{fit}, we were able to minimize the fitting error for D_{HD}. However, there is a significant spread of the fitted D_{HD} distribution, which we were able to confirm was characteristic of the acquisition and analysis method by analysis of simulated trajectories. These leaves some open questions about what the resolution limit of this method will be for measuring nanoparticle size.

These questions will be further investigated by measuring the sizes of the other two sizes of QDs depicted in Figure 5.1 in addition to particles with fixed core size and variable polymer coating thicknesses. Ultimately, the goal will be to analyze a population of QDs with mixed sizes to demonstrate the power of widefield SPT analysis to measure the sizes of heterogenous populations of nanoparticles.

5.4 Methods

Quantum Dot Synthesis. *(QDs synthesized by Suresh Sarkar, UIUC)* The three different QD cores were synthesized similarly to the methods described in previous chapters. Differences in the synthetic protocol can be found in recently published work.[14]

Transmission Electron Microscopy of QDs. *(Performed by Suresh Sarkar, UIUC)* TEM images were obtained using a JEOL 2010 LaB6 high-resolution microscope in the Frederick Seitz Materials Research Laboratory Central Research Facilities at University of Illinois. For QDs in organic solvents, samples were prepared by placing a drop of dilute QD solution in hexane on an ultrathin carbon film TEM grid (Ted Pella; Product # 01824) and then wicking the solution off with a tissue.

pPEG Quantum Dot Coating. *(QDs coated and characterized by Liang Ma, UIUC)* A methanol solution of tetramethylammonium hydroxide (25%) was added to a biphasic mixture of *N*-methylformamide (NMF) and purified QDs in hexane. The suspension was stirred vigorously for 1 hour until the QDs were completely transferred to the NMF phase. Hexane was removed, and the NMF solution was washed with hexane twice. Residual hexane and methanol were evaporated under vacuum. A solution of pPEG in NMF (5:1 imidazole to QD surface atom) was added dropwise to the hydroxide-coated QDs in NMF (1 μM, 0.4 mL) with stirring under nitrogen atmosphere. The reaction was allowed to proceed at 110°C for 2 hours. The coated QDs were precipitated from NMF using anhydrous diethyl ether. The QDs were then dispersed in 50 mM sodium borate buffer (pH 8.5) and centrifuged to remove possible aggregates. The QDs were purified using centrifugal filtration (Amicon Ultra 50 kDa molecular weight cutoff) in 50 mM sodium borate buffer. The dilution–filtration cycle was performed five times. Monodispersity of coated QDs was assessed by size exclusion chromatography.

Sample Preparation. QDs prepared in 50 mM borate buffer were dispersed in glycerol to reach a final concentration of 0.123 nM and a glycerol concentration of ~93, 95, or 98%. For imaging, ~100 µL of the QDs dispersed in the glycerol solution were deposited in a CellView dish with a #1.5 coverglass bottom (Greiner Bio-One, Kremsmünster, Austria).

Microscopy. All samples were imaged using highly-inclined laminar optical sheet (HILO) microscopy on a Zeiss Axio Observer.Z1 inverted microscope (Zeiss, Oberkochen, Germany) with a 100x 1.45 NA alpha Plan-Fluar oil immersion microscope. The particles were excited with a 488nm 100mW optically pumped semiconductor laser with 15% laser power at optimized HILO angles for our system (~60° from normal). Excitation light was excluded using a 482/18 nm laser-line bandpass filter (Semrock), and emission light was filtered with a 600/37 nm or 650/100 nm bandpass filter (Semrock.. Data was acquired on a Photometrics eXcelon Evolve 512 EMCCD (Photometrics, Tuscon, AZ) and using Zeiss Zen software. All samples were uniformly excited, and data was collected for 60 seconds at a rate of 21.64 frames/s.

Diffusion Analysis. Single particle detection and tracking was done using the FIJI plugin called

TrackMate.[11] Custom MATLAB scripts were used to calculate MSD values for all of the tracked particles and to fit a Brownian motion model in order to calculate diffusion coefficient values. In order to accurately calculate hydrodynamic diameters from these diffusion coefficient values, only particle tracks with a length of 200 frames or more (based on literature recommendations[7,8]) and a diffusion coefficient greater than 0.02 $\mu m^2/s$ (based on the empirically determined localization error for immobilized particles on our system) were included in the hydrodynamic diameter calculations. Hydrodynamic diameters were calculated using the Stokes-Einstein relation and known viscosity values of glycerol solutions.[10]

Analysis of Simulated Trajectories. Trajectories were simulated using the MATLAB *wfbm* function, which generates a fractional Brownian motion trajectory with specified α (set to $\alpha = 1$ in this case to simulation Brownian motion), when normalized by standard deviation. Trajectories were scaled by D, and a series of normally distributed measurement errors were added to each position in each dimension.[15] Measurement errors derived from a distribution with zero mean and a standard deviation derived from the mean experimental localization error from the SPT analysis for each QD coating class. Track lengths were truncated to match the distribution of experimentally measured track lengths. These simulated trajectories were analyzed using the diffusion analysis method described above.

5.5 References

1. Filipe, V., Hawe, A. & Jiskoot, W. Critical evaluation of Nanoparticle Tracking Analysis (NTA) by NanoSight for the measurement of nanoparticles and protein aggregates. *Pharm. Res.* **27,** 796–810 (2010).
2. Kostanski, L. K., Keller, D. M. & Hamielec, A. E. Size-exclusion chromatography—a review of calibration methodologies. *J. Biochem. Biophys. Methods* **58,** 159–186 (2004).
3. Hong, P., Koza, S. & Bouvier, E. S. P. A review size-exclusion chromatography for the

analysis of protein biotherapeutics and their aggregates. *J. Liq. Chromatogr. Relat. Technol.* **35,** 2923–2950 (2012).

4. der Pol, E. *et al.* Particle size distribution of exosomes and microvesicles determined by transmission electron microscopy, flow cytometry, nanoparticle tracking analysis, and resistive pulse sensing. *J. Thromb. Haemost.* **12,** 1182–1192 (2014).
5. Hole, P. *et al.* Interlaboratory comparison of size measurements on nanoparticles using nanoparticle tracking analysis (NTA). *J. nanoparticle Res.* **15,** 2101 (2013).
6. Qian, H., Sheetz, M. P. & Elson, E. L. Single particle tracking. Analysis of diffusion and flow in two-dimensional systems. *Biophys. J.* **60,** 910–921 (1991).
7. Saxton, M. J. Single-particle tracking: the distribution of diffusion coefficients. *Biophys. J.* **72,** 1744 (1997).
8. Ernst, D. & Köhler, J. Measuring a diffusion coefficient by single-particle tracking: statistical analysis of experimental mean squared displacement curves. *Phys. Chem. Chem. Phys.* **15,** 845–849 (2013).
9. Segur, J. B. & Oberstar, H. E. Viscosity of glycerol and its aqueous solutions. *Ind. Eng. Chem.* **43,** 2117–2120 (1951).
10. Cheng, N.-S. Formula for the viscosity of a glycerol- water mixture. *Ind. Eng. Chem. Res.* **47,** 3285–3288 (2008).
11. Tinevez, J.-Y. *et al.* TrackMate: An open and extensible platform for single-particle tracking. *Methods* **115,** 80–90 (2017).
12. Michalet, X. Mean square displacement analysis of single-particle trajectories with localization error: Brownian motion in an isotropic medium. *Phys. Rev. E* **82,** 41914 (2010).
13. Michalet, X. & Berglund, A. J. Optimal diffusion coefficient estimation in single-particle tracking. *Phys. Rev. E* **85,** 61916 (2012).
14. Liu, Y. *et al.* Enhanced mRNA FISH with compact quantum dots. *Nat. Commun.* **9,** 4461 (2018).
15. Kepten, E., Weron, A., Sikora, G., Burnecki, K. & Garini, Y. Guidelines for the fitting of anomalous diffusion mean square displacement graphs from single particle tracking experiments. *PLoS One* **10,** e0117722 (2015).

CHAPTER 6: CONCLUSIONS AND OUTLOOK

6.1 Summary

QDs have made an important impact in the past decade in understanding complex processes intrinsic to biology with one of the primary areas of impact being measurements of single-molecule dynamics, which have been made possible by the unique optical properties of QDs. The work presented in this dissertation builds on this progress, specifically making advances in the imaging in the intracellular space and nanoparticle size measurement.

In Chapter 2, we described a new analysis technique combining single-molecule diffusion and brightness analysis. This approach further yielded novel single-cell metrics that can be used to interrogate nanoparticle delivery mechanisms and intracellular particle state and final fate. In Chapters 3, this analysis technique was used to optimize QD surfaces for optimal intracellular delivery with outcomes suggesting that for intracellular targeting with molecular probes, stable and neutral surfaces are ideal. In Chapter 4, we presented initial work aimed towards specific targeting of intracellular proteins in live cells with externally delivered QD-probes with such stable and electrostatically neutral surfaces. We further used quantitative verification of the targeted labeling by characterization of the degree of colocalization with the target fusion protein showing an increased colocalization of the QD-probe with the target protein in the group without ligand blocking. Finally, in Chapter 5 we demonstrated a direct measurement of nanoparticle size in the range of 20 nm D_{HD} using HILO microscopy based SPT analysis beating the lower limit of accurate size measurement by comparable scattering-based SPT analysis by nearly 80 nm.

6.2 Future Outlook

With recent advances in instrumentation, probes, and image analysis software, the capacity to perform single-molecule tracking is now widely available.[1–4] With the new methods presented, it will be possible to use single-particle imaging and tracking not just as a tools to understand biology at this scale, but also to understand and optimize intracellular delivery of nanoparticles and intracellular dynamics and trafficking. It may be possible to accurately apply pharmacodynamics models relating dose to efficacy and potency for nanoparticle therapeutics, which present unique challenges due to uncertainty of numerous transport parameters.[5] Additionally, even though this method currently limited to imaging cultured cells, it could also potentially be applied to evaluate delivery in living tissues in both intracellular and extracellular domains using imaging techniques with both rapid acquisition and high depth penetration, such as spinning disk confocal microscopy, light sheet microscopy, or holographic multiphoton imaging.[6,7]

Furthermore, if the appropriate materials improvements can be made to optimize intracellular labeling of proteins with extrinsically delivered QDs for cytoplasmic targets that are relatively stationary, then the optimized intracellular labeling parameters could be extended to labeling more dynamic targets, such as transcription factors. The tracking of intracellular protein dynamics and trafficking, especially in response to drug treatments, could reveal biological mechanisms that have never been measured before.

6.3 References

1. Li, G.-W. & Xie, X. S. Central dogma at the single-molecule level in living cells. *Nature* **475,** 308 (2011).
2. Wu, B., Buxbaum, A. R., Katz, Z. B., Yoon, Y. J. & Singer, R. H. Quantifying protein-mRNA interactions in single live cells. *Cell* **162,** 211–220 (2015).
3. Kusumi, A., Tsunoyama, T. A., Hirosawa, K. M., Kasai, R. S. & Fujiwara, T. K. Tracking single molecules at work in living cells. *Nat. Chem. Biol.* **10,** 524–532 (2014).
4. Manzo, C. & Garcia-Parajo, M. F. A review of progress in single particle tracking: from methods to biophysical insights. *Reports Prog. Phys.* **78,** 124601 (2015).
5. Li, M., Zou, P., Tyner, K. & Lee, S. Physiologically based pharmacokinetic (PBPK) modeling of pharmaceutical nanoparticles. *AAPS J.* **19,** 26–42 (2017).
6. Gonda, K., Watanabe, T. M., Ohuchi, N. & Higuchi, H. In vivo nano-imaging of membrane dynamics in metastatic tumor cells using quantum dots. *J. Biol. Chem.* **285,** 2750–2757 (2010).
7. Zhang, R. *et al.* Two-Photon 3D FIONA of Individual Quantum Dots in an Aqueous Environment. *Nano Lett.* **11,** 4074–4078 (2011).